ANNEALING AND PRECIPITATION BEHAVIOR DURING BATCH ANNEALING OF HSLA STEELS

by

Chao Fang

B.S. in Materials Science and Engineering, University of Science and Technology Beijing, 2000

Submitted to the Graduate Faculty of

Swanson School of Engineering in partial fulfillment

of the requirements for the degree of

Doctor of Philosophy

University of Pittsburgh

2011

UNIVERSITY OF PITTSBURGH

SWANSON SCHOOL OF ENGINEERING

This dissertation was presented

by

Chao Fang

It was defended on

March 1st, 2011

and approved by

C. Issac Garcia, Research Professor, Mechanical Engineering and Materials Science

Ian Nettleship, Associate Professor, Mechanical Engineering and Materials Science

Luis E. Vallejo, Professor, Civil and Environmental Engineering

Shi-Hoon Choi, Associate Professor, Applied Materials Engineering, Sunchon National University

Dissertation Director: Anthony J. DeArdo, Professor, Mechanical Engineering and Materials Science

ANNEALING AND PRECIPITATION BEHAVIOR DURING BATCH ANNEALING OF HSLA STEELS

Chao Fang, PhD

University of Pittsburgh, 2011

To gain a fundamental understanding of the factors responsible for the kinetics of annealing behavior during batch annealing for high strength low alloy (HSLA) steels, studies have been conducted to analyze the influence of alloy composition, hot band state, cold rolling reduction (CR%), heating rate, soaking temperature and time, etc. on the annealing behavior of HSLA steels during batch annealing process. The recrystallization kinetics was mainly controlled by several key parameters such as stored energy, precipitation and/or solute drag, special grain boundaries, and texture, etc. The combination of Electron Back-Scattered Diffraction (EBSD) technique and the Sub-grain Method was used to construct and analyze stored energy distribution maps before and during the batch annealing process of cold rolled HSLA steels. Precipitation behavior was studied using Scanning Electron Microscopy (SEM), Energy Dispersive X-ray Spectroscopy (EDS), Transmission Electron Microscopy (TEM), and High Resolution TEM (HRTEM). Grain boundary characteristic and texture fibers were also analyzed using EBSD scanning data. The results show that different composition and processing parameters would cause different hot band microstructure and different amounts of dislocation density, i.e., stored energy, remained in the alloys after hot rolling deformation. Higher dislocation density in the hot band steel will cause even higher dislocation density in the sheet steel after cold rolling deformation, which will cause higher recrystallization speed at early stages. If precipitates were formed during annealing, their formation would consume part of the stored energy and decreased

some driving force. The new formed fine precipitates would also apply certain pinning force on the grain boundaries, which dragged the moving of those boundaries, i.e., lowered the recrystallization speed further. Certain special grain boundaries like Coincident Site Lattice (CSL) boundaries have very low boundary energy and mobility. The higher volume fraction of this kind of boundaries would also slow down the recrystallization process. Texture could not be a critical factor causing the different annealing behavior in this study, since the texture fibers distributions are very similar. Two or more factors might affect the annealing process at the same time. Some factors could be more efficient than others at certain stage or stages.

TABLE OF CONTENTS

LIST OF TABLES

LIST OF FIGURES

ACKNOWLEDGMENTS

The completion of this study would have never been possible without those helps, supports and assistances from so many kind persons. Here, I would like to give my most sincere thanks to them.

First and foremost, I would like to thank my advisors, Professor Anthony J. DeArdo and Professor C. Isaac Garcia for their great guidance and generous support throughout my research. Their invaluable advices and suggestions make the whole research so well organized and directed. I would also like to extend my gratitude to my other committee members, Professor Ian Nettleship, Professor Luis E. Vallejo and Professor Shi-Hoon Choi. Their collective insights have been vital to the success of this work.

I would like to thank Professor Minking K. Chyu, the Chairman of Mechanical Engineering and Materials Science Department, for his invaluable help and support at my most difficult times. Special thanks are due to Dr. Ken Goldman. He is a very kind and generous man and a great teacher in both research and language. His years of help make so many things much easier.

Special thanks are extended to Long Li, Dr. Kengun Cho, and Professor Mingjian Hua, as well as to Xiaojun Liang, Hoe-Seok Yang, Albert Stewart, and Cole Van Ormer, for their generous and constant help on my experiments.

I would like to thank the Basic Metals Processing Research Institute (BAMPRI) and the Mechanical Engineering and Materials Science Department, University of Pittsburgh for providing the facilities to conduct this work. I would also like to thank the steel companies that form part of the BAMPRI-Thin Slab Casting consortium such as Nucor-Decatur and Nucor-Berkeley for providing the steel samples and financial support for this program.

Last but not least, I would like to thank my wife, Li Sun, my parents and sisters, and my cute little daughter, Jenny S. Fang for their love, support and giving me happiness and courage through the critical stages of my Ph.D. Program.

Thank you all very much!

This dissertation is especially dedicated to my dad and sister in heaven, my mom, my sisters, my wife and my daughter.

1.0 INTRODUCTION

Cold rolled steels are usually annealed to relieve internal stresses, soften the steel, develop new texture and improve mechanical properties such as formability, drawability and ductility. Two different principal annealing processes are normally employed, batch (or box) annealing and continuous annealing. Despite the advantages of continuous annealing, batch annealing is still widely used in industry. During batch annealing, several coils are stacked together and treated at once in a furnace at a desired thermal profile. Coil surfaces absorb more heat than the coil centers, so the actual thermal profile applied on the coil surfaces and coil centers are different. The difference in thermal uniformity results in different levels of annealing results and uneven final properties of the steels throughout the coil. The initial purpose of this study is to understand the effects of thermal profile on the annealing behavior of High Strength Low Alloy (HSLA) steels. The final purpose of this work is to suggest ways to eliminate or reduce the difference in recrystallization between the outer and inner coils. Since recovery, recrystallization and grain growth during the annealing process are affected by many factors such as: alloy composition, hot band state, cold rolling rate, texture, annealing temperature, heating rate, soaking time, cooling rate, etc., all of them will be considered in this work. The stored energy distribution and its relationship with texture will be analyzed before and after annealing, and the effects of solute drag and/or precipitation on T_{start} and T_{end} and the kinetics of recrystallization will be another focused topic. Also, because of the considerable capital, maintenance, and energy costs associated with the batch annealing process, the optimization of heating and cooling schedules to improve the productive capacity of these units is a subject of great interest at present.

2.0 BACKGROUND

2.1 COLD ROLLING AND STORED ENERGY

Most of the energy expended in plastically deforming a metal appears in the form of heat, but a small percentage of the energy remains “stored” in the metal as strain energy causing an increase in internal energy [1]. The increase of the free energy is known as stored energy. This stored energy is associated with various lattice defects generated during deformation and provides the initial driving force for recovery and recrystallization in the annealing process. The defects are present as dislocations and defects like point defects (zero dimension), line defects (one dimension), planar defects (two dimension), and a material containing these defects is thermodynamically unstable [2]. Although thermodynamics would suggest that the defects should spontaneously disappear, in practice, the necessary atomistic mechanisms are often very slow at low homologous temperatures, which mean that most unstable defect structures are retained after deformation.

2.1.1 Stored energy distribution and its relationship to deformation and texture

The amount of stored energy depends on the type of metals, composition of the metal, the deformation process, as well as the rate and temperature of deformation. Numerous studies have shown that the stored energy increases with increasing deformation, but at a decreased rate, so that the fraction of the total energy stored compared to the total energy expended decreases with increasing deformation [3]. The amount of stored energy can be greatly increased by increasing the severity of the deformation, lowering the deformation temperature, and by changing the pure metal to an alloy or changing alloy composition [1, 4-6]. Cold working is able to increase the number of dislocations in a metal by a factor as large as 10,000 to 1,000,000 times. Since each dislocation represents a crystal defect with an associated lattice strain, increasing the dislocation density increases the strain energy of the metal.

The stored energy of deformation in single crystals varies significantly with the different crystal orientations in metals or alloys. The texture fiber is a one dimensional description of a texture. It is essentially the value of the orientation distribution function (ODF) along a given "fiber" in Euler space. The idea of texture fibers first arose in the analysis of texture from rolled face centered cubic (FCC) materials. In these materials, local maxima tend to align themselves along a characteristic fiber. Thus, the description of the texture can be reduced from three-dimensional ODF to a one-dimensional trace along the fiber. However, this characteristic fiber tends to shift slightly from sample to sample. Thus, instead of using exact locations in Euler space to define the fiber, local maxima along the fiber are used. For body center cubic (BCC) metals and alloys, most stored energy is distributed along either α fibers or γ fibers. The α-fiber is a partial fiber texture with a <110> fiber axis parallel to the rolling direction and intensity maxima at {001} <110>, {112} <110> and {111} <110>. The γ-fiber is a fairly complete fiber texture with the <111> fiber axis parallel to the sheet normal; the major components in this fiber texture have <110>, <112> and <123> aligned with the rolling direction. In Oyarzabal's work [7], EBSD results indicate that the cold work stored energy in the α-fiber components is minimum at {1 0 0} <0 1 1> and increases monotonously towards the {1 1 1} <0 1 1>, which is common to the α and γ fibers. The stored energy among all the components belonging to the γ-fiber remains almost at the same level. The mean stored energy is higher in the deformed grains with γ-fiber orientations. In Vanderschueren's work [8], similar results were obtained. In Cao's work [9], deformed {111} <112> and {111} <110> grains in the cold-rolled IF steels generally disappear at the early stage of recrystallization whereas deformed {001} <110> and {112} <110> grains, are mostly consumed at the late stage of recrystallization. This difference is attributed to the difference in stored energy between grains having different orientations. New {111} <110> grains are nucleated within deformed {111} <112> grains and new {111} <112> grains originated in the deformed {111} <110> grains. In Etter's work [10], the results show that: 1. the stored energy increases with the amount of reduction in both α and γ fibers in ferrite. 2. Stored energy evolution with cold rolling reduction is described for texture components of both fibers of the ferrite. The γ-fiber's energy remains greater than the α-fiber's. Avraamov [11] also observed that the γ-fiber of the major components represent the largest stored energy of deformation. The stored energy varies in the different texture components of the material, which was also supported by TEM results from Dillamore et al. [12], X-ray line broadening results of Every & Hatherly [13], where measurements were made on reflections from different crystal planes lying parallel to the cold-rolled steel sheet, and also by the neutron diffraction measurements of Rajmohan [14].

2.1.2 Stored energy measurement or calculation methods

To study the distribution characteristics of stored energy, many methods have been used to measure or calculate it directly or indirectly. The following are several commonly used methods.

2.1.2.1 Subgrain Method

Choi [15] developed the Subgrain Method to evaluate the orientation-dependent stored energy of deformed grains from the data measured using electron back-scattered diffraction (EBSD) analysis. The subgrain structure in the deformed microstructure was used in the calculation of stored energy. If the dislocation substructure can be simplified in the form of subgrains of diameter, D, and boundary energy, γ, then the stored energy, S_i of each lattice site, can be given by:

$$S_i = \alpha \frac{\gamma}{D}$$

, where α is the geometric constant ~3. If we assume that the boundary energy of a subgrain is only a function of the boundary misorientation (Δθ) and not dependent on the boundary types (tilt and twist), the boundary energy from the Read–Shockley equation [16] can be expressed as the following relation:

$$\gamma(\Delta\theta) = \begin{cases} \gamma_m \dfrac{\theta'}{\theta^*}\left[1 - \ln\left(\dfrac{\theta'}{\theta^*}\right)\right], & \theta' < \theta^* \\ \gamma_m, & \theta' \geq \theta^* \end{cases}$$

, where θ' = |Δθ | for 0 ≤ | Δθ| ≤ π and θ' = 2π − | Δθ| for π ≤ | Δθ| ≤ 2π, Δθ is the boundary misorientation between two neighboring subgrains, θ^* is the misorientation limit for low angle grain boundaries, which was chosen as 15°, and γ_m is the specific energy of high angle grain boundaries. This method is a new way to quantify the heterogeneous distribution of stored energy in deformed metal materials. It will be used in this study to construct stored energy distribution maps.

2.1.2.2 Neutron line broadening

Rajmohan et al. [14] derived the stored energy distribution function in the Euler angle space for cold-rolled IF steels by measuring the neutron line broadening. However, since the method provides average stored energy for each orientation, it cannot be used to study the heterogeneous distribution of stored energy inside the individual or specific deformed grains.

2.1.2.3 Image Quality (IQ)

The image quality (or pattern quality) determined by electron back scattered diffraction (EBSD) analysis was used to estimate the orientation-dependent stored energy in cold-rolled materials [17]. However, since the pattern quality can be affected by experimental procedures such as specimen surface quality and beam quality, it can only be used as a semi-quantitative value for the stored energy term. A recent method on normalizing the raw data developed by previous studies in BAMPRI [18] can minimize these variations caused by experimental condition, which makes it an optional method in this study.

2.1.2.4 Taylor's Factor

In the theoretical work, the Taylor model was used to calculate the Taylor factor as a measurement of an orientation-dependent stored energy in cold-rolled steels [14, 19]. The Taylor factor is a first-order approximation for the stored energy induced by plastic deformation of polycrystalline materials. The assumption of homogenization scheme (stress and strain rate are uniform in each grain) is not proper to simulate the heterogeneous distribution of stored energy in the deformed grains. However, Taylor's second assumption of slip or deformation by the motion of perfect dislocations is appropriate for high stacking fault materials such as BCC α-iron.

2.1.2.5 Simulation Methods

Bacroix et al. [20] and Diligent et al. [21] calculated the orientation-dependent stored energy in cold-rolled IF steels with the visco-plastic self-consistent and elasto-plastic self-consistent polycrystal models, respectively. The polycrystal models also assume that the stress and strain rate is uniform in each grain, so they have the similar limitation as the Taylor model.

In order to overcome the shortcoming of the models, Sarma et al. [22, 23] simulated the plane strain compression of FCC polycrystalline materials to determine the orientation-dependent stored energy using a crystal plasticity finite element model with a real configuration for microstructure. The results of their simulation provided a means to obtain quantitative information on the inhomogeneous distribution of stored energy and orientations among the different grains comprising FCC polycrystalline materials.

Raabe et al. [24-26] investigated the influences of intrinsic (initial grain orientation) and extrinsic (neighboring grains) origins on the formation of orientation gradients using a 3-D crystal plasticity finite element model with BCC and FCC bi-crystal structures.

Choi [27] simulated plane strain compression of polycrystalline IF steel using a quasi 3-D crystal plasticity finite element model in a similar approach to Becker [28, 29]. Moreover, the inhomogeneous stored energy in cold-rolled IF steel was analyzed quantitatively as a function of orientation. In order to estimate the magnitude of the orientation gradient in deformed grains, the misorientation angle was calculated for all elements and compared for all grains.

2.1.3 Energy balance between recovery and recrystallization

Recovery and recrystallization are competing processes as both are driven by the stored energy of the deformed state. Conversely, because recovery lowers the driving force for recrystallization, a significant amount of prior recovery may in turn influence the nature and the kinetics of recrystallization. The division between recovery and recrystallization is sometimes difficult to define, because recovery mechanisms play an important role in nucleating recrystallization.

The nature of the material itself also determines the extent of recovery. One of the most important parameters is the stacking fault energy, γ_{SFE}, which determines the rate of dislocation climb and cross slip. They are the mechanisms which usually control the rate of recovery. In metals of low stacking fault energy such as copper, α-brass and austenitic stainless steel, cross slip and climb are difficult, and little recovery of the dislocation structure normally occurs prior to recrystallization. However, in metals of high stacking fault energy such as aluminium and α - iron, climb is rapid and cross slip is easy, and significant recovery may occur.

2.2 BATCH ANNEALING AND CONTINUOUS ANNEALING

Steel material hardens after cold rolling due to the defects generated by plastic deformation. Annealing is therefore carried out to soften the material. The annealing process comprises heating, holding of the material at an elevated temperature (soaking), and cooling of the material. Heating facilitates the movement of iron atoms, resulting in the disappearance of tangled dislocations and the formation and growth of new grains of various sizes, which depend on the heating and soaking conditions. These phenomena make work hardened or cold rolled steel crystals recover and recrystallize to be softened. In the steel industry, the steel is heated and profile controlled, with times and temperatures set according to the properties desired to reach an increased ductility and relieve strains that lead to failures in service. The annealing process can be classed by soaking temperature into recovery annealing and recrystallization annealing. The recovery annealing uses a temperature lower than the start temperature of recrystallization, while a recrystallization annealing normally uses a temperature higher than that temperature. The recrystallization annealing was concerned in this study.

The annealing of cold rolled coils has conventionally been conducted by grouping and annealing the coils in batches stacked in a bell-type furnace. This process is called batch annealing. Continuous annealing is now more commonly used. Continuous annealing involves uncoiling, and welding strips together, passing the welded strips continuously through a heating furnace, and then dividing and recoiling the strips. Unlike continuous annealing, where the strip of steel is uncoiled, treated and rewound in approximately 15 minutes (throughput about 80 tons per hour), batch annealing heats several coils together in large furnaces over approximately 3 days (throughput about 1.4 tons per hour). The coils are usually stacked on fixed bases, covered, and mobile furnaces lowered onto them. Figure 1 shows a) a typical single stack gas-fired annealing furnace and b) a multi-stack annealing furnace. Gas and/or electrical heating are used for the furnaces.

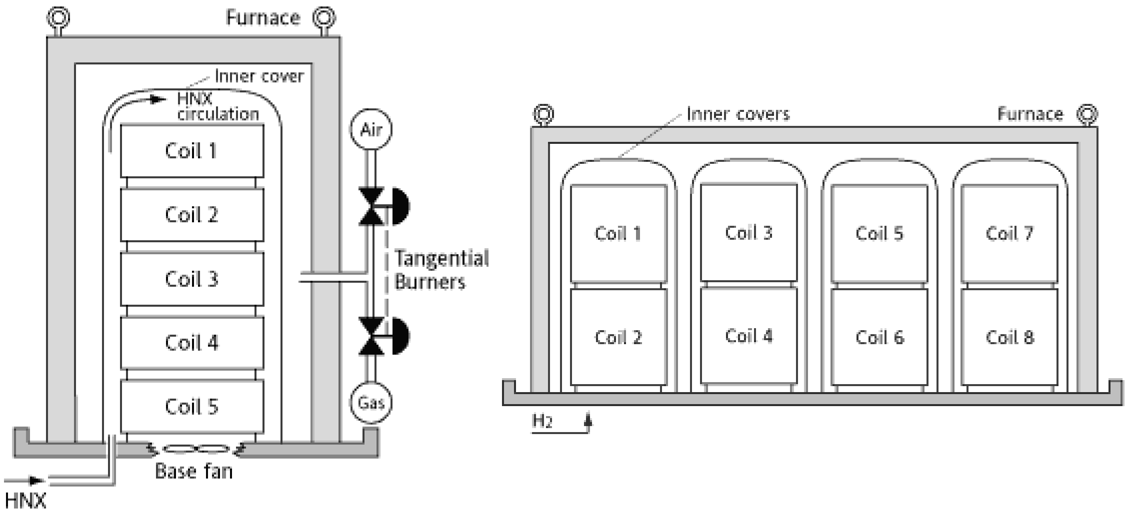

Figure 1. Single stack annealing furnace (left) and multi-stack annealing furnace (right)

Batch annealing is usually performed at subcritical temperatures, below T_{Ac1}, that are below 725°C for low carbon steel. Conversely, the continuous annealing process is usually performed at intercritical temperatures that are approximately 800°C, but the annealing time is short enough so that no austenite is formed. In this study, the batch annealing process is simulated.

2.3 RECOVERY

Recovery can be defined as all annealing processes occurring in deformed materials that occur without the migration of a high angle grain boundary. Typically, recovery processes involve the rearrangement of dislocations to lower their energy, for example by the formation of low-angle subgrain boundaries. Stored energy is partially released. Recovery refers to changes in a deformed material which occur prior to recrystallization, and which partially restore the properties to their values before deformation. During recovery, the microstructural changes in a material are subtle and occur on a small scale. The microstructures as observed by optical microscopy do not usually reveal much change and for this reason, recovery is often measured indirectly by some bulk technique, for example by following the change in some physical or mechanical properties [30]. Measurement of the changes in stored energy by calorimetry is the most direct method of following recovery because the stored energy is related to the number and configuration of the dislocations in the material [31]. The microstructural changes which occur during recovery affect the mechanical properties, and therefore, recovery is often measured by changes in the yield stress or hardness of the material [32]. Several other physical properties including density and electrical resistivity which are altered during plastic deformation are subsequently modified by recovery. Monitoring the changes in these properties is another way to measure recovery.

During recovery the stored energy of the material is lowered by dislocation movement. There are two primary processes, these being the annihilation of dislocations and the rearrangement of dislocations into lower energy configurations. Both processes are achieved by glide, climb and cross-slip of dislocations [33].

On annealing, the excess dislocations will arrange into lower energy configurations in the form of regular arrays or low angle grain boundaries (LAGBs). The simplest case is that dislocations of only one Burgers vector are involved. Such a structure may be replicated experimentally by bending a single crystal which is deforming on a single slip system, as was first demonstrated by Cahn [34], and this mechanism is often known as polygonization. According to the Read-Shockley equation [16], the energy of a tilt boundary increases with increasing misorientation and the energy per dislocation decreases with increasing misorientation. Therefore, there is a driving force to form fewer, more highly misoriented boundaries as recovery proceeds.

2.4 RECRYSTALLIZATION

Recrystallization is the formation of a new grain structure in a deformed material by the formation and a migration of high angle grain boundaries driven by the stored energy of deformation; new strain free grains are formed behind the moving grain boundaries. Recrystallization of the deformed microstructure is often called primary recrystallization in order to distinguish it from the process of abnormal grain growth which may occur in fully recrystallized material and which is sometimes called secondary recrystallization or abnormal grain growth [35]. It is convenient to divide primary recrystallization into two regimes, nucleation which corresponds to the first appearance of new grains in the microstructure and growth, during which the new grains replace deformed material. Although these two events occur consecutively for any particular grain, both nucleation and growth may be occurring at any time throughout the specimen. The progress of recrystallization with time during isothermal annealing is commonly represented by a plot of the volume fraction of material recrystallized (X_V) as a function of log (time). This plot typically shows an apparent incubation time before recrystallization is detected. This is followed by an increasing rate of recrystallization, a linear region, and finally a decreasing rate of recrystallization.

2.4.1 Mechanism of recrystallization

In recrystallization, a set of new grains will be formed. New crystals appear at points of high lattice strain energy such as slip-line intersections, deformation twin intersections, and in areas close to grain boundaries. It’s customary to define the nucleation frequency, N, as the number of nuclei that form per second in a cubic centimeter of unrecrystallized matrix because nuclei can’t form in the volume which has already been recrystallized. The linear rate of growth, G, is defined as the time rate of change of the diameter of a recrystallized grain. The ratio of the rate of nucleation N to the rate of growth G, N/G, is frequently used to predict the recrystallized grain size. If the ratio is high, many nuclei will form before the recrystallization process is completed, and the grain size will be finer. On the other hand, a low ratio corresponds to a slow nucleation rate relative to the growth rate and the final recrystallized grain size will be coarser.

The kinetics of recrystallization is normally described by the Johnson–Mehl–Avrami–Kolmogorov (JMAK) model. It is assumed that nuclei are formed at a rate N and that grains grow into the deformed material at a linear rate G. The fraction of recrystallized material (X_V) rises with time. However, the new grains will eventually meet each other and the rate of recrystallization will then decrease and tending to zero as X_V approaches 1 as shown in the following JMAK equation:

$$X_V = 1 - \exp(-Bt^n)$$

Where $B = fNG^3/4$ and n is known as exponent of time t, n is varying from 1-4 with growth dimensionality etc. factors, and N, G are constant with t. JMAK approach assumes that the nucleation sites are randomly distributed.

There are several models for nucleation of recrystallization nuclei: 1) Classical Nucleation (Fluctuation) Model [36], 2) Subgrain Growth Model by Sub-Boundary Migration [2, 37, 38], 3) Subgrain Coalescence Model [39, 40], 4) Strain-Induced Boundary Migration Model [41, 42], and 5) Inverse-Rowland Shear Mechanism [43-45]. Models 2), 3), and 4) are called the “Preformed Nucleus Models”. They don’t require the formation of a new orientation in the cold-work materials but are all based on the development of regions already present after deformation. All these models postulate that recrystallization occurs by the motion of high angle boundaries.

Model 2) Subgrain Growth Model and Model 3) Subgrain Coalence Model differ from Model 4) Strain-induced Boundary Migration in that the high angle boundaries responsible for the recrystallization are newly created (either during recovery or during the incubation stage), whereas the high angle boundaries responsible for recrystallization in Model 4) are the original high angle boundaries.

2.4.2 The methods to quantify the fraction of recrystallization

The microstructure at any time is divided into recrystallized or non-recrystallized regions, and the fraction recrystallized increases from 0 to 1 as the transformation proceeds. To study the progress of recrystallization, many methods to quantify recrystallization fraction have been used. Some traditional methods such as optical microscopy (OM), scanning electron microscopy (SEM) are based on visual measurement or image color and contrast analysis which is not accurate or take too much time. Modern methods based on E BSD data analysis differ the recrystallized area from unrecrystallized area by comparing their microstructural characters, which is a much more accurate and faster way.

The progress of recrystallisation was investigated using Vickers hardness measurements (1 kg), OM and SEM by Vanderschueren [8]. Using SEM micrographs, the fraction recrystallized was determined by an image analyzer. Image analysis was also used to evaluate the size distribution of the recrystallized grains in partially recrystallized material. The orientation of individual grain in deformed, partially recrystallized and fully recrystallized material was analyzed by EBSD.

Chen [46] used a new methodology for the determination of the recrystallized volume fraction from anodically etched aluminium alloys using optical microscopy. The method involves the creation of a composite image from multiple micrographs taken at a series of orientations. The results of quantitative analysis of images obtained by this new method are compared with those obtained using the traditional single image optical microscopy technique, orientation imaging microscopy (OIM) and microhardness indentation. The multiple orientation image method is shown to consistently yield a recrystallized volume fraction which is significantly higher than that determined from a single image while multiple orientation imaging and OIM results are found to be in good agreement.

Liu [47] showed that the recrystallization kinetics can be investigated by X-ray diffraction and measurements of hardness. The variation in texture volume fractions with annealing time reflects better the progress of recrystallization. The JMAK exponent and the activation energy for recrystallization derived from texture data are in good agreement with those from hardness data. Monitoring the change of texture volume fractions during annealing is shown to be a feasible method of determining the recrystallization kinetics.

Mitsche [48] used two methods to differentiate between the recrystallized and the deformed structure. One is based on the Image Quality (IQ) and the other is based on the misorientation [49, 50].

A method based on EBSD has been developed by Lu [51] to differentiate recrystallized from unrecrystallized grains in partially annealed samples based on the point-to-point misorientation within the grains. Recrystallized grains exhibit a low average point-to-point misorientation whereas the contrary is the case for deformed grains. The analysis for recrystallized fraction was calibrated based on this distinguishing feature, and it was found that the average point-to-point misorientation within a grain in a fully recrystallized sample was less than 0.7. Based on this calibration, partially recrystallized samples were analyzed for their degree of recrystallization, and the technique was validated using microhardness measurements. The analysis of the misorientation data was in excellent agreement with the hardness data.

A new experimental method of determining the volume fraction of recrystallized structure in a polycrystalline material has been developed by Field [52]. This method is based upon the comparison of electron backscatter diffraction patterns from adjacent locations in a polycrystal. Positions along a line are tested to determine whether adjacent points have the same crystal lattice orientation indicating that no dislocation structure exists between the two locations. If the distance between the two positions is relatively small, it is assured that the two points lie within a region of essentially defect-free lattice. Scanning through a region of material in this manner yields the lineal fraction of recrystallized material which directly correlates with the volume fraction. This automatic measurement eliminates the subjectivity and human error always associated with the quantitative determination of fraction recrystallized in a material.

Kernel average misorientation distribution maps from EBSD data were used in this study to quantify the fraction of recrystallized area. The maps can be formed using TSL OIM analysis software by processing the original EBSD scanning data. The misorientation between a grain at the center of the kernel and all points at the perimeter of the kernel are measured. The local misorientation value assigned to the center point is the average of these misorientations. For a given point, the average misorientation of that point with all of its neighbors is calculated with the proviso that misorientations exceeding some tolerance value (Maximum misorientation) are excluded from the averaging calculation.

2.5 GRAIN GROWTH

Grain growth is the process involving the migration of grain boundaries when the driving force for migration is solely the reduction of the total grain boundary energy. Coarsening can take place by either ‘normal’ grain growth, whose main mechanism is the disappearance of the smallest grains in the distribution, or ‘abnormal’ grain growth. The latter process involves the growth of a few grains which become much larger than the average. The driving force for grain growth is a reduction in the energy which is stored in the material in the form of grain boundaries. Grain boundaries and the surface energy will be both reduced after grain coursing. Some dramatic texture changes are usually associated with abnormal grain growth [53]. Amongst the best known examples is that associated with abnormal grain growth in rolled copper sheet, where the cube texture is replaced by new orientations generated by a 30°–40° <111> rotation [54, 55].

2.6 TEXTURE

Many mechanical and physical properties of crystals are anisotropic, and therefore the properties of a polycrystalline aggregate will depend on whether the individual grains or subgrains, which comprise the sample, are randomly oriented or tend to have some preferred crystallographic orientation. The sum of the crystallographic orientations of the crystallites within a polycrystalline aggregate is known as the texture of the material.

2.6.1 Deformation texture

The orientation changes that take place during deformation are not random. They are a consequence of the fact that deformation occurs on the most favourably oriented slip or twinning systems and it follows that the deformed metal acquires a preferred orientation or texture.

In a single crystal subjected to a particular stress state, plastic flow can be accomplished by slip on one or more particular slip systems. For a given stress state, the various potential slip systems are generally oriented differently with respect to the principal stress axes; therefore, the resolved shear stress, γ_{RSS} , on each slip system will be different. Plastic flow is initiated by slip on those systems where γ_{RSS} reaches a critical value characteristic of the material. This critical stress is denoted γ_{CRSS} and is related to the tensile yield stress, σ_y, through the expression:

$$\sigma_y = m\tau_{CRSS}$$

This is known as Schmid's law. The parameter m is a geometrical factor which is derived from the orientation of a particular slip system with respect to the stress state. While the Schmid factor, 1/m, is useful for identifying which slip systems are most likely to be activated for a single crystal of a given material, most materials are polycrystalline and an average Schmid factor is needed to predict the response of a textured polycrystal to a given stress state. The Taylor model describes deformation in polycrystals based on slip in the individual crystals. The model can be used to predict the evolution of texture during deformation. In metals, deformation is accomplished through slip on specific slip systems. Which slip systems are active is a function of their orientation relative to the imposed macroscopic stress state. A Taylor Factor is a geometric factor which describes the propensity of a crystal to slip (or not slip) based on the orientation of the crystal relative to the sample reference frame. In this sense, the Taylor factor is a multiplication factor on the yield strength of an individual crystal. The key assumption in the Taylor model is that of uniform strain within each constituent crystal equal to the macroscopic strain.

The family of close-packed planes in FCC is {111}. There are four such planes in a FCC crystal: (111), (-111), (1-11), (11-1). The close-packed directions are the slip directions which are <-110>. There are three such directions for each slip plane, e.g. for the plane (111) the slip directions are: [-110], [0-11] and [10-1]. Thus there are 4 slip planes with each having 3 slip directions, a total of 12 slip systems for FCC crystals.

The close-packed directions in BCC crystals are <111>. There are no close-packed planes in BCC. However, there are three types of planes that can be considered close-packed. They are nearly equal for the highest packing density planes in BCC: {110}, {321}, {211}. All of these planes have been observed to be slip planes. Thus we have the following slip systems in BCC crystals: 6 {110} planes each with 2 <111> directions, 24 {321} planes each with 1 <111> direction, 12 {211} planes each with 1 <111> direction, i.e. a total of 48 slip systems for BCC crystals.

Many models have been attempts to predict the evolution of textures during deformation. The Sachs model [56] assumed that each grain deforms independently of its neighbours and on the slip system that has the greatest resolved shear stress, i.e. in precisely the manner of an unconstrained single crystal of the same orientation. In these circumstances a crystal (grain) deforms on the most highly stressed slip system. The Taylor model [57] assumed that all grains undergo the same shape change. The strain tensor is always symmetrical and together with the constant volume requirement for plasticity gives five independent strain components. Taylor assumed that the combination of slip systems selected for a grain during an increment of deformation was that which achieved the required strain with the minimum internal work. The choice of the five active systems of the 12 total determines the grain rotation path during deformation.

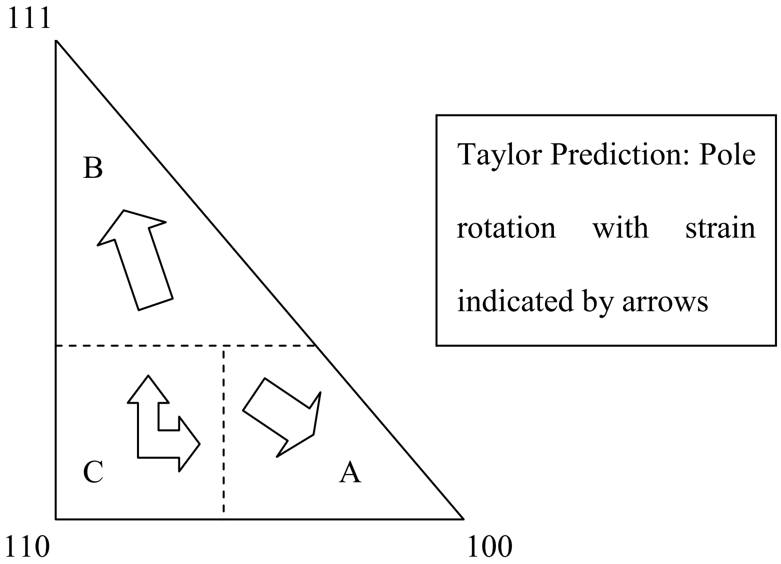

Figure 2. Pole rotation prediction by initial Taylor theory

Figure 2 shows the behavior assumed by initial Taylor theory for FCC structures, which predicted that poles initially in region B will rotate toward <111>, poles in region A rotate toward 100 and poles in region C rotate out of C toward either <100> or <111> (i.e., C is an unstable region). All of the rotations will deplete poles in region C and enrich poles in regions A and B, i.e. Taylor theory predicted <111> and <100> fiber texture for FCC structures. Taylor theory treated only simple glide or perfect slip and treated all 12 slip systems per crystal the same.

Some experimental results [58] related to stacking fault energy (SFE) couldn't be explained by this theory. Chin's group [58-60] challenged the Taylor theory's basis of simple glide of perfect dislocations. Dislocation theory predicts four different forms of shear deformation: Cross Slip or Collinear Slip (shearing in one <110> direction but on two {111} planes), Co-Planar or Latent Hardening Slip (shearing in two <111> directions concurrently), Deformation Faulting (shearing in <112> by Shockley partial dislocations), and Mechanical Twinning (shearing by {111} <112> twins). These forms of shear deformation were incorporated into the rotation calculations. Rotation calculations showed that by invoking Collinear Slip caused region C to be depopulated as per Taylor, but most poles rotating towards <111>, not <100>, and not equally as per Taylor. Hence high ratio <111> to <100> in high SFE metals/alloys, or less <100> than predicted by Taylor model. Coplanar or latent hardening slip favored in metals with low SFE. Pole rotations in Taylor region C for coplanar slip about the same as found for collinear slip (less <100> than predicted by Taylor). Results for deformation faulting favored a strong <111> texture enrichment in low SFE metals, reinforcing the trend found in coplanar slip in low SFE metals. For Mechanical Twinning, Chin recognized the very large difference in crystal orientation between untwined normal lattice and twinned region. He concluded that this could not be treated with Taylor theory. Ahlborn and Wassermann [61] found a large amount of <100> in drawn Ag crystals which they attributed to twinning. They suggested that the initial deformation of Ag favors very high <111> which with continuing deformation rotates to <511> during twinning. Continuing deformation then rotates this <511> to <100>. Hence the final high <100> is due to a slip + twin + slip process. But if this were true, the very low SFE metals-alloys would also have a high <100>, which they do not. Hence, Chin thought Ahlborn and Wassermann needed more refinement. If the crystal twinned too early in the deformation, there would not be enough enrichment at <100> via slip to lead to final high <100> from the subsequent twinning. Chin suggested that extensive slip must first occur in Ag to both a) build up the internal energy of the material to eventually allow twinning to occur, and b) to allow enough poles to be accumulated near <100> due to the initial slip such that a very high concentration would be found near <111> after twinning and later slip in the final crystal. A later development was the formulation of the so-called relaxed constraints model [62, 63] to account for the deformation of non-equiaxed grains. This term is used in order to distinguish such models, which allow the operation of less than five independent slip systems, from the full constraints model of Taylor and the zero constraints model of Sachs. Like these the relaxed constraints models assume that slip is homogeneous within a grain and that any effects of individual location within the microstructure can be ignored, i.e. all grains of the same orientation behave similarly. In attempting to make better predictions of the nature and rate of formation of deformation textures, more recent models abandon the assumption of homogeneous strain, and use a variety of methods to predict textures. Self-consistent models [64] used a mean field approach in which the deformation of each crystallite is considered individually within the surroundings of a homogeneous matrix. Crystal plasticity finite element models [65] used finite element methods, but include constitutive crystal plasticity equations. They can take account not only of nearest neighbour grain interactions, but also long-range interactions. However, they are very computer intensive.

2.6.2 Recrystallization texture

If the deformed metal is subsequently recrystallized, nucleation occurs preferentially in association with specific features of the microstructure, i.e., with regions of high stored energy and particular orientation. The ability of the nucleus to grow may also be influenced by the orientations of adjacent regions in the microstructure. The changes in texture that occur during the recrystallization process can be dramatic in the sense that the previous texture of the deformed state is, in some cases, replaced by an entirely different texture. The purity of a particular metal may also strongly influence the recrystallization texture. In many cases very small amounts of second elements may, by affecting the boundary mobility, change the annealing texture completely.

2.7 PRECIPITATION BEHAVIOR

2.7.1 The effects of different alloy additions on the annealing behavior or steel properties

The chemical elements niobium, titanium and vanadium are very effective as microalloying additions in steel, influencing the microstructure by both a solute drag effect and the formation of nitrides and carbides precipitates. Since the solubility products and the physical properties of each element and each compound are different, they have some different characteristics, which cause each of these elements to have specific merits. Niobium and titanium addition effects will be compared in this study.

Niobium continues to play a major positive role in optimising the manufacturability, final properties and performance of the niobium bearing steels. Niobium is often used as a stabilizing element in sheet steels, often in combination with titanium, whereby carbides are formed thus reducing the amount of free carbon in solid solution, in both ultralow carbon steel and ferritic stainless steel. Niobium is normally recognized as the most effective microalloying addition which is due to its features. In the ternary Fe–C–Nb system, the major feature of the equilibrium diagram relevant to steels is the marked reduction of the solubility of carbon in austenite and ferrite as a result of the ready formation of niobium carbide. Niobium shows a strong tendency to form carbonitrides, but relatively little tendency to form oxides, sulphides, or solid solutions of these compounds. In this regard it behaves similarly to vanadium. This characteristic distinguishes it from titanium which does not act as a carbide former until all oxygen, nitrogen, and sulphur have been consumed by initial additions of titanium. Niobium carbo-nitrides can readily be dissolved completely prior to hot rolling at temperatures between about 1200°C to 1320°C that correspond to a commonly used slab reheating temperature range. Precipitation could be formed during cooling or formed during or after rolling between about 1000°C and 900°C that correspond to a commonly used temperature range for the completion of the hot rolling process. Precipitation during cooling is not likely to be significant, since precipitation in recrystallized austenite is normally very sluggish. Precipitation during or after rolling is the strain induced precipitation which could produce marked retardation of recrystallization. Dissolved niobium produces the largest effect on retarding recrystallization in comparison with any other microalloying elements. Solubility of carbo-nitrides at low temperatures in the austenitic range is very limited, practically precluding precipitation strengthening.

Since titanium carbide will not be formed before all oxygen, nitrogen, and sulphur have been consumed by initial additions of titanium, the effects of titanium on microstructure are strongly dependent on the amount of titanium added. Addition of a small amount of titanium produces titanium nitrides, TiN, having extremely limited solubility. The extremely stable titanium nitride practically does not dissolve at the soaking temperature, thus precluding any solid solution effect of titanium on recrystallization. The stability of the titanium nitride also precludes any noticable strain inducement. The recrystallization kinetics of steels with additions of up to 0.04wt% titanium is similar to those of plain carbon steel. Addition of a greater amount of titanium to low carbon steels provides an ability to form titanium carbides, in addition to the stable titanium nitrides that are naturally formed due to the presence of nitrogen in steels. Subsequently, the steel reproduces the effects seen in niobium steels. These effects include both a retardation of recrystallization of γ due to dissolved titanium and a strain induced precipitation over the temperature range l000°C - 850°C peaking at 900°C. Titanium readily forms a sulfide or carbo-sulfide in competition with manganese for sulfur. At low titanium levels (or high manganese levels), manganese sulfide is formed with titanium in solid solution. Conversely, the more stable titanium sulfide is formed at low manganese levels. The titanium sulfides are hard particles that are non-deformable under hot rolling conditions. They change the sulfides from elongated ovoid to sphere, leading to a significant improvement of steel ductility. With sufficient amount of titanium addition, Ti-based precipitation could be formed during annealing of cold rolled steels, which will retard recovery and recrystallization processes [66].

2.7.2 The mechanism of precipitation behavior

Second-phase particles may either have been present before the deformation of the material, in which case they are often distributed reasonably uniformly in the microstructure, or they may precipitate during the anneal, in which case their distribution is often related to the dislocation structure.

If the processes of recrystallization and precipitation occur concurrently, the situation is very complex for the following reasons: 1) the presence of a deformed microstructure may affect the nature and kinetics of the precipitation; 2) the presence of precipitates may interfere with recovery and recrystallization. The problem was first analyzed by Hornbogen and colleagues in

Al–Cu and Al–Fe alloys, e.g. Ahlborn et al. [67], and was reviewed by Hornbogen and Koster [68].

Solubility diagrams have been used to help explain the physical metallurgy of microalloyed steels and, in particular, the precipitation phenomena [69-71]. The largest possible supersaturation occurs when the microalloying element and the interstitial are present in the steel in the stoichiometric ratio, and deviation from this ratio will lead to decreasing supersaturation [72]. Solubility products can be in influenced by the presence of elements that do not directly participate in the precipitation reaction. Third elemental solutes that raise the activity of niobium or carbon through a positive interaction coefficient decrease their solubility, while those that decrease the activity through negative coefficients increase it [73, 74]. Although the use of solubility products is helpful in understanding the behaviour of microalloying elements in austenite and ferrite, there are some important restrictions that must be recognized when applying them. many precipitate reactions are governed by a local composition rather than a bulk composition the influence of segregation on precipitation must be considered when applying any solubility equation, as discussed by Palmiere [73].

2.7.3 The difference between precipitates in austenite and precipitates in ferrite

Through TEM investigation of the orientation relationship between the carbide and the matrix, it is possible to determine if the carbide formed in ferrite or austenite. This is important in determining the temperature where the carbide forms, and also in determining the presence of austenite in the temperature range where the precipitation occurs. The carbide will conform closely to either the Kurdjumov-Sachs orientation relationship or the Baker-Nutting Orientation relationship as described in the following sections.

Baker-Nutting Orientation Relationship

The Baker-Nutting orientation relationship [75] describes the relationship between a carbide particle and the matrix when the carbide precipitates in the ferrite. The B-N relationship is shown schematically in Figure 3 and can be shown as:

$$(100)MC \parallel (100)\alpha$$

$$[100]MC \parallel [110]\alpha$$

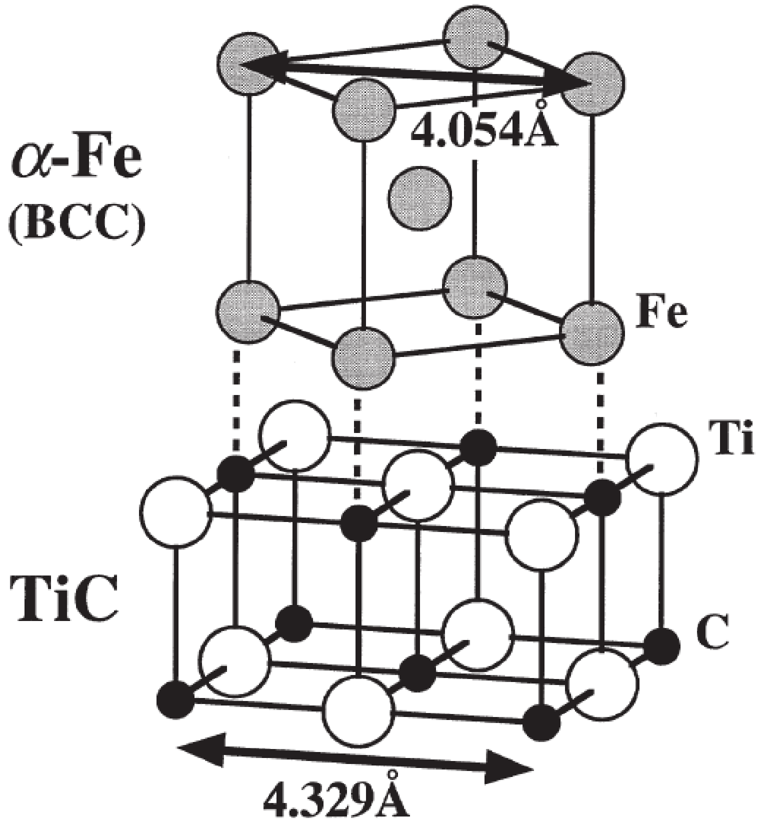

Figure 3. Schematic of the Baker-Nutting orientation relationship between a titanium carbide particle and the ferrite matrix

Kurdjumov-Sachs Orientation Relationship

The Kurdjumov-Sachs orientation relationship [76] is used to describe the orientation between an FCC lattice and a BCC lattice. When this occurs, the close packed planes between the two crystal structures will be aligned as shown in Figure 4 so that:

$$(110)\mathrm{BCC} \parallel (111)\mathrm{FCC}$$

$$[111]\mathrm{BCC} \parallel [110]\mathrm{FCC}$$

where (110) is the close packed plane in BCC and (111) is the close packed plane in the FCC.

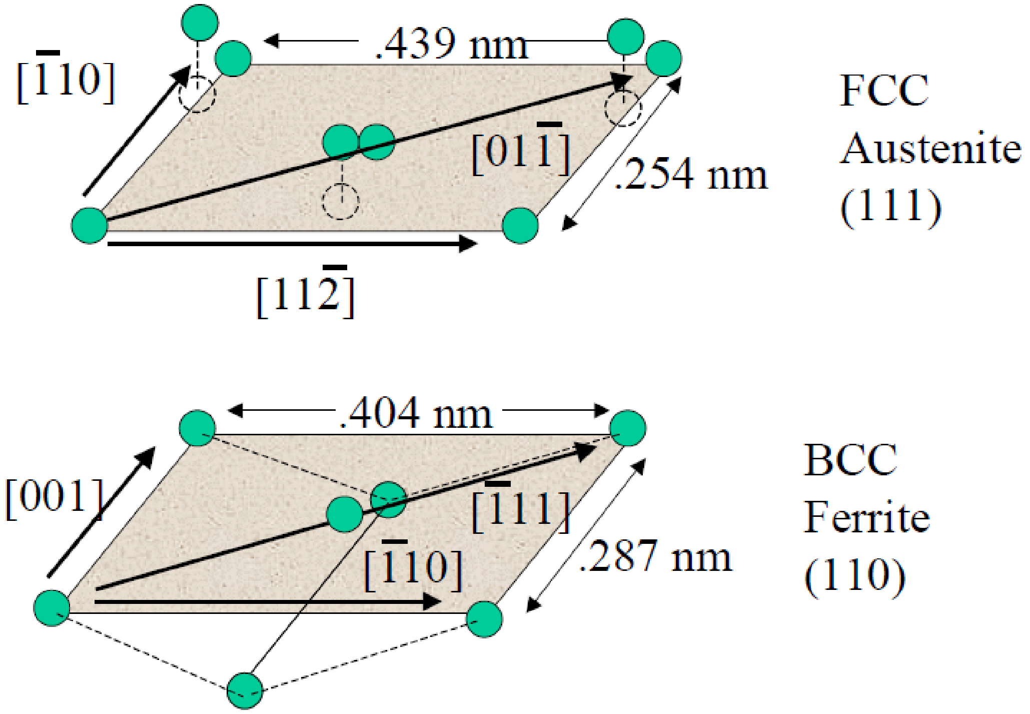

Figure 4. Schematic showing the parallel planes and directions in the Kurdjumov-Sachs orientation relationship between ferrite and austenite

This orientation relationship has been observed at ferrite/austenite grain boundaries. This orientation relationship can also be used to indicate the precipitation of carbides in the austenite phase. Carbides will initially form in austenite with NaCl lattice parallel to that of the FCC austenite:

$$(100)\mathrm{MC} \parallel (100)\gamma$$

$$[010]\mathrm{MC} \parallel [010]\gamma$$

The austenite/ferrite boundary will then move past the particle, leaving the particle with the K-S relationship with respect to the matrix.

2.7.4 Pinning force of precipitates

The effects of particles on recrystallization are complex. During deformation, particles will affect the deformation microstructure and texture through effects such as an increase in dislocation density, the production of large deformation heterogeneities at larger particles, and the alteration of the homogeneity of slip, e.g., shear bands. During annealing, the primary effect of closely spaced particles is to pin grain boundaries (Zener pinning), but the deformation heterogeneities at large particles may be sites at which recrystallization originates (particle stimulated nucleation or PSN). Second-phase particles may either have been present during the deformation of the material, in which case they are often distributed reasonably uniformly in the microstructure, or they may precipitate during the anneal, in which case their distribution is often related to the dislocation structure. Second-phase particles may affect recovery mechanisms in several ways. During the annihilation and rearrangement of dislocations to form low angle boundaries, the particles may pin the individual dislocations and thus inhibit this stage of the recovery. There is substantial evidence that a fine particle dispersion may exert a strong pinning effect on subgrains (Humphreys and Martin [77], Ahlborn et al., [67], Jones & Hansen [78]). Particle-limited subgrain growth may have a significant effect on the recrystallization behavior of an alloy. A dispersion of particles may hinder the recovery processes involved in the initiation of recrystallization. Precipitation on the recovered substructure may occur during the annealing of a supersaturated alloy. In this situation, the precipitation generally occurs on the low angle boundaries. Such non-uniformly distributed precipitates exert a strong pinning effect on the boundaries. It has long been established that recrystallization is prevented or delayed by a dispersion of closely spaced second-phase particles, due to the pinning (Zener drag) of both high and low angle boundaries. The influence of the particles is expected to depend on a number of factors and, in particular, on whether the particles are present during deformation or whether they form during the subsequent anneal before recrystallization occurs. At high annealing temperatures, recrystallization is likely to be complete before precipitation occurs and the particles, therefore, do not influence the recrystallized microstructure and texture. At lower temperatures, precipitation generally occurs before recrystallization and precipitates form on the deformed or recovered substructure, thereby inhibiting both recovery and recrystallization [79].

2.7.4.1 Grain boundary migration during annealing

The migration of low angle (LAGB) and high angle grain boundaries (HAGB) play a central role in the annealing of cold worked metals. Low angle boundary migration occurs during recovery and during the nucleation of recrystallization, and high angle boundary migration occurs both during and after primary recrystallization. Low angle and high angle grain boundaries migrate by means of atomistic processes which occur in the vicinity of the boundary. The mechanism of boundary migration depends on several parameters including the boundary structure which, in a given material, is a function of misorientation and boundary plane. It also depends on the experimental conditions, in particular the temperature and the nature and magnitude of the forces on the boundary, and it is also strongly influenced by point defects in the material such as solutes and vacancies. It is well established that low angle grain boundaries migrate through the movement by climb and glide of the dislocations which comprise the boundary. Because the atomic packing at grain boundaries is less dense than in the perfect crystal, grain boundaries are associated with a free or excess volume which depends on the crystallography of the boundary. This leads to a strong interaction with solute atoms and to the formation of a solute atmosphere which, at low boundary velocities, moves with the boundary and impedes its migration. The range of boundary velocities is very large. For example, in the case of grain growth the boundary may move relatively slowly through an almost perfect crystal. However, during recrystallization, the boundary moves at a very high velocity (often much higher than during diffusion-controlled phase transformations). In this case, the boundary migrates into highly defective material, leaving a perfect crystal behind it.

Kronberg and Wilson [54] showed that rotation about a common <111> and <100> axes are such that lattices of new and old grains have a common sublattice, this kind of sublattice is called the coincidence site lattice (CSL) because the points coinside with both the new and old lattices. The points take two crystals and the number of coincident sites will vary if the lattices are rotated. There are some special orientations in which the number of coincident sites is abnormally high. The special boundaries like twist or tilt boundaries have the Kronberg-Wilson (K-W) orientations. K-W boundaries are good fit boundaries, so they absorb considerably less impurities than bad fit random boundaries. The tendency to absorb the impurities also is temperature dependent. The absorption is low at high temperatures and high at low temperatures. Therefore, at high temperatures, neither K-W nor random boundaries would be expected to be strongly influenced by solutes; at low temperature, random boundaries become impurity laden and migration rate falls well below that of the random boundary in a pure matrix.

A dispersion of particles will exert a retarding force or pressure on a low angle or high angle grain boundary and this may have a profound effect on the processes of recovery, recrystallization and grain growth. The effect is known as Zener drag after the original analysis by Zener which was published by Smith [80]. The relationship can be described as following Zener pinning pressure equation:

$$P_Z = \frac{3F_V\gamma}{2r}$$

The magnitude of this interaction depends the nature of the particle and interface, and the shape, size, spacing and volume fraction of the particles. In some situations the second-phase particles may be precipitated after the formation of a grain or subgrain structure. In this case the particles are unlikely to be distributed uniformly and will form preferentially on the boundaries. The pinning pressure due to the particles will therefore be greater than for a random particle distribution (Hutchinson and Duggan [81]).

A dense dispersion of very fine precipitates is believed to exert a strong pinning force exerted on the grain boundary to retard the growth of these grains. Similar conclusions were drawn by Hellman [82] and Hillert [83] for various materials. In addition, Hu [84] also pointed out that impurities, solutes or fine second phase particles inhibit boundary migration to retard recrystallisation.

2.7.4.2 Ti-Based Precipitates

Wei [85] used high-resolution electron microscopy to examine the crystallography and morphology of TiC particles. Plate-like TiC precipitates with a thickness ranging from a few atomic layers to 20nm were observed in steels. It was found that the Baker–Nutting orientation relationship is always satisfied with the ferrite matrix within about 5° for both the nanosized and the coarse TiC particles. The habit plane of the TiC precipitate is the (100) ferrite plane. A moderate tendency for the faceting of lateral interfaces on the {001} and {011} ferrite planes was found. The presence of interfacial misfit dislocations was revealed by examining the excess lattice fringes terminating at the interfaces between the TiC platelet and the ferrite matrix. The location and number of the excess lattice fringes terminating at the broad plane and the lateral interface were consistent with the mismatch in the atomic arrangement between the Baker–Nutting orientation relationship related TiC and ferrite.

Zhou [86] used transmission electron microscopy (TEM) and physics-chemical phase analysis to investigate the precipitates in high strength steels microalloyed with Ti produced by compact strip production (CSP). It was seen that precipitates in Ti microalloyed steels mainly included TiN, $Ti_4C_2S_2$, and TiC. The size of TiN particles varied from 50 to 500 nm, and they could precipitate during or before soaking. The $Ti_4C_2S_2$ with the size of 40-100 nm might precipitate before rolling, and the TiC particles with the size of 5-50 nm precipitated heterogeneously. High Ti content would lead to the presence of larger TiC particles that precipitated in austenite, and, by contrast, TiC particles that precipitated in ferrite and the transformation of austenite to ferrite were smaller. They were less than 30 nm and mainly responsible for precipitate strengthening. It should be noted that the TiC particles in higher Ti content were generally smaller than those in the steel with a lower Ti content.

Belyakov [66] studied the development of primary recrystallization in a steel containing 0.4 volume% of fine TiC precipitations with an average size of 12 nm. After sufficiently large cold strains, the recrystallization developed readily upon annealing at temperatures above 600 °C. An increase in the cold strain as well as the annealing temperature resulted in the acceleration of recrystallization kinetics. However, a certain amount of cold worked microstructures of about 15 volume% remained unrecrystallized even after annealing at a rather high temperature of 700°C. The unrecrystallized portions were composed of grains with the <0 0 1> crystallographic direction parallel to the compression axis. Both the low stored energies in these grains and the pinning of recrystallizing grain boundaries by the dispersed carbides were discussed as crucial factors that resulted in the incomplete recrystallization.

2.7.4.3 Nb-Based Precipitates

The precipitation of Nb carbonitrides in ferrite is widely used in steels, especially for two main applications: for low solute contents (IF steels), the precipitation of NbC improves the drawability by removing C and N atoms out of solid solution [87]; for higher solute contents (HSLA grades), the precipitation of Nb carbonitrides provides important precipitation hardening [88, 89].

Small amounts of niobium in steels have been known to affect both the microstructure and properties. The niobium has been known to increase strength [90-92], develop good textures [93], improve surface quality [94], and increase formability [95]. The main benefit of the niobium is its ability to suppress recovery, recrystallization, and grain growth in steels [96]. This occurs from both niobium in solid solution and niobium in precipitates. The topic of niobium in steels has been covered extensively in a review paper by DeArdo [97].

In Hutchinson's paper [98], the comparative effectiveness of solute Nb and NbC particles at impeding grain-boundary motion is treated theoretically. Nb is often considered to be a powerful alloying element for controlling the recrystallization processes in steel and is of considerable technological importance. However, the Nb can be present both as solute in solution, where it is thought to exhibit a strong solute drag effect, or as NbC precipitates, which are thought to be effective at pinning grain boundaries. It is shown that, for a steel containing ~0.05 at.% Nb (~0.1 wt.% Nb), under typical recrystallization conditions, solute Nb is more effective in the ferrite, whereas in the austenite, depending on the exact recrystallization temperature, either solute Nb or NbC precipitates may be more effective.

3.0 STATEMENT OF OBJECTIVES

Batch annealing is still widely used in industry to soften cold rolled steels and improve their mechanical properties. The different thermal profiles throughout the coil cause non-uniform properties after annealing. The main objective of this study is to gain a fundamental understanding of the factors responsible for the kinetics of annealing behavior during batch annealing for high strength low alloy (HSLA) steels, which will lead to solve the practical problems during commercial production. Certain factors such as alloy composition (Ti-bearing and Nb-bearing), cold rolling reduction rate, texture, heating rate (Cold Spot Temperature profile and High Spot Temperature profile) and soaking time, which may influence the annealing behavior, will be considered in this study. How solute drag and/or precipitation would affect the start temperature (T_{Start}), the end temperature (T_{End}) and the kinetics of recrystallization will also be studied. These factors influence the annealing behavior at different levels, texture dependent stored energy distribution and the Zener pinning force of precipitates are expected to have more significant effects than other factors and will be extensively studied. Finally, suggestions should be made on eliminating or reducing the difference in annealing results between the outer and inner coils and the difference annealing behavior between Ti-bearing steels and Nb-bearing steels.

4.0 EXPERIMENTAL PROCEDURES

4.1 CHEMICAL COMPOSITIONS

The steel samples used in this study are listed in Table 1. The main difference between the two types of steels is that one contains significantly higher Ti and the other contains significantly higher Nb and a little higher Mn. Different alloy compositions were specially designed for different application, the reason we compare these two kinds of steels was that the annealing uniformity were different for them although the problem existed in both kinds of steels. The purpose was to compare what factors made that kind of difference and what could be done to improve the one with the worst uniformity.

Table 1. Chemical compositions of experimental steels used in this study (wt%)

Type	C	Si	Al	Nb	N	Mn	V	Ti
Ti-bearing	0.0455	0.1909	0.0410	0.0027	0.0086	0.7296	0.0039	0.0577
Nb-Bearing	0.0526	0.1938	0.0191	0.0317	0.0073	1.0680	0.0019	0.0097

4.2 DETAILED PROCEDURES

The hot band samples were cold rolled with different desired cold rolling rate at room temperature in the factory. Both hot band and cold rolled samples were supplied from commercial sources. Samples were cut into small pieces about 3cm in length and 2cm in width.

To prevent oxidation during annealing, the samples were encapsulated individually in quartz tubes or chemically plated with one layer of Ni. The T_{Ac1} of the steels were first measured by a dilatometer. The annealing soaking temperature was then determined by the T_{Ac1}. T_{Ac1} minus 10, 20, 30 degree C were as the annealing soaking temperature. The T_{Ac1} for different alloy composition steels are slightly different, to simplify the experiments and do a better comparison, 670°C was selected as a common annealing temperature for most samples. About 10 to 15 small piece samples were put into the furnace at the same time. Two annealing processes were simulated, one is called cold spot temperature (CST) the other is called hot spot temperature (HST). The main difference for these two processes are heating rates and soaking time. The CST simulates the temperature change for the center part of the coils, where the heating rate is lower and the soaking time is shorter. The HST simulates the temperature change for the surface part of the coils, where the heating rate is about 2 to 3 times higher and the soaking time is much longer. The whole annealing process would take about 80 hours. Please see Figure 5 for annealing cycles.

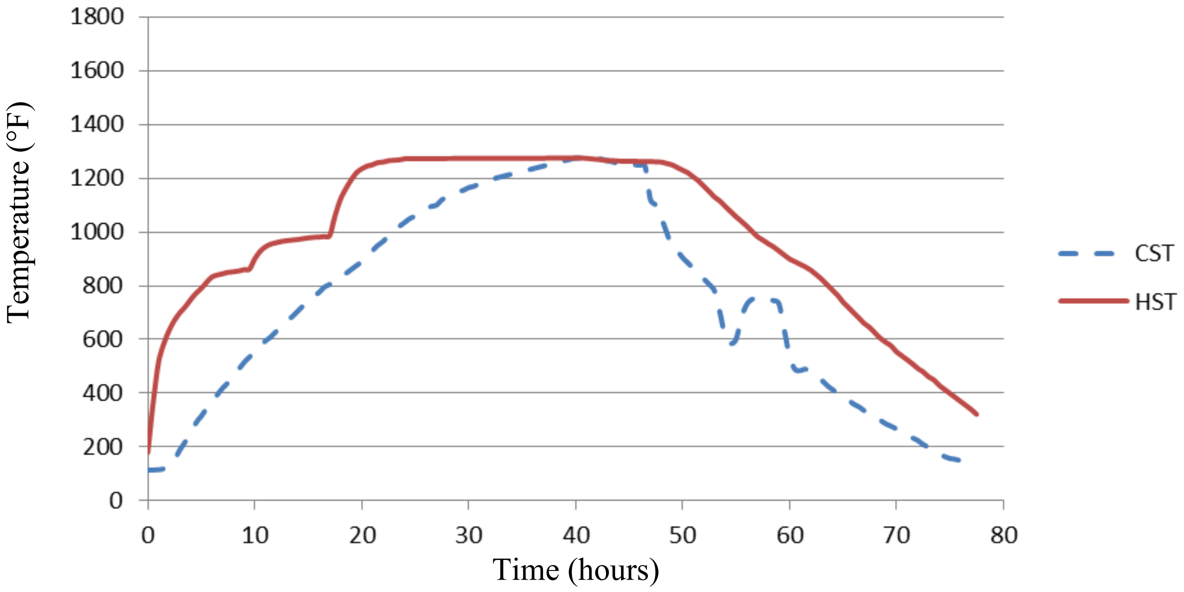

Figure 5. Simulated annealing cycles

After the test, it was found that the temperature in the furnace was relatively uniform and very well controlled. Also, the temperature of the samples and the temperature of the furnace were essentially the same during annealing because of the small size of our samples. So only the furnace temperature change was monitored. Small sample pieces were taken out one by one at different temperatures: 335°C, 400°C, 500°C, 600°C, 670°C and different soaking times: 1 hour, 2 hours, 4 hours, 6 hours etc. up to 30 hours, then water quenched to room temperature. To get more accurate recrystallization start temperature and precipitation start temperature, the experiment was refined from 520°C to 660°C with 20°C temperature intervals. Parts of these samples were cut again along rolling direction into smaller pieces about 10mm in length and 5mm in width and thermo mounted using bakelite or copper powder. The samples were then ground on 400 to 2400 grit silicon carbide abrasive paper and polished with 0.05 micron alumina power on abrasive cloths. The final polishing step used the vibratory polishing machine and 0.05 micron alumina power. Then the samples can be used for EBSD experiment directly; chemical polishing was needed sometimes for better surface condition. 2% to 5% Nital was used for etching when sample microstructure needed to be observed on OM or SEM. Microhardness (VHN) and nanohardness were measured after microstructural analysis. Other parts of the annealed samples were used for precipitation (PPTN) analysis in TEM (3mm diameter thin disk).

4.3 EQUIPMENT AND TECHNIQUES

4.3.1 Dilatometer

A Theta Dilamatic IIe dilatometer was used for determining T_{Ac1} in this research because of its computer controlled furnace with a semi-enclosed sample chamber. This furnace was utilized for heating and cooling experiments where the heating and cooling rates needed to be controlled. The furnace uses a resistance-heating element that can obtain heating rates of up to 10 °C per second. This furnace is interfaced to a PC through the serial port, allowing for two-way communication between the computer and the temperature controller. This allows the computer to record the temperature data from the controller, as well as continuously change the sample set point temperature and heating rate. The sample temperature is monitored through a k-type thermocouple spot welded to the surface of the sample. The sample is contained in a semi-enclosed quartz tube. The quartz tube had an opening at one end to allow the sample to be removed quickly and air or water quenched. Argon was introduced into the quartz tube to protect the heated samples from oxidation. Increasing the argon flow across the sample could also be used to obtain higher cooling rates.

4.3.2 Optical Microscopy (OM)

Optical Microscopy was first used to observe the microstructure and phase balance of the samples. Bulk samples were cut using a Buehler Isomet 1000 diamond cutting wheel and were then hot-mounted using copper powder in a Buehler Pnumet I mounting press. The samples were then ground on 400 to 2400 grit silicon carbide abrasive paper and polished with 0.05 micron alumina power on polishing cloths. The samples were etched using 2% Nital for 10-30 seconds. The time needed depends on the microstructures and chemical compositions of the samples. Optical micrographic images were captured using a Sony digital camera attached to a Nikon Microscope. Bioquant image analysis software was utilized to save the images on the computer in JPEG format.

4.3.3 Scanning Electron Microscopy (SEM) and Energy Dispersive X-ray Spectroscopy (EDS)

Samples for analysis on the SEM and EDS were prepared either as optical microscopy bulk samples or TEM thin foils. Most samples analyzed on the SEM were prepared as TEM thin foils even if they were not going to be analyzed in the TEM. There are three reasons for routinely preparing TEM foils for the SEM. The first is because the TEM foil preparation keeps the sample very clean which helps resolve small particles. Second, the twin-jet electopolisher tends to leave carbides and nitrides on top of the surface, facilitating good images and analysis of the particles. The final reason why TEM foils were usually prepared for SEM analysis was that it always left the option open for further analysis on the TEM. A Philips XL30 FEG SEM was used for analyzing larger precipitates and fine microstructures and the characters of second phase. Typical parameters for the SEM would be 15 kV and beam spot size 3. Elemental analysis was done using an EDAX CDU LEAP detector. Samples were in focus at a 10 mm working distance for all images and analyses. All SEM images were captured in TIFF compressed format.

4.3.4 Electron Back-Scattered Diffraction (EBSD)

EBSD experiments normally need a very good sample surface condition. TEM thin foils are also often used here for the same reason why we use them in SEM and EDS experiments. The other way is, after preparing steps as for optical microscopy samples, using vibration polishing and/or electropolishing to do the final refinement. The Vibromet 2 Vibratory Polisher is used for fine polishing. In this case, the total polishing time on the Vibromet 2 is from 1 to 12 hours depending on the sample hardness and desired surface condition. Standard operation procedure of EBSD observation is employed in this part of work. For every observation, 20kV voltage and the beam spot size of 6 are applied. The square scan mode is used for compatible with the analyzing software developed by Choi [15] to do stored energy distribution analysis. The step size is varied from 0.1μm to 0.5μm determined by the grain size and the features of interest. All data collection is accomplished by using the TSL OIM data collector software. General analysis of the EBSD data is conducted by using the TSL OIM Analysis software. Grain boundaries and subgrain boundaries can be determined and measured. Information on the texture of the specimens can also be calculated. Since the scanning area of EBSD is relative small, XRD has been done to determine the texture again to confirm or compare the results. Initially recorded data of the diffraction pattern image quality (IQ) and the confidence index (CI) may also be normalized and presented by using this software. EBSD-IQ analysis software previously developed by BAMPRI [18] were mainly used for analyzing the phase balance in this study.

4.3.5 Transmission Electron Microscopy (TEM)

For further analysis of small precipitates and to obtain crystallographic data, a transmission electron microscope (TEM), JEOL200CX and JEOL2100F, were used. The TEM uses tungsten filaments operated at 200 kV, 118 μA, and a beam spot size of 2. Thin foil samples preparation involves sectioning the samples, mechanical or chemical thinning, and electropolishing. Samples were first sectioned to 500-800μm in thickness using a Buehler Isomet 1000 diamond cutting wheel. The thin samples were then attached to a larger steel block using a hot plate and wax. Once the sample was mechanically ground on one side using 320, 400 and 600 grit silicon carbide paper the foil was again placed on the hot plate to melt the wax. The sample was turned over and then mechanically ground on the opposite side. After the sample was sufficiently thin (less than 200μm), chemical thinning will be done using an acid solution mixed from 50ml H_2O, 30ml HNO_3, 15ml HCl and 10ml HF. The foils should be thinner than 100μm after this step. These foils were then punched into 3 mm discs and gently polished using 600 or 1200 grit to get a shining surface. Then the disks were elecropolished until perforation using a Fischione twinjet electropolisher and the electrolyte solution is mixed from 80g Na_2CrO_3 and 400ml Acetic acid. Finally, the samples were cleaned using a three step ethanol cleaning process to remove all residues on the sample.

4.3.6 X-ray Diffraction (XRD)

A polished sample used for EBSD experiment is good for the XRD experiment. Philips Analytical X-Ray PW3710 based X'Pert Diffractometer systems were used to do phase and texture analysis in this study as a secondary method to compare the results to EBSD measurements.

4.3.7 Microhardness and Nanohardness

Microhardness and nanohardness measurements are the key to correlate the quantified microstructure and the mechanical properties of the microstructure. The typical loads used during the microhardness measurement in this study are 10 gram or 500 gram with the dwell time of 15 seconds. 10 gram is used for measuring the hardness of certain individual grain. A 500 gram load is used for measuring the hardness of the whole ferrite matrix including some grains and their grain boundaries. The changing trend of hardness during the annealing process shows the stages of recovery, recrystallization and grain growth. To complement microhardness results, nanohardness measurements will be performed on a Hysitron Triboindenter. Through nanohardness measurement in a pre-selected area, detail hardness information all over the microstructure can be collected. This measurement covers not only the grain boundaries, but also the grain matrix among these grain boundaries; the nanohardness is affected not only by the grain boundaries, subgrain boundaries, but also by the defect density and texture of the location of interest. The defect density and texture variation is certainly associated with different deformation level or recrystallization level. The nanohardness distribution maps can be used to compare with the SEM images and texture based stored energy distribution maps to determine microstructure and recrystallization fraction information.

5.0 RESULTS

Figure 6 show that the HSLA steel hot band samples with higher Nb & Mn concentration have smaller grain size and smaller ferrite volume fraction. The EBSD-IQ distribution charts in Figure 7 and Figure 8 also show the same results for the ferrite volume fraction. From Figure 9, we can see that the second microconstituent in the hot band Nb-bearing HSLA steel samples shows a typical pearlite structure. The different microstructures in the initial hot band state will cause different cold rolling microstructure and the total amount of stored energy, which will influence the annealing behavior of the cold rolled steels. We will discuss this kind of influence later.

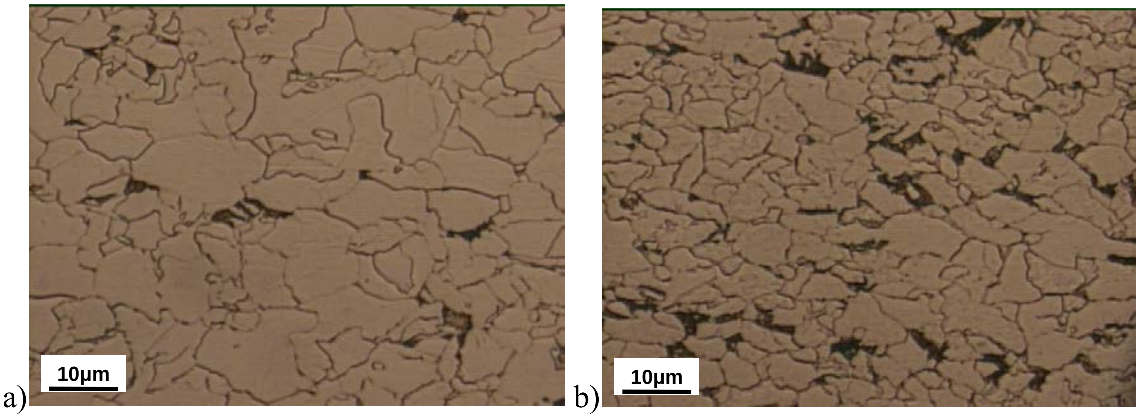

Figure 6. OM images of hot band samples: a) low Nb & Mn, high Ti, b) high Nb & Mn, low Ti

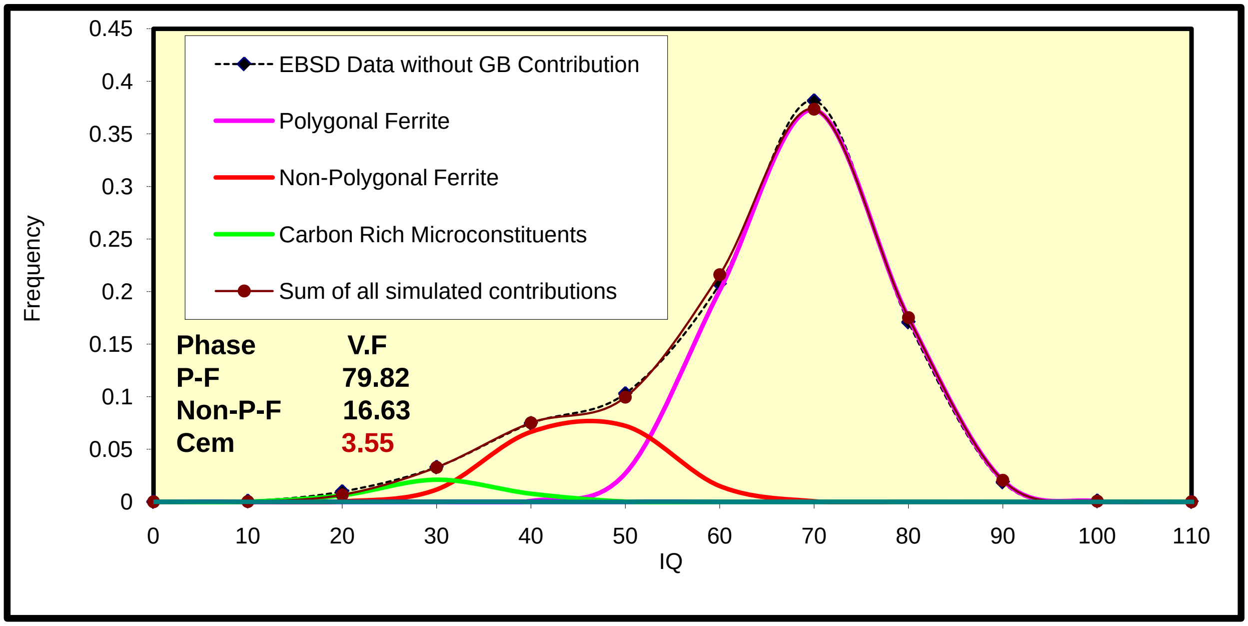

Figure 7. EBSD-IQ chart of low Nb & Mn, high Ti sample shows the volume fraction of carbon rich microconstituents is 3.55%

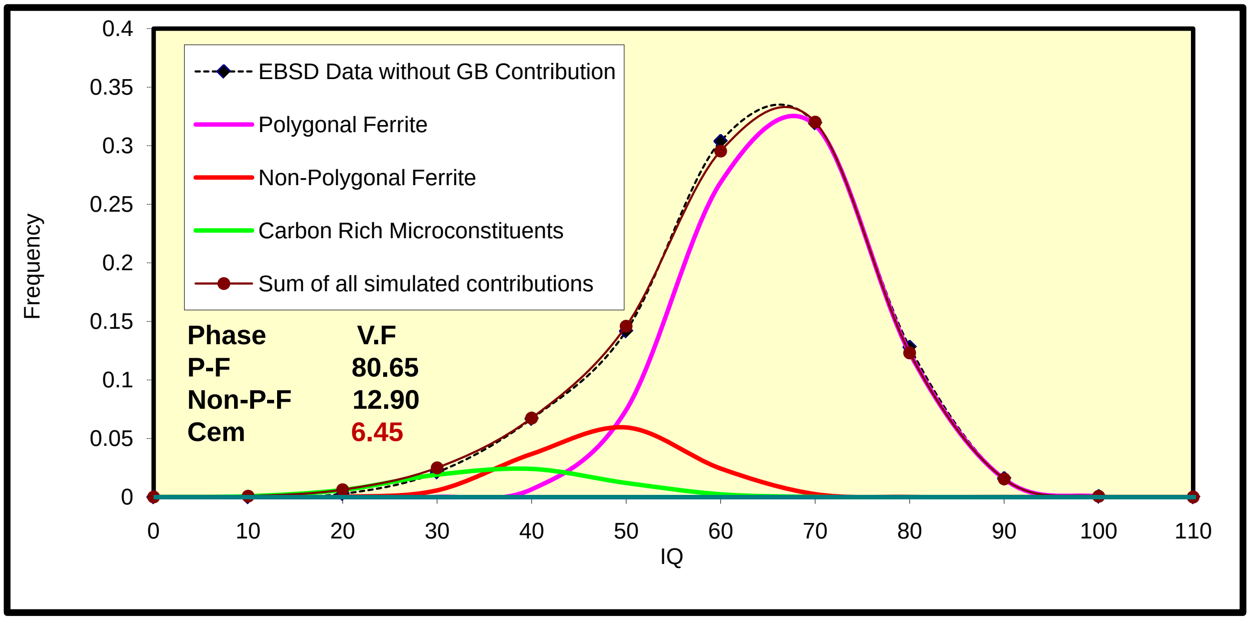

Figure 8. EBSD-IQ chart of high Nb & Mn, low Ti sample shows the volume fraction of carbon rich microconstituents is 6.45%

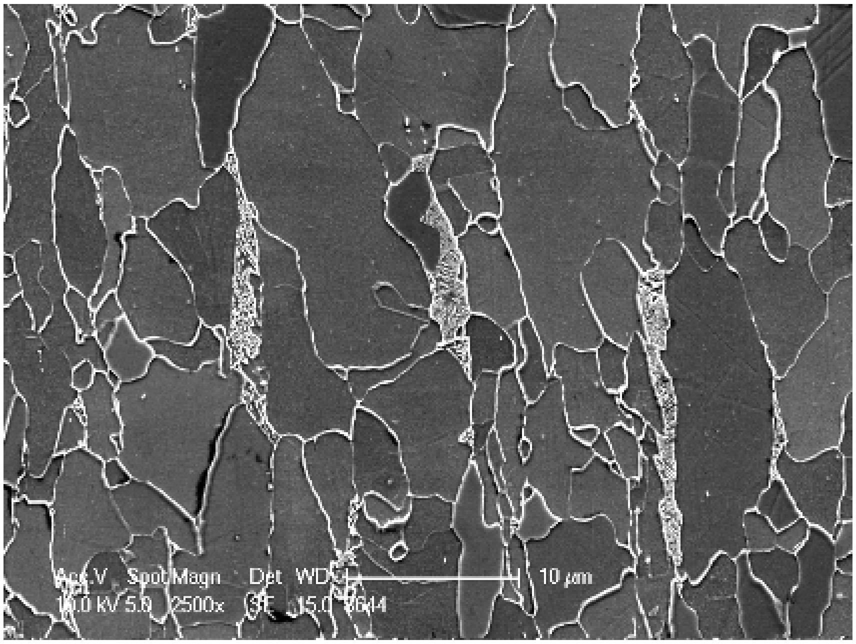

a) Magnification: 2500X (SEM)

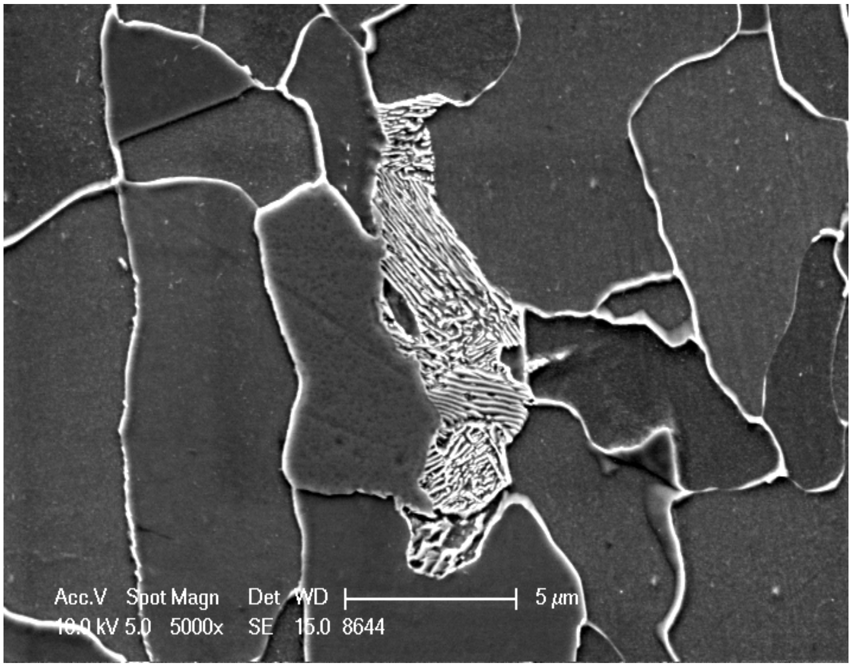

b) Magnification: 5000X (SEM)

Figure 9. The second microconstituent at a) 2500X and b) 5000X observed with SEM in the hot band Nb-bearing steel samples show a typical pearlite microstructure

Different techniques confirmed that the Nb-bearing steel at hot band state had a smaller grain size and larger volume fraction of pearlite than Ti-bearing steel, it’s believed that these microstructure differences was one of the reasons causing different stored energy level at the initial hot band and cold rolled states, this will be discussed further later.

Figure 10 shows a typical structure evolution for the annealing process of cold rolled steels. From Figure 11, we can see that the hardness (VHN) of cold rolled samples drops continuously during annealing process, the sharp drop around 600°C indicates that the recrystallization starts around that temperature, EBSD analysis also confirmed the start temperature of recrystallization is around 580°C to 600°C as shown in Figure 12, the temperatures were different for different alloy composition steels, Nb-bearing steel started to recrystallize at lower temperature around 580°C other than Ti-bearing steel starting around 600°C. The fraction of low angle misorientation (<15°) continuously decreases and the fraction of high angle misorientation (>15°) continuously increases during annealing (Figure 13), which shows that stored energy is consumed continuously during the recovery and recrystallization stages.

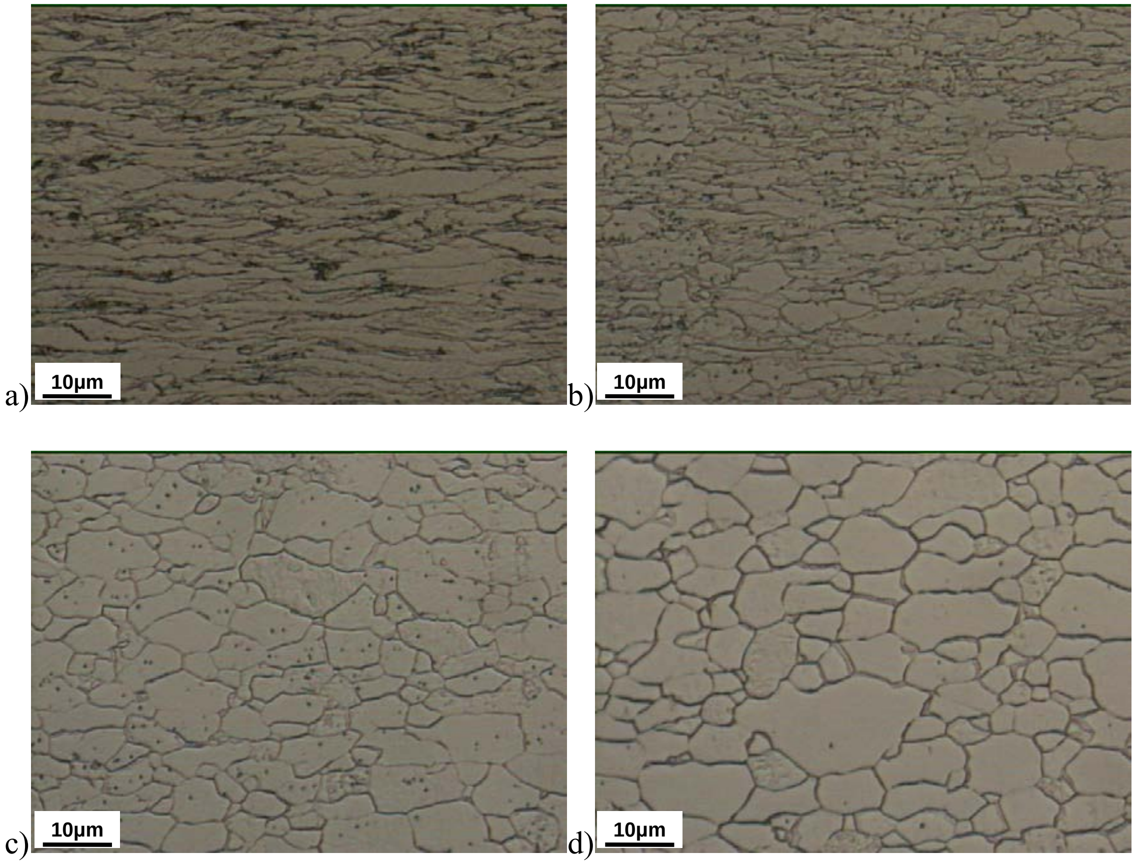

Figure 10. OM images showing the structure evolution of the annealing process of Nb-bearing steel: a) Cold Rolled, b) 600°C, c) 670°C, d) 670°C for 6hrs

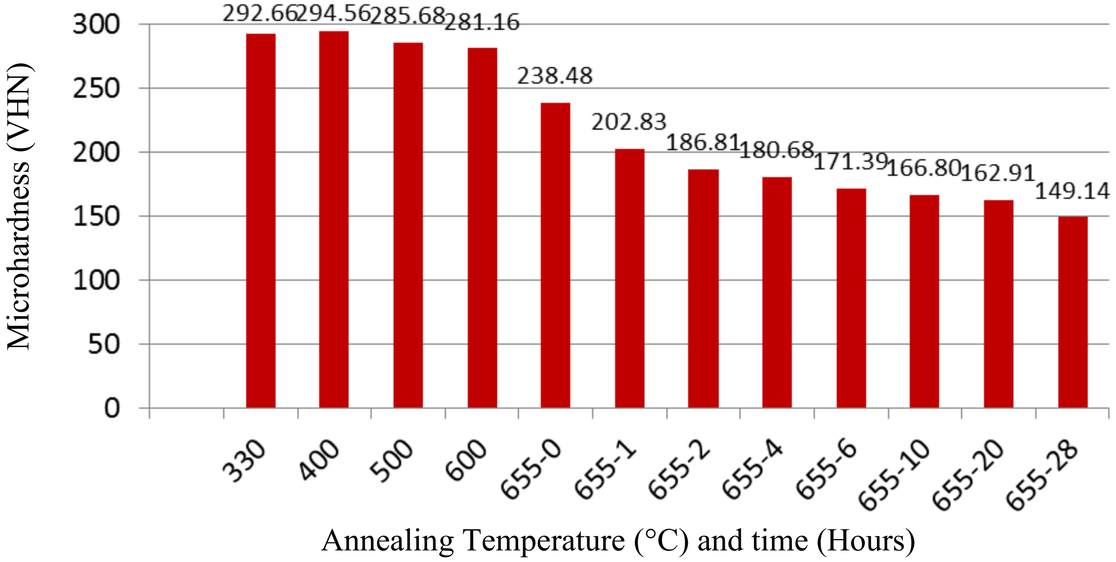

Figure 11. Microhardness (VHN) changing trend during annealing process of Ti-bearing steel

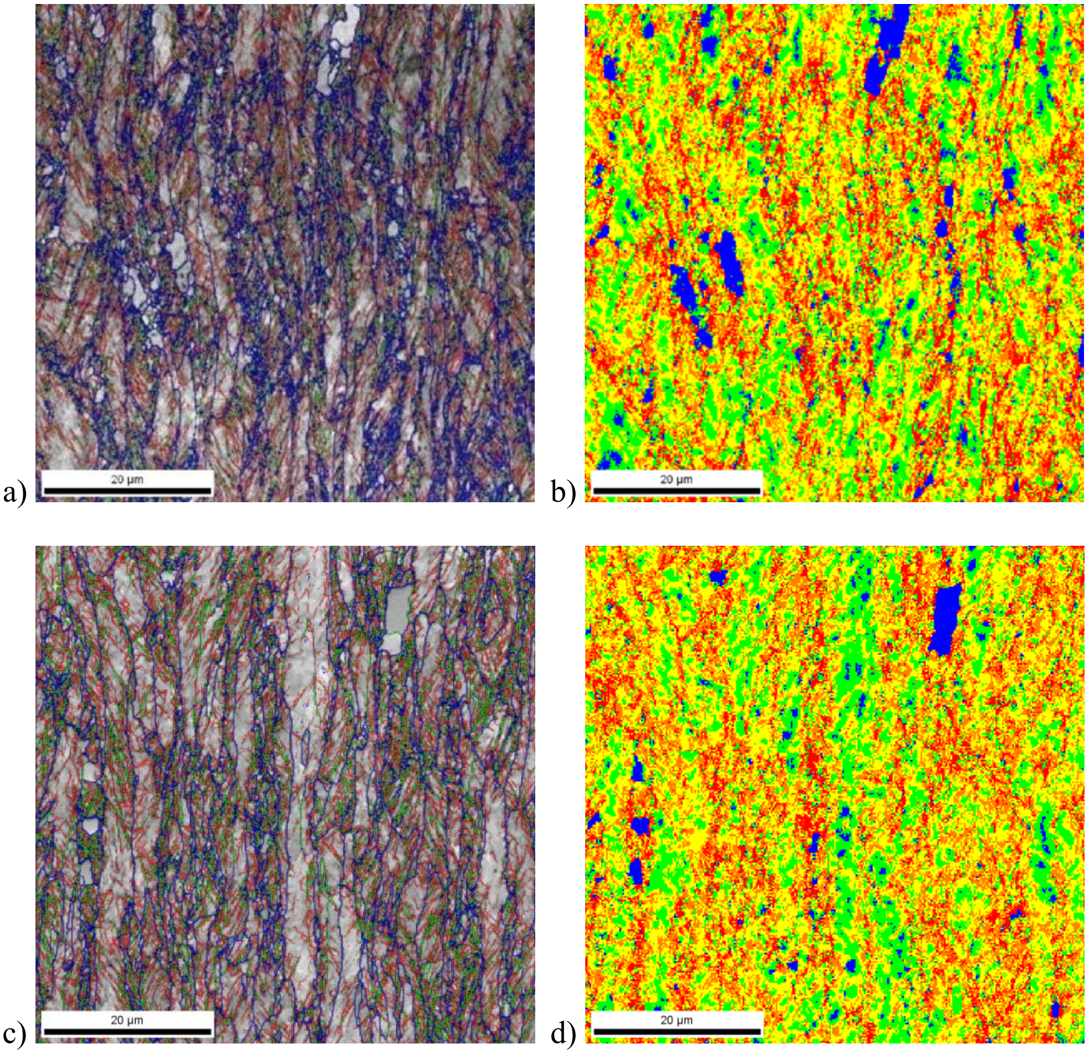

Figure 12. a) EBSD IQ reconstructed images and b) Kernel Average Misorientation distribution maps of Ti-bearing steel at annealing temperature reaching 600°C, and c) EBSD IQ reconstructed images and d) Kernel Average Misorientation distribution maps of Nb-bearing steel at annealing temperature reaching 580°C

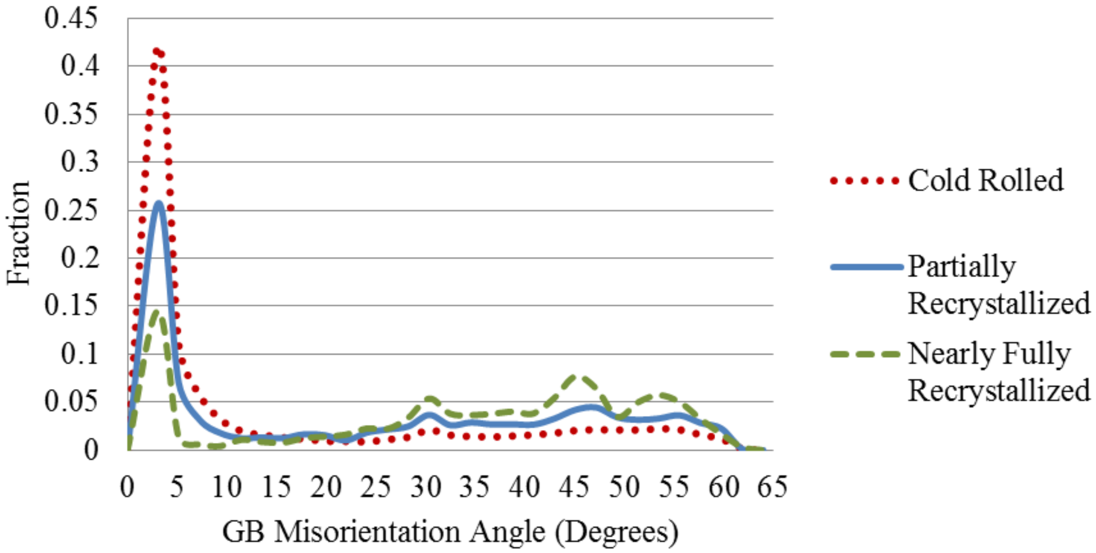

Figure 13. EBSD misorientation angle ditribution to quantify stored energy and recrystallization for Nb-bearing steel

Stored energy supplied the initial driving force for recovery and recrystallization. It was continuously consumed during the whole annealing process. The microhardness of the cold rolled steels kept dropping during annealing because the dislocation density, i.e., stored energy kept decreasing.

From the dashed line in Figure 14 and Figure 15, we can see that cold rolled sample surfaces are more deformed and have higher hardness than sample centers. Comparing Figure 15a and 15b, also comparing the dotted line and dashed line in Figure 14, we know that the difference between surfaces and centers will decrease as cold rolling reduction rate increases. More deformation means more stored energy. Stored energy supplies the initial driving force for recovery and recrystallization. So more stored energy makes the surfaces recrystallization easier and earlier than the centers as shown from the SEM images in Figure 17. The dramatic change of hardness across the sample was observed as shown in Figure 16.

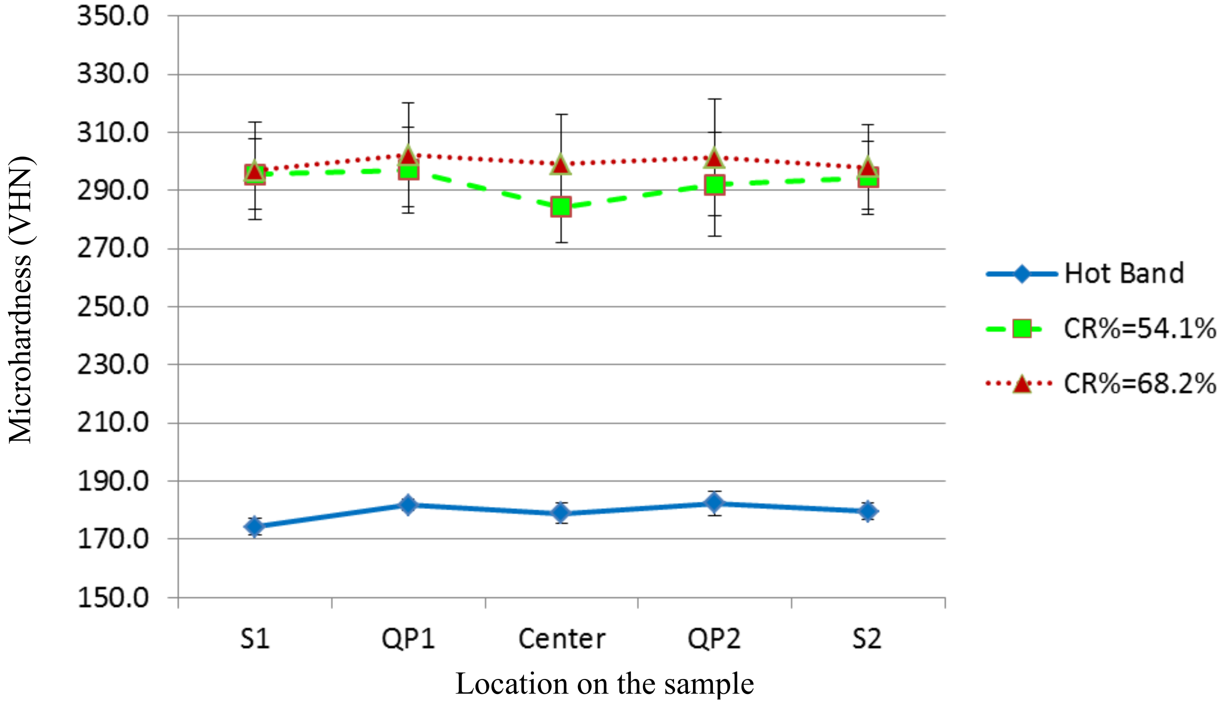

Figure 14. Microhardness (VHN) changes through the locations on the Ti-bearing steels

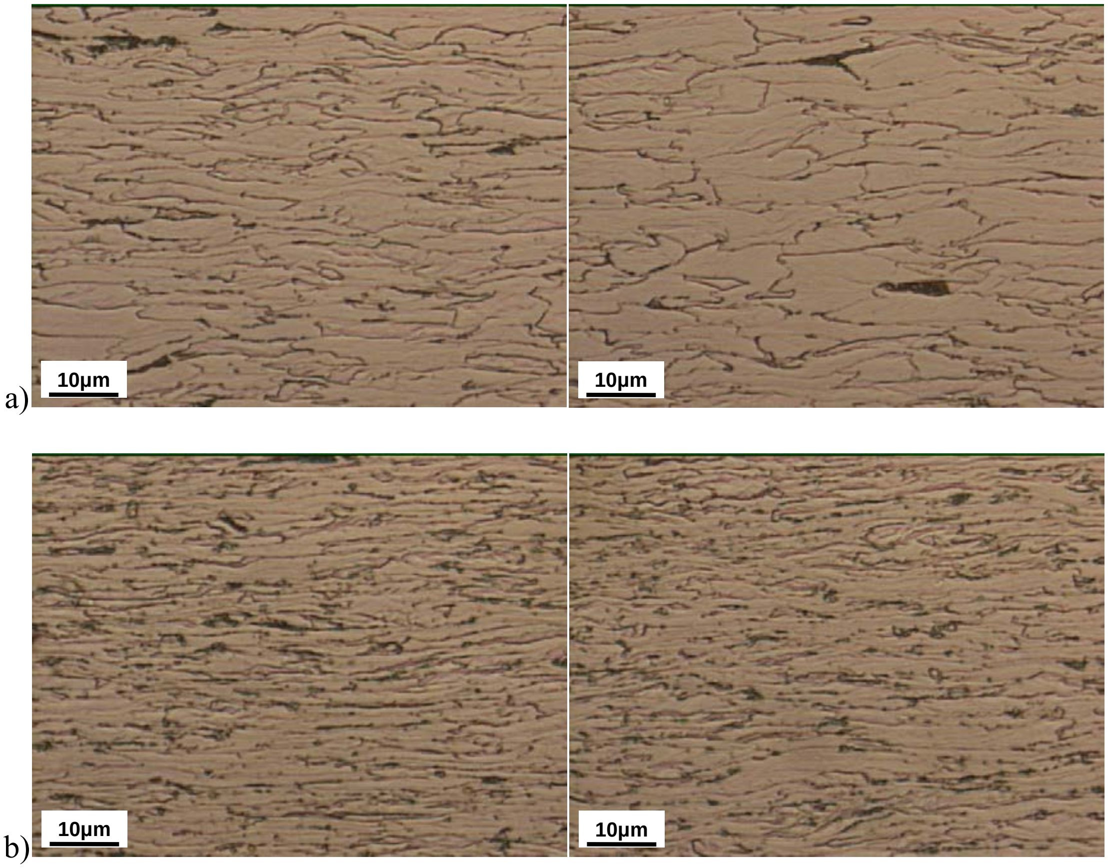

Figure 15. OM images show the difference between surface (left) and center (right) for a) CR%=54% for versus b) CR%=68% for Ti-bearing steel

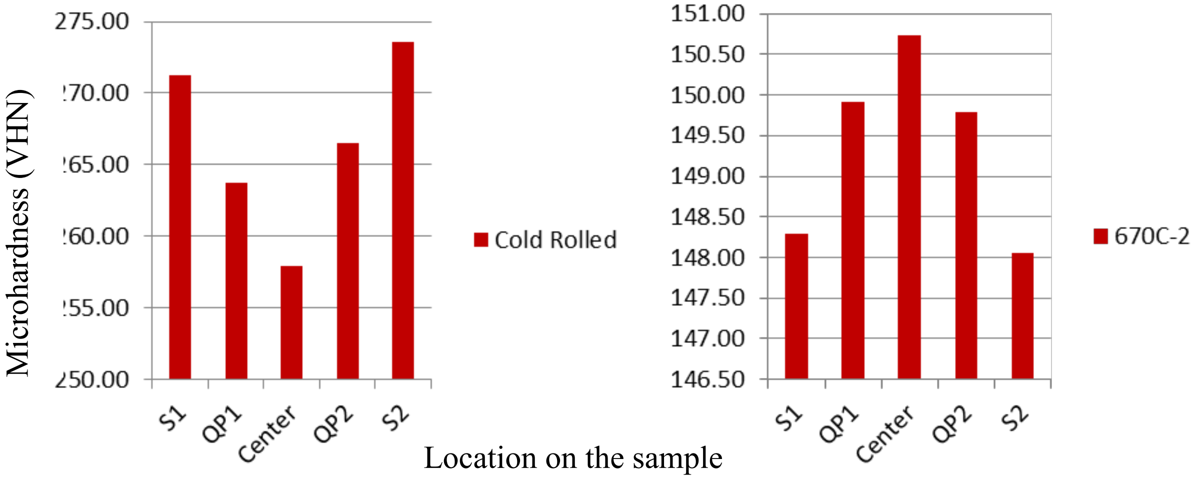

Figure 16. Comparison of microhardness varying across the sample before (left) and after (right) annealing for Nb-bearing steel

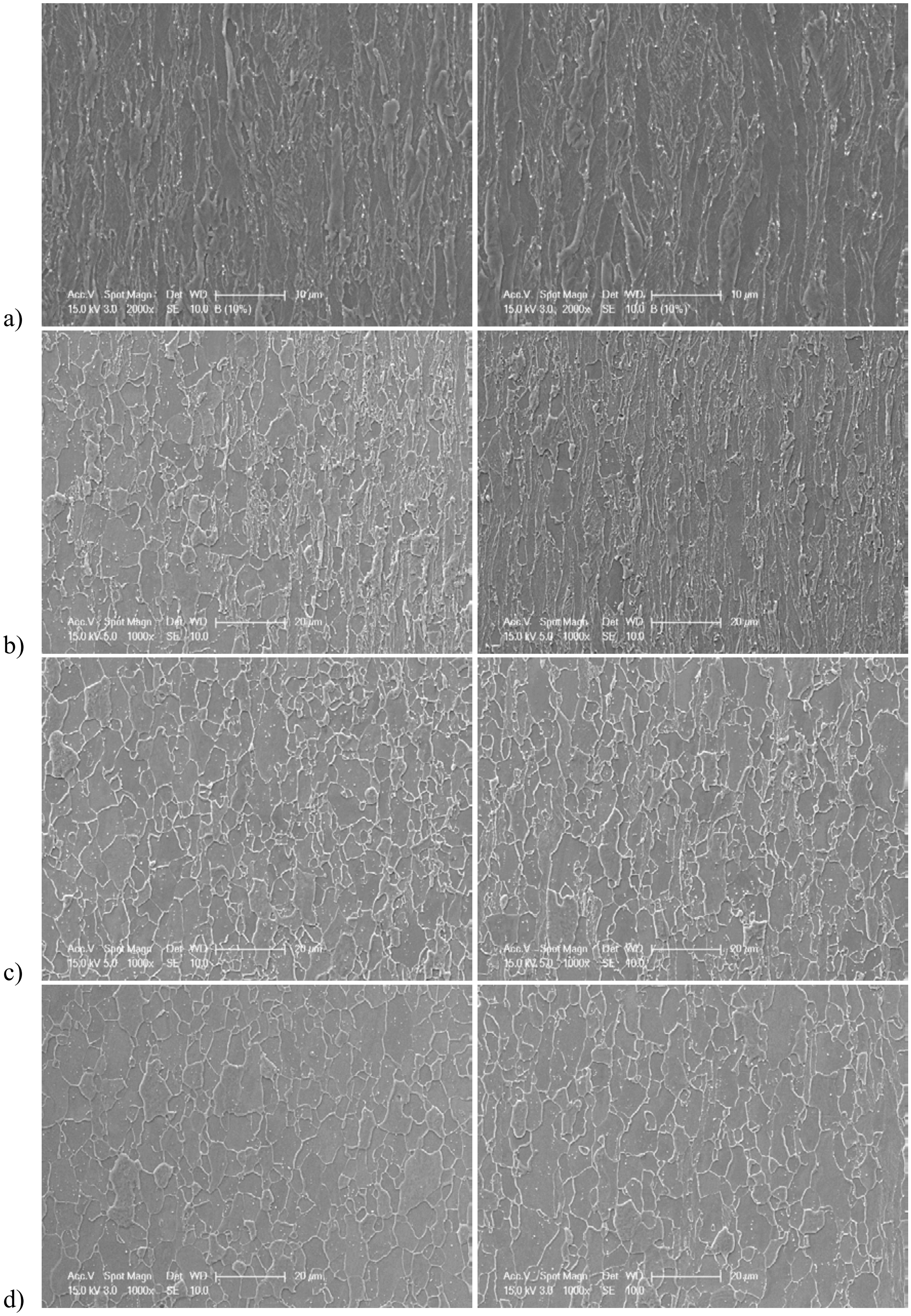
Acc.V Spot Magn Det WD 10 µm
15.0 kV 3.0 2000x SE 10.0 B (10%)
Acc.V Spot Magn Det WD 10 µm
15.0 kV 3.0 2000x SE 10.0 B (10%)
a)
Acc.V Spot Magn Det WD 20 µm
15.0 kV 5.0 1000x SE 10.0
Acc.V Spot Magn Det WD 20 µm
15.0 kV 5.0 1000x SE 10.0
b)
Acc.V Spot Magn Det WD 20 µm
15.0 kV 5.0 1000x SE 10.0
Acc.V Spot Magn Det WD 20 µm
15.0 kV 5.0 1000x SE 10.0
c)
Acc.V Spot Magn Det WD 20 µm
15.0 kV 3.0 1000x SE 10.0
Acc.V Spot Magn Det WD 20 µm
15.0 kV 3.0 1000x SE 10.0
d)

e)

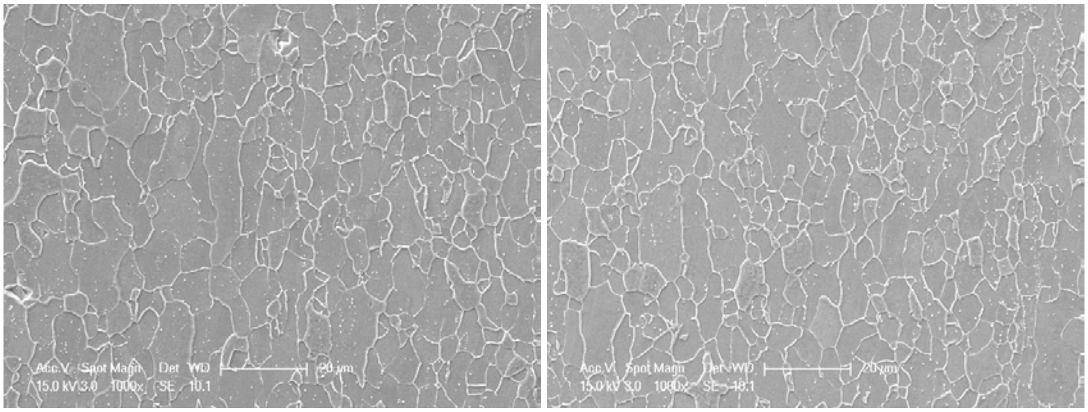

Figure 17. The comparison of surface (left) and center (right) annealing conditions at a) 580°C, b) 600°C, c) 620°C, d) 640°C, e) 660°C for Nb-bearing steel samples using SEM

To eliminate the influence of different soaking temperatures and make a better comparison, 670°C was commonly used as the highest heating temperature and soaking temperature for most samples. Recrystallization starts around 580°C to 600°C, but varied for different alloy composition steels. The Nb-bearing steel starts to recrystallize at a lower temperature (around 580°C) and a higher recrystallization rate than Ti-bearing steel (around 600°C) even though the cold rolling reduction rate (CR%) of Ti-bearing steel (58.2%) is a little higher than Nb-bearing steel (54.5%) The scanning was conducted at the center, quarter point, and surface layers of each sample (Figure 18-37). The fraction of recrystallization changing trends over time for both steels at different layers was compared in Figure 38. The average hardness changing trends for both steels were compared in Figure 39. All the differences could come from a lot of factors such as stored energy, texture, precipitation and grain boundary types, etc. Steels with different composition had different recrystallization kinetics. Nb-bearing steel had a lower recrystallization start temperature and faster recrystallization speed at the first stages. One of the reasons is that the stored energy in the cold rolled Nb-bearing steel was higher than Ti-bearing steel, which was inherited by the nature of the type of ferrite which could have a higher dislocation density (stored energy) in the hot band condition due to different microalloying compositions and processing parameters. The sample surface layers were deformed more and have more shear strain, thus contained much higher stored energy than the center layers, which make the surface layers had a faster recrystallization kinetics than the center layers. But Nb-bearing steel had a better uniformity throughout the sample thickness than Ti-bearing steel. For Ti-bearing steel, precipitates began to dramatically influence the recrystallization kinetics after annealing to 660ºC.

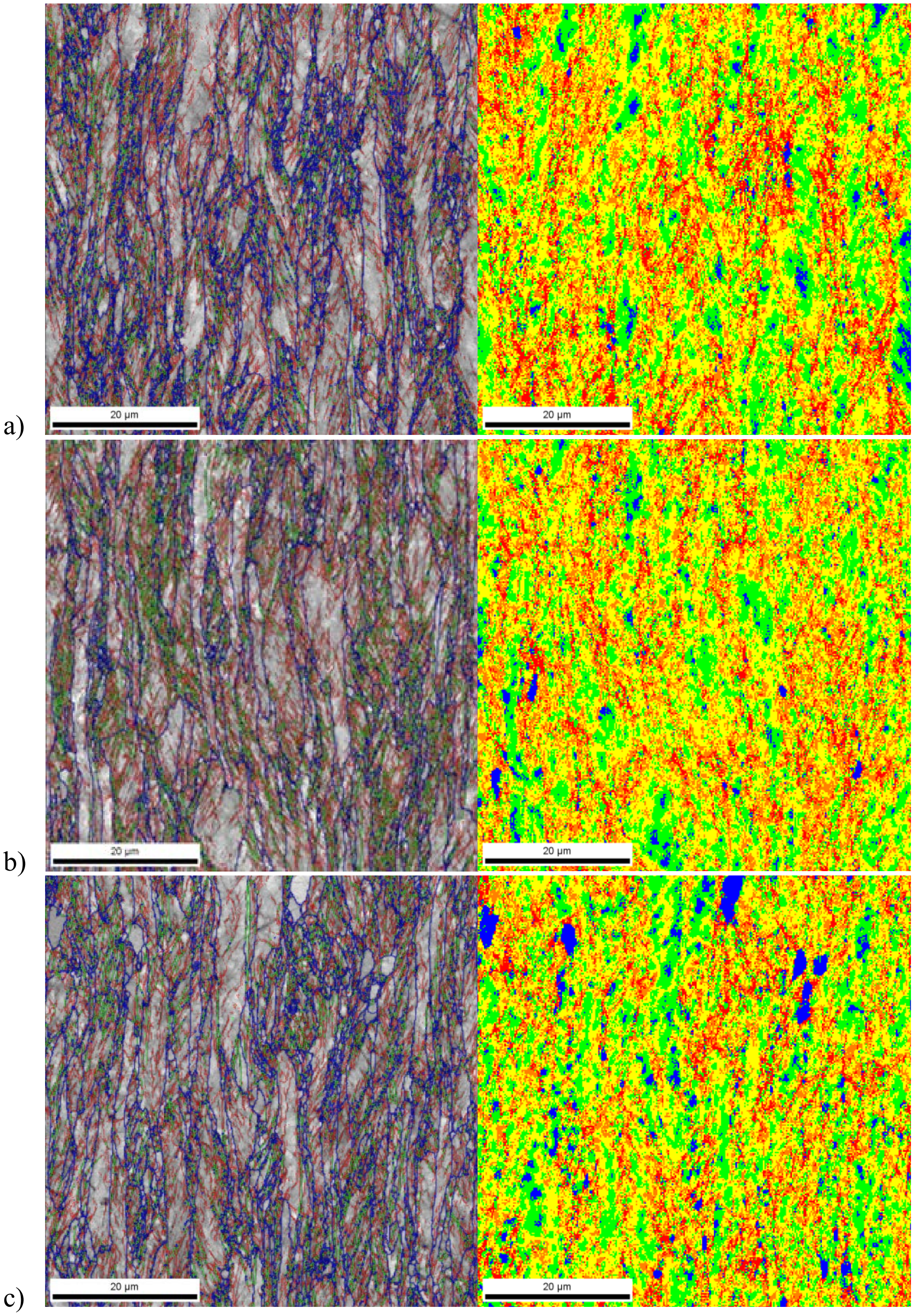

Figure 18. EBSD IQ reconstructed images (left) and Kernel Average Misorientation distribution maps (right) at a) center layer, b) quarter point layer, and c) surface layer of Ti-bearing steel at 580°C

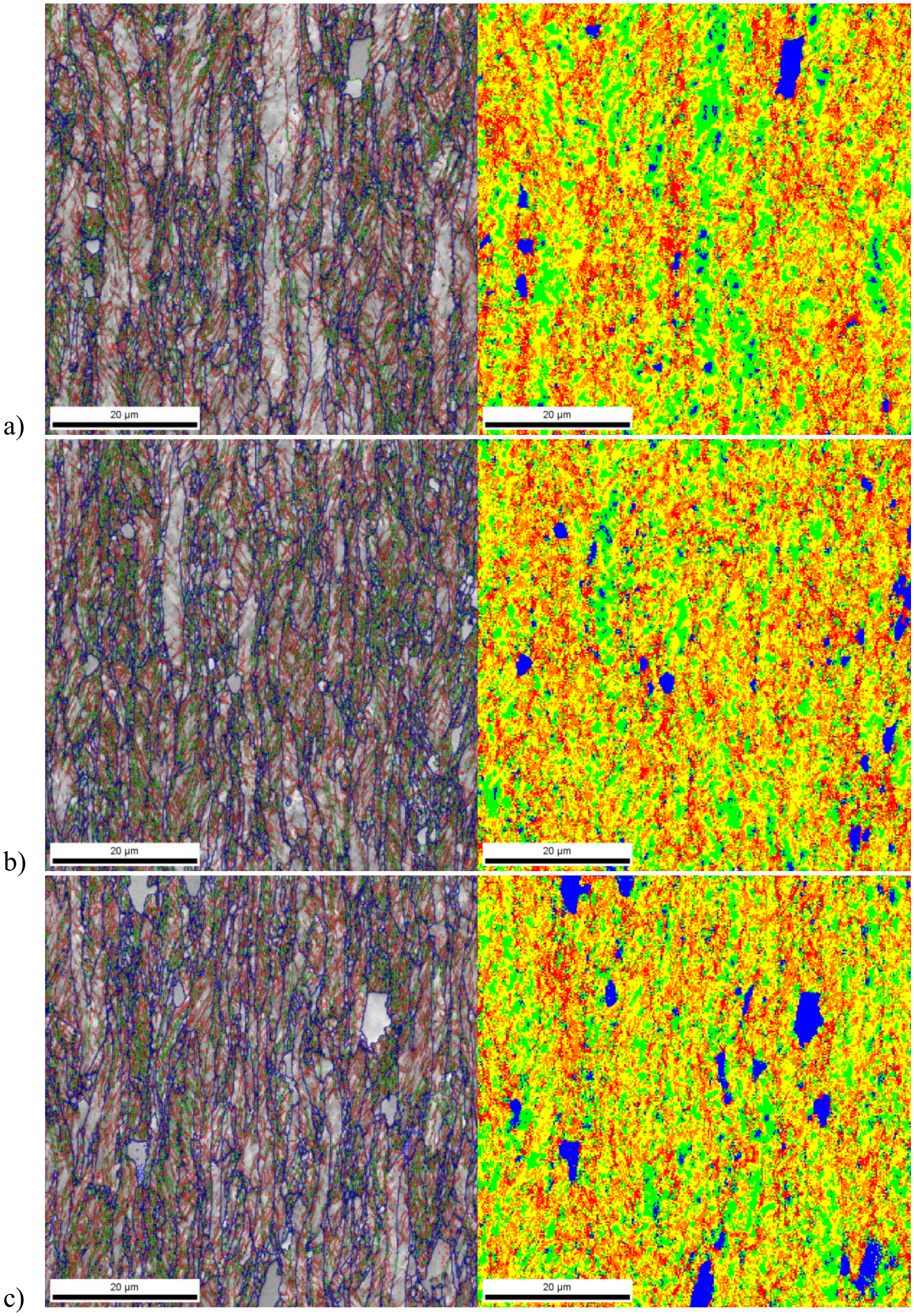

Figure 19. EBSD IQ reconstructed images (left) and Kernel Average Misorientation distribution maps (right) at a) center layer, b) quarter point layer, and c) surface layer of Nb-bearing steel at 580°C

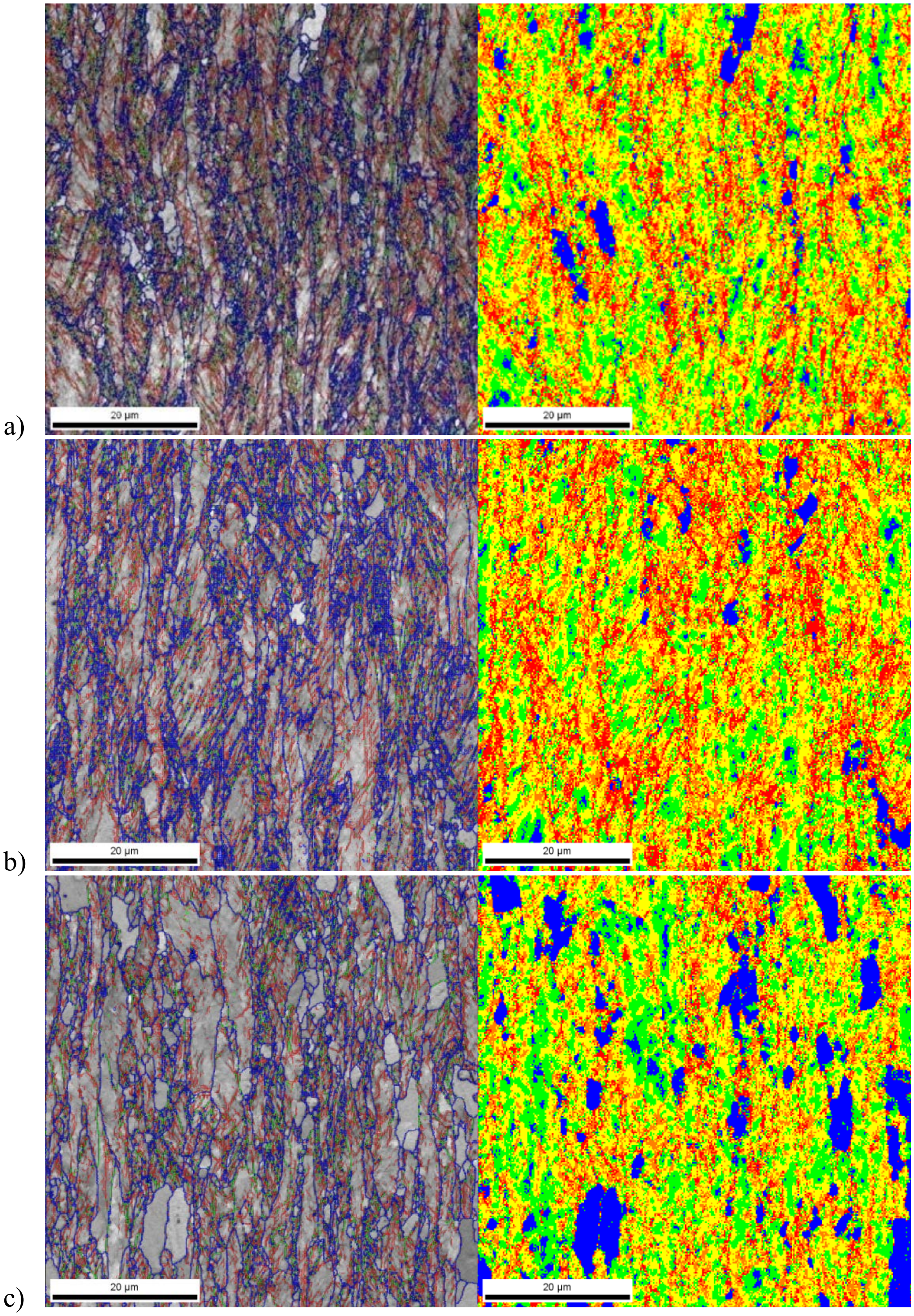

Figure 20. EBSD IQ reconstructed images (left) and Kernel Average Misorientation distribution maps (right) at a) center layer, b) quarter point layer, and c) surface layer of Ti-bearing steel at 600°C

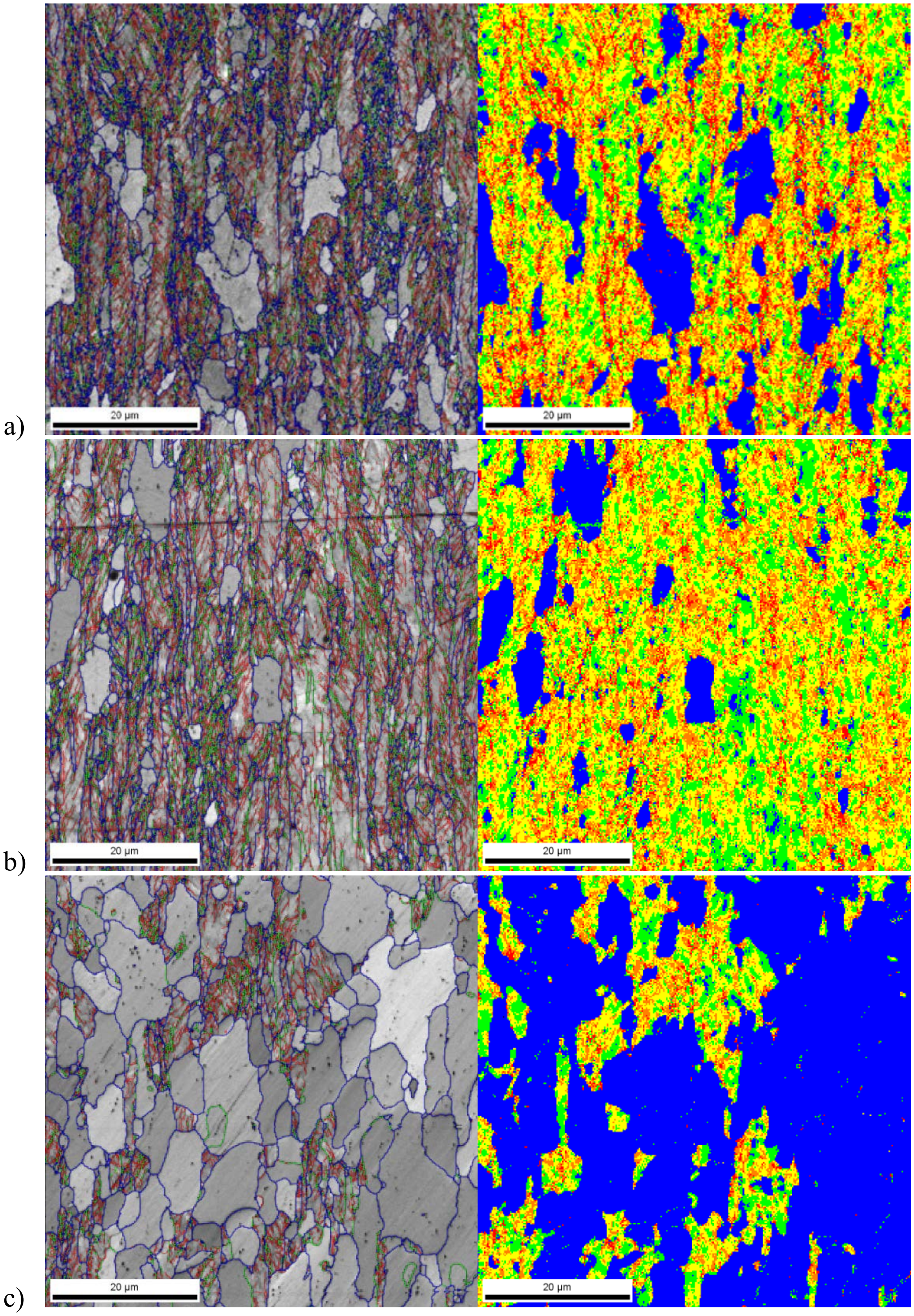

Figure 21. EBSD IQ reconstructed images (left) and Kernel Average Misorientation distribution maps (right) at a) center layer, b) quarter point layer, and c) surface layer of Nb-bearing steel at 600°C

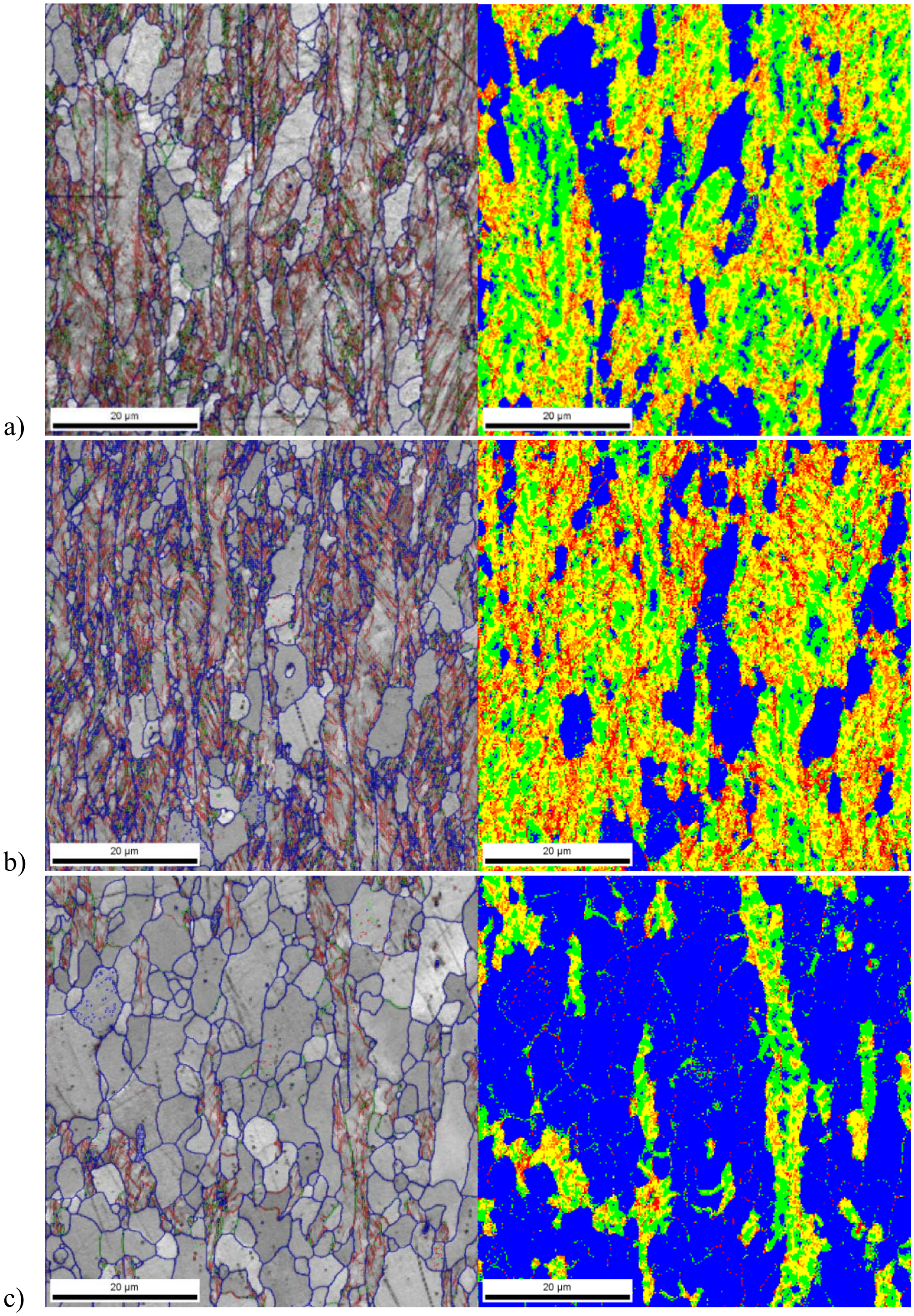

Figure 22. EBSD IQ reconstructed images (left) and Kernel Average Misorientation distribution maps (right) at a) center layer, b) quarter point layer, and c) surface layer of Ti-bearing steel at 620°C

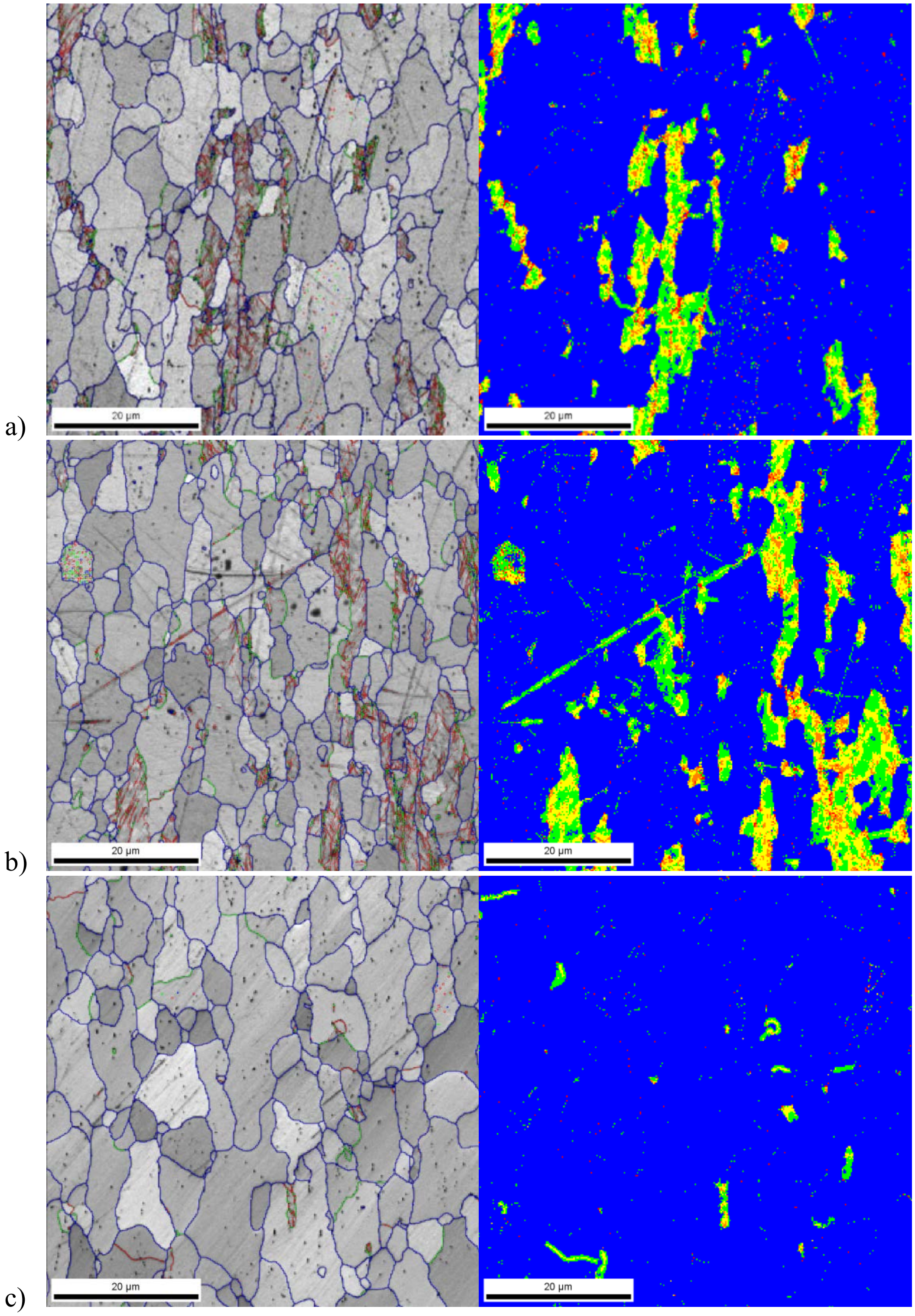

Figure 23. EBSD IQ reconstructed images (left) and Kernel Average Misorientation distribution maps (right) at a) center layer, b) quarter point layer, and c) surface layer of Nb-bearing steel at 620°C

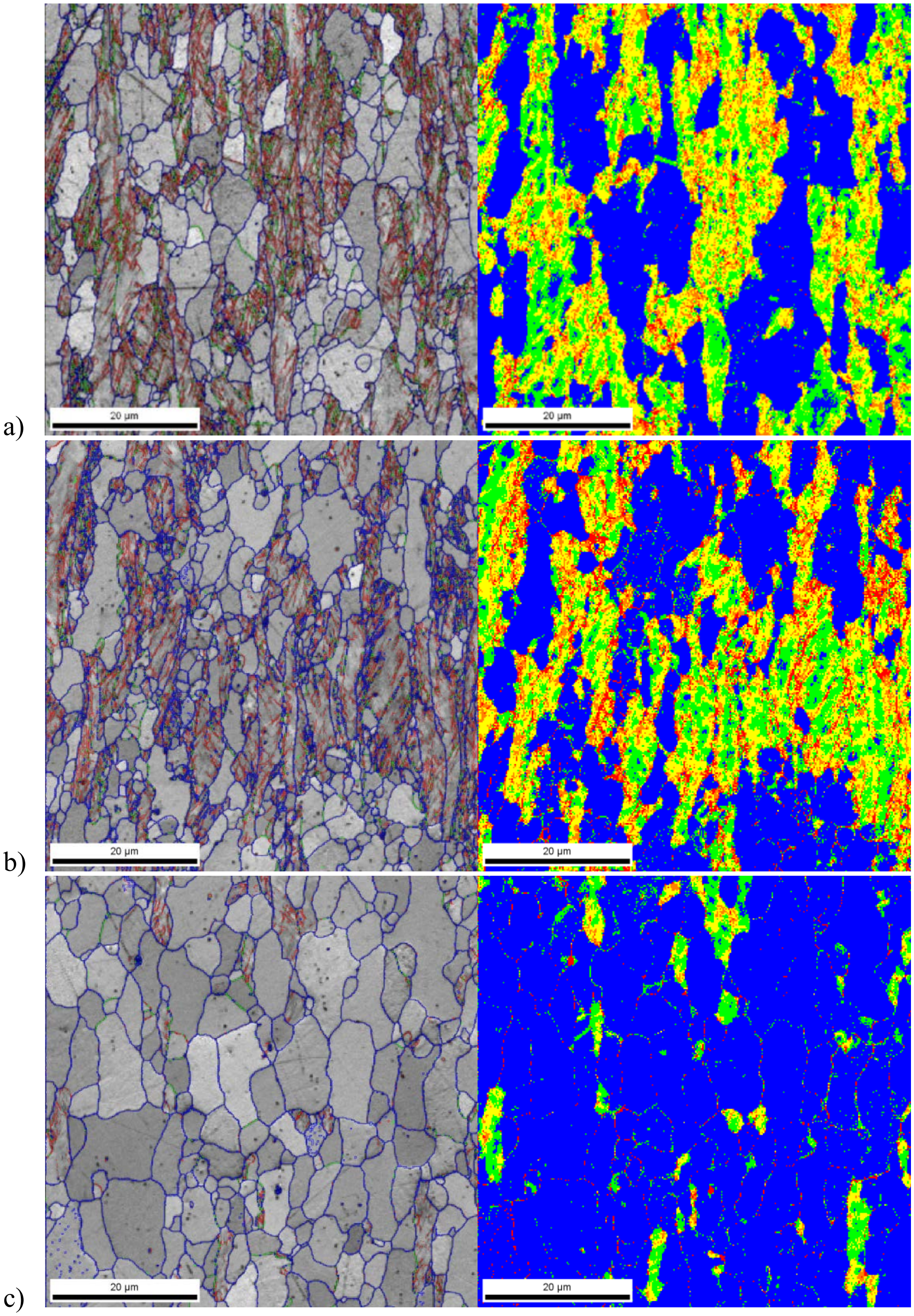

Figure 24. EBSD IQ reconstructed images (left) and Kernel Average Misorientation distribution maps (right) at a) center layer, b) quarter point layer, and c) surface layer of Ti-bearing steel at 640°C

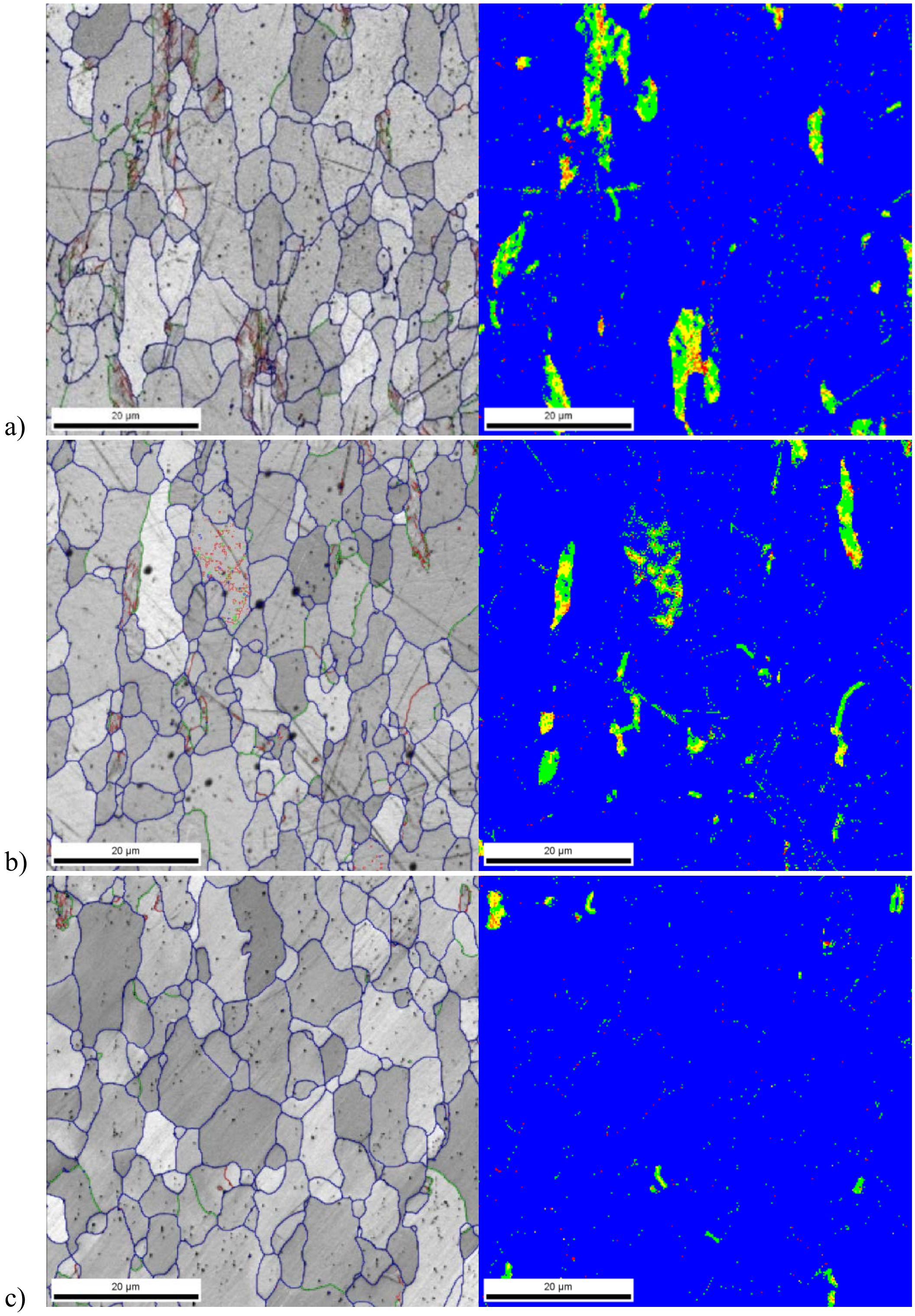

Figure 25. EBSD IQ reconstructed images (left) and Kernel Average Misorientation distribution maps (right) at a) center layer, b) quarter point layer, and c) surface layer of Nb-bearing steel at 640°C

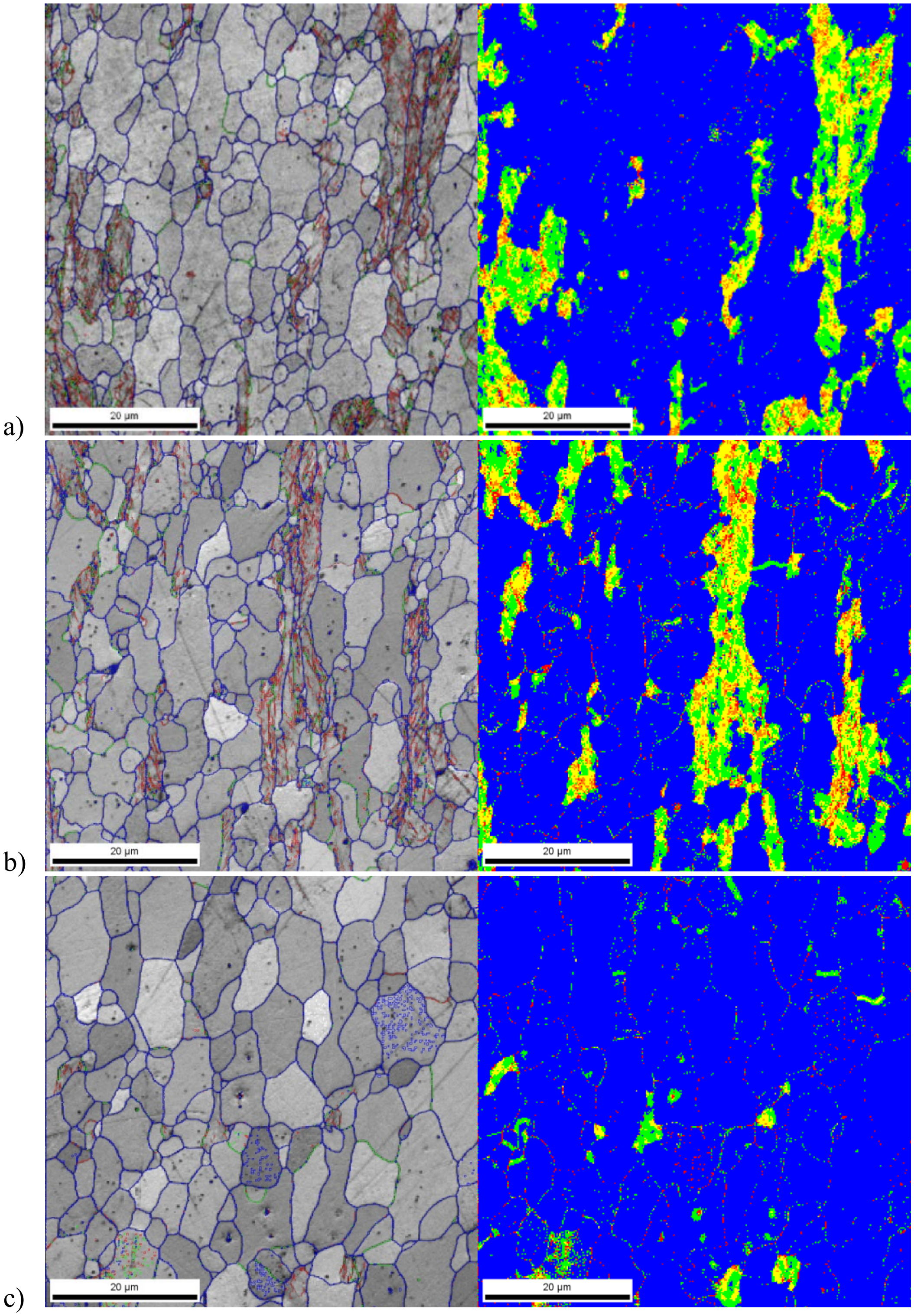

Figure 26. EBSD IQ reconstructed images (left) and Kernel Average Misorientation distribution maps (right) at a) center layer, b) quarter point layer, and c) surface layer of Ti-bearing steel at 660°C

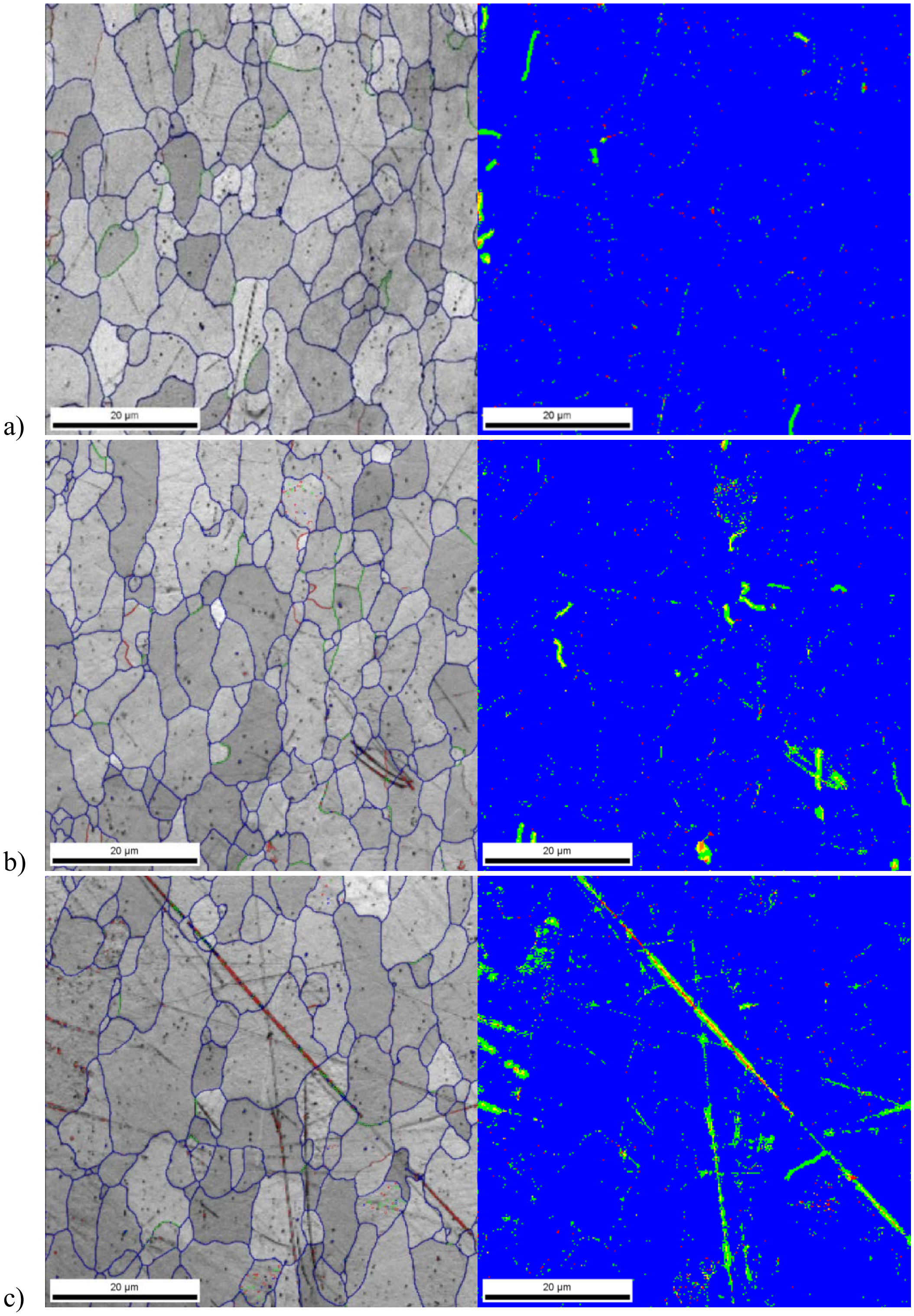

Figure 27. EBSD IQ reconstructed images (left) and Kernel Average Misorientation distribution maps (right) at a) center layer, b) quarter point layer, and c) surface layer of Nb-bearing steel at 660°C

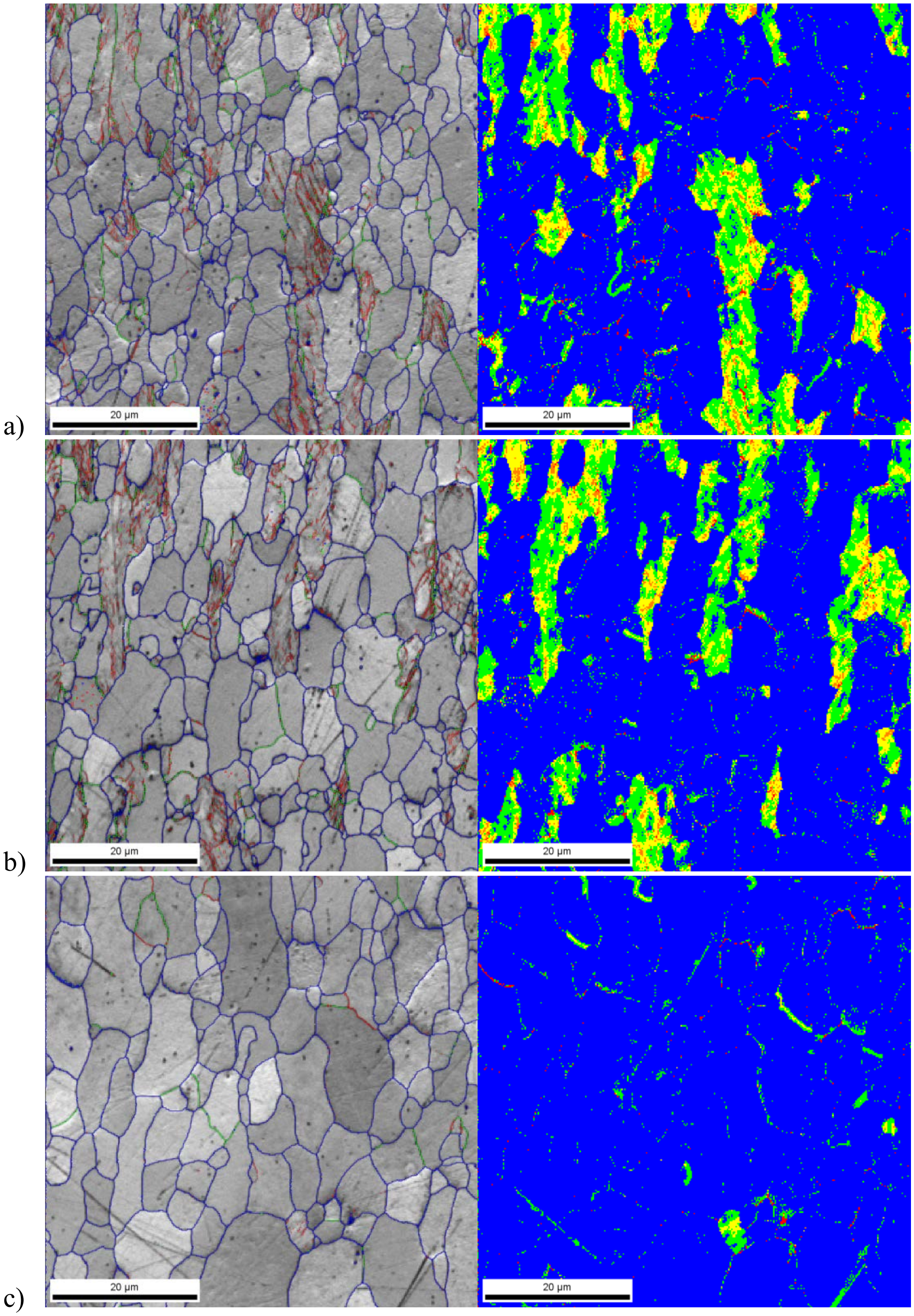

Figure 28. EBSD IQ reconstructed images (left) and Kernel Average Misorientation distribution maps (right) at a) center layer, b) quarter point layer, and c) surface layer of Ti-bearing steel at 670°C

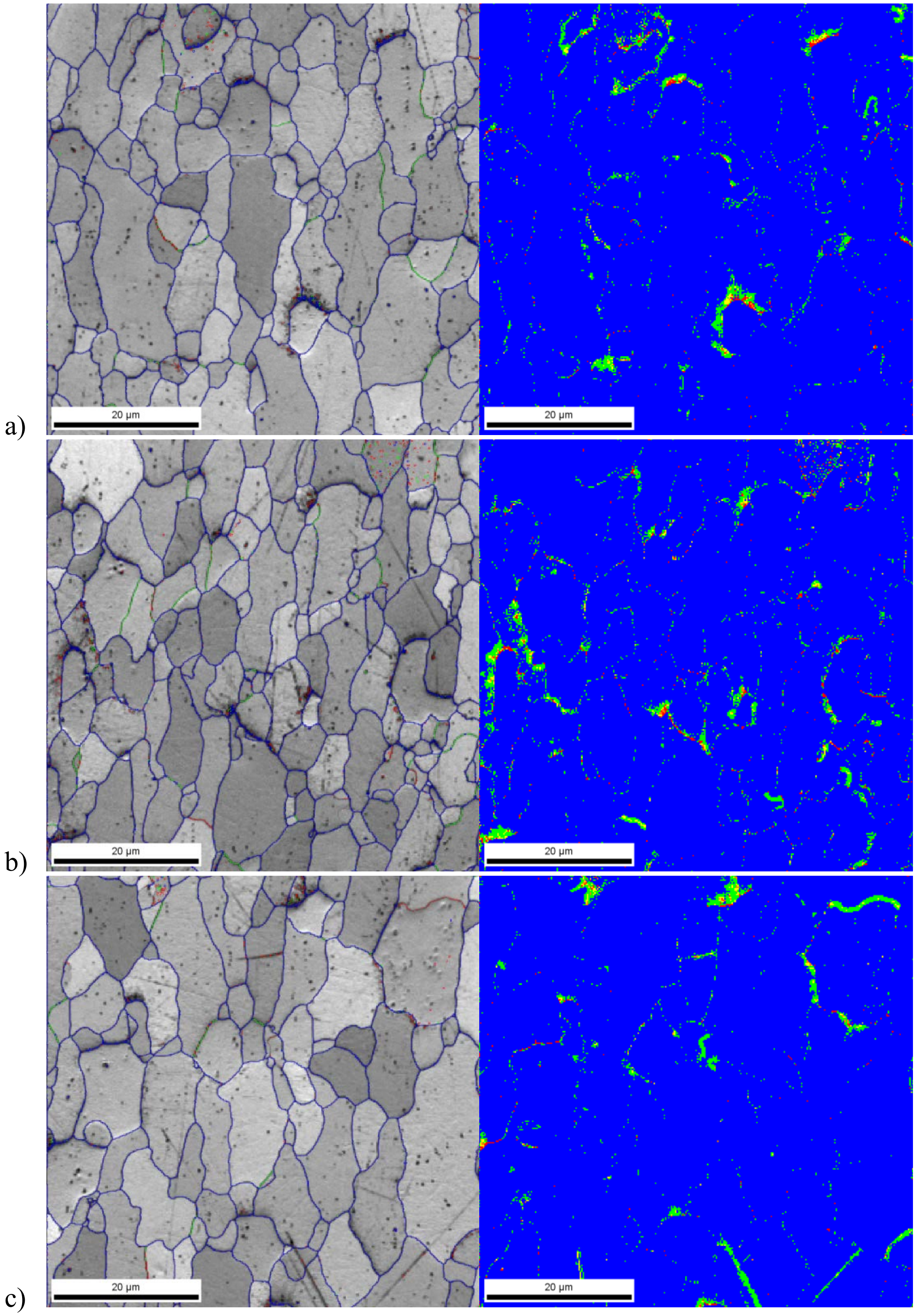

Figure 29. EBSD IQ reconstructed images (left) and Kernel Average Misorientation distribution maps (right) at a) center layer, b) quarter point layer, and c) surface layer of Nb-bearing steel at 670°C

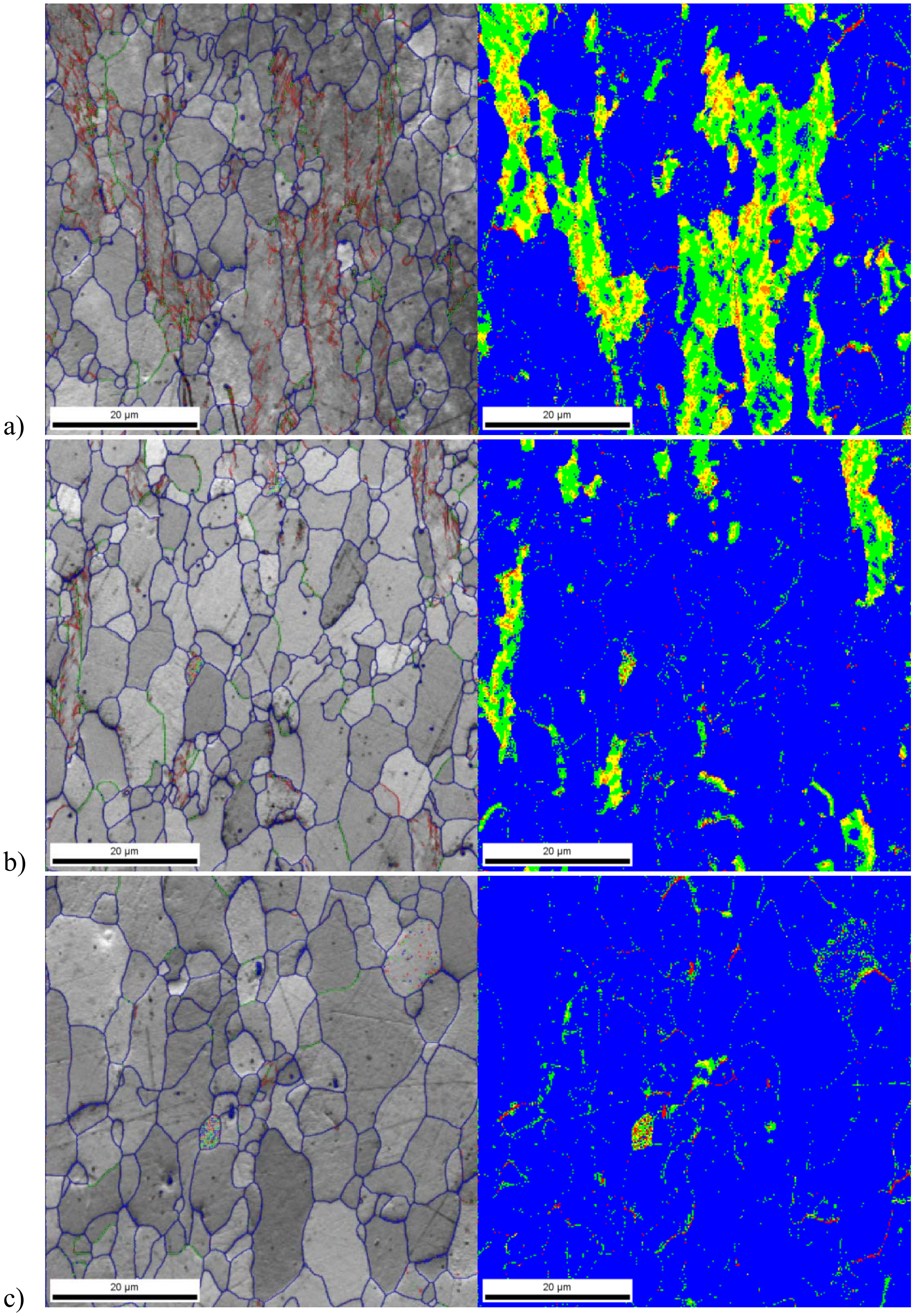

Figure 30. EBSD IQ reconstructed images (left) and Kernel Average Misorientation distribution maps (right) at a) center layer, b) quarter point layer, and c) surface layer of Ti-bearing steel at 670°C soaking for 1 hour

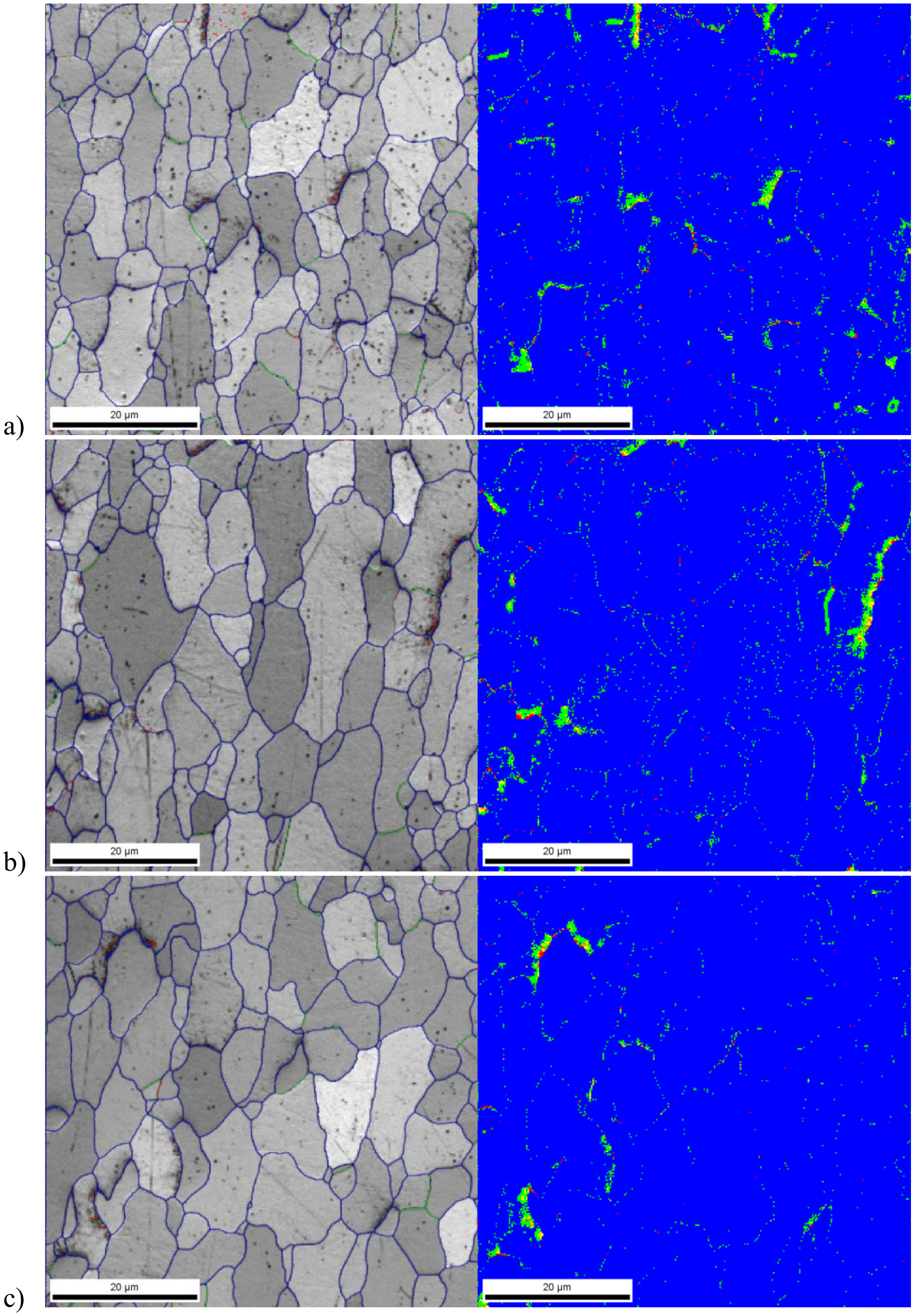

Figure 31. EBSD IQ reconstructed images (left) and Kernel Average Misorientation distribution maps (right) at a) center layer, b) quarter point layer, and c) surface layer of Nb-bearing steel at 670°C soaking for 1 hour

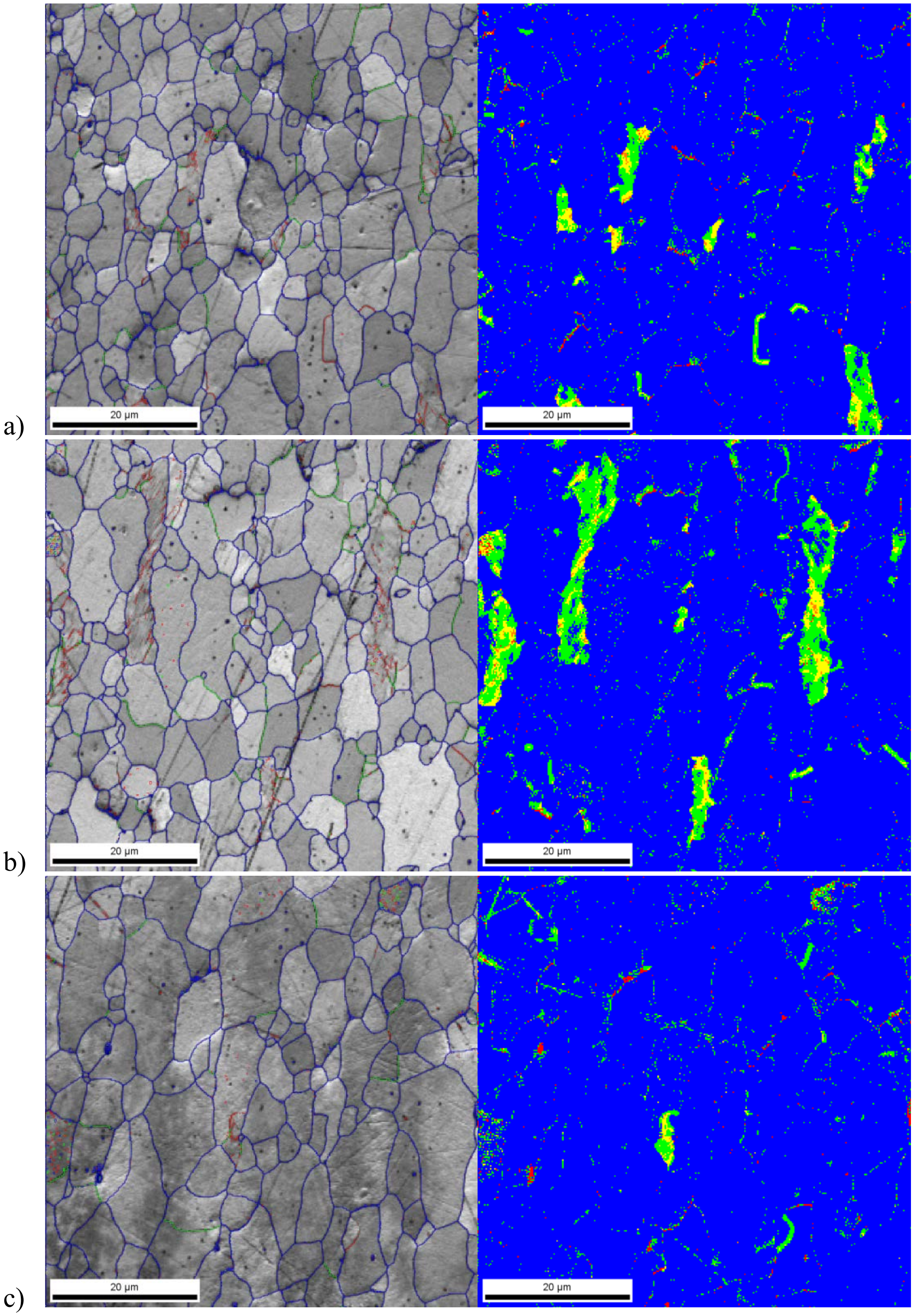

Figure 32. EBSD IQ reconstructed images (left) and Kernel Average Misorientation distribution maps (right) at a) center layer, b) quarter point layer, and c) surface layer of Ti-bearing steel at 670°C soaking for 2 hours

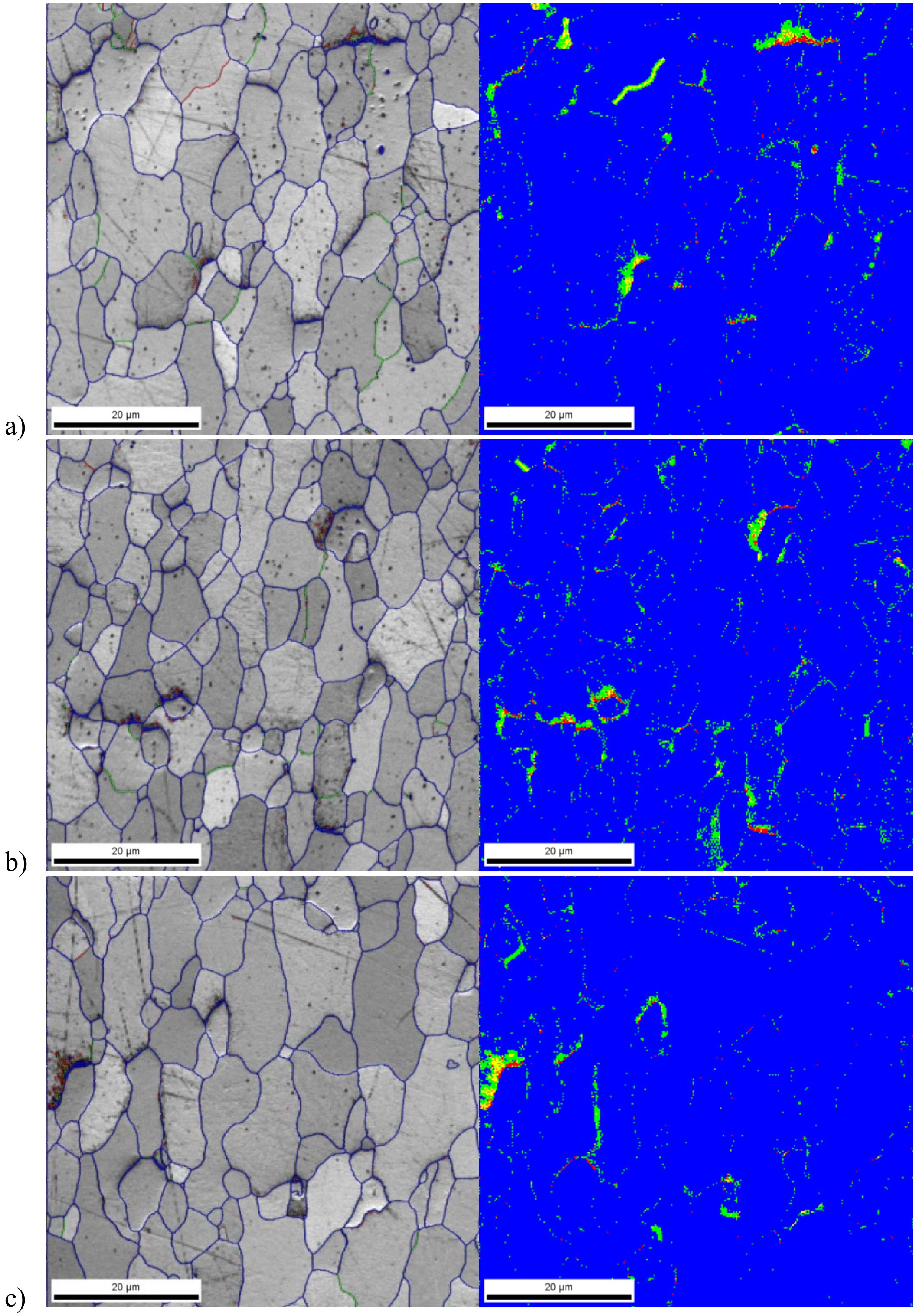

Figure 33. EBSD IQ reconstructed images (left) and Kernel Average Misorientation distribution maps (right) at a) center layer, b) quarter point layer, and c) surface layer of Nb-bearing steel at 670°C soaking for 2 hours

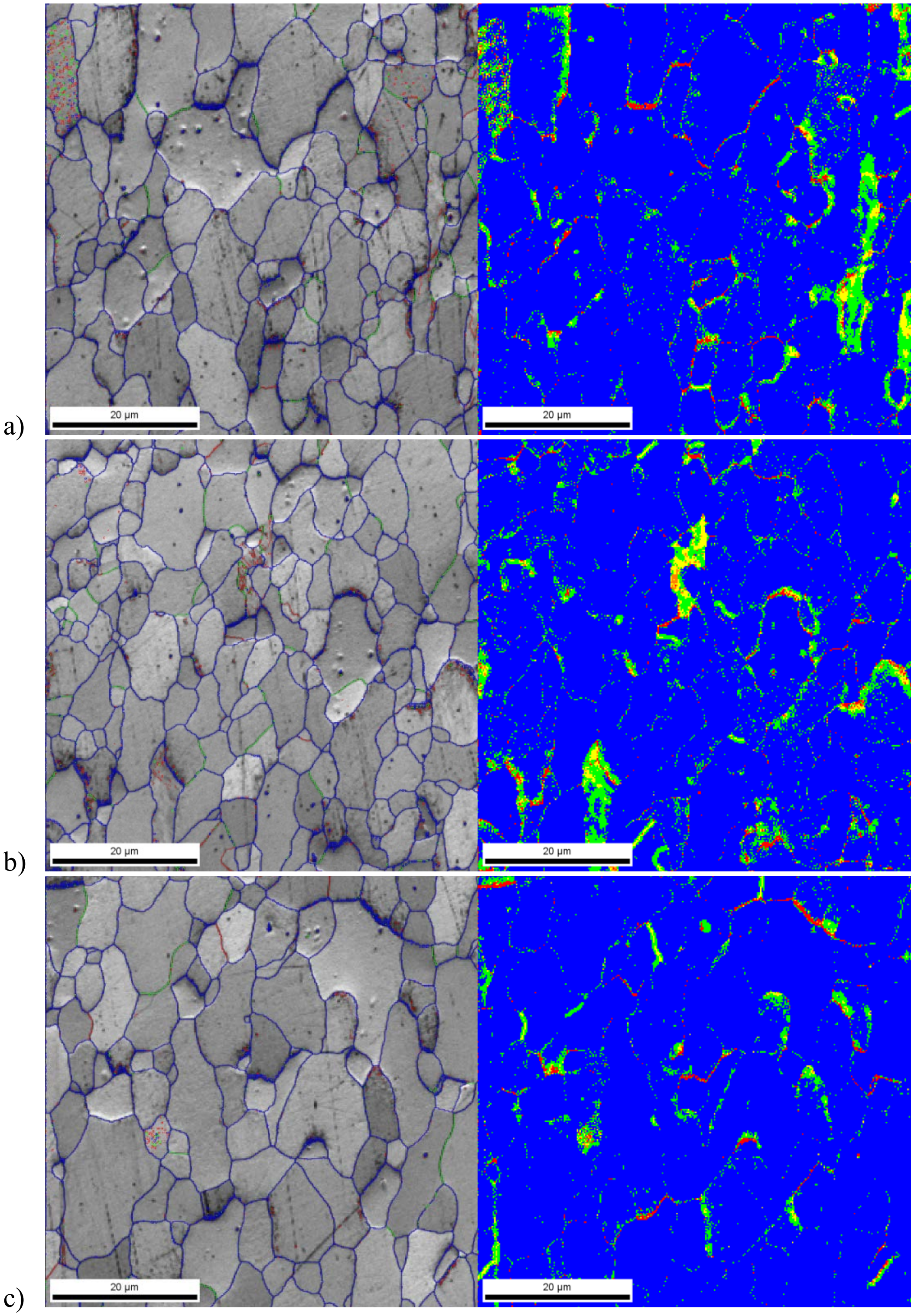

Figure 34. EBSD IQ reconstructed images (left) and Kernel Average Misorientation distribution maps (right) at a) center layer, b) quarter point layer, and c) surface layer of Ti-bearing steel at 670°C soaking for 4 hours

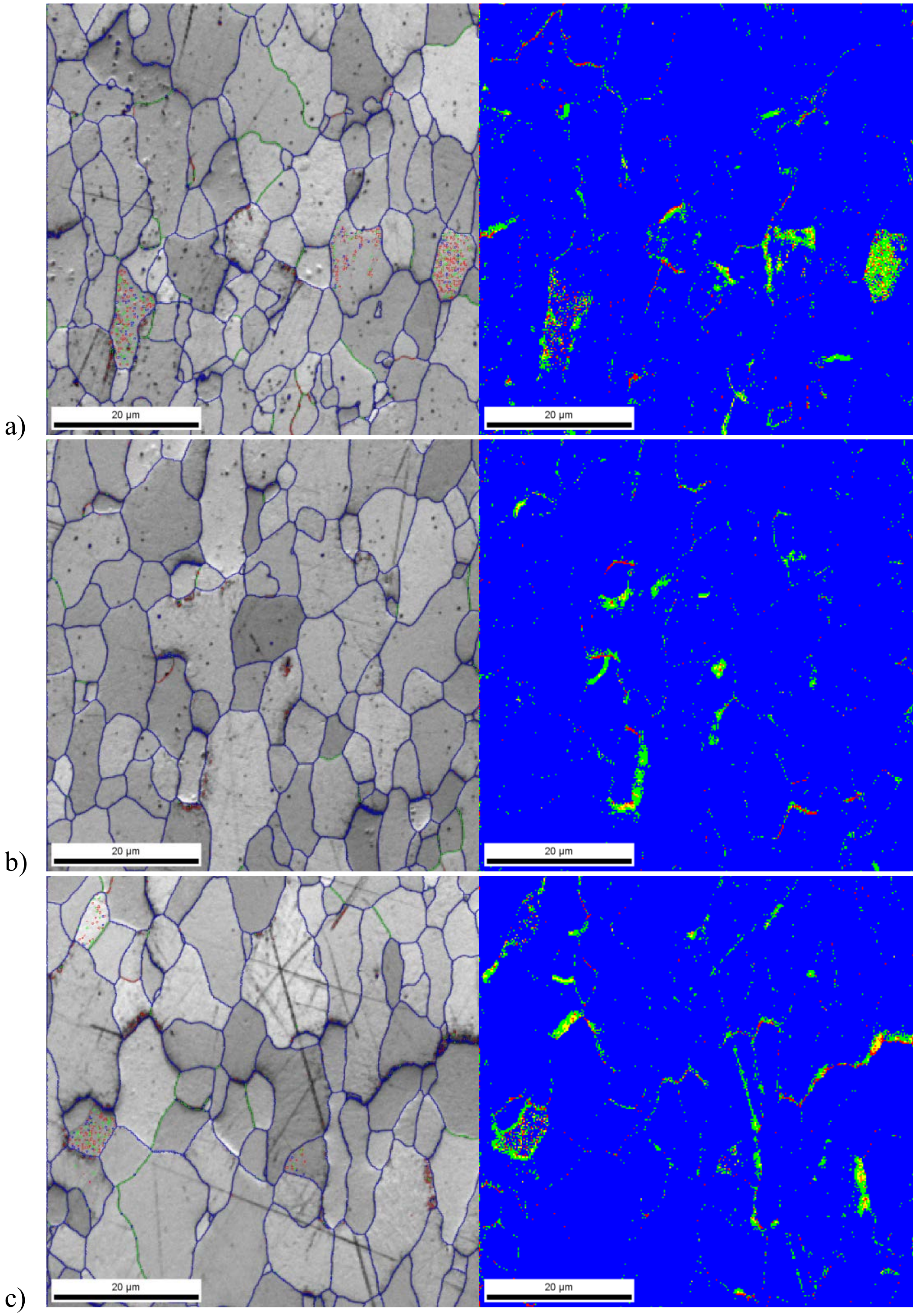

Figure 35. EBSD IQ reconstructed images (left) and Kernel Average Misorientation distribution maps (right) at a) center layer, b) quarter point layer, and c) surface layer of Nb-bearing steel at 670°C soaking for 4 hours

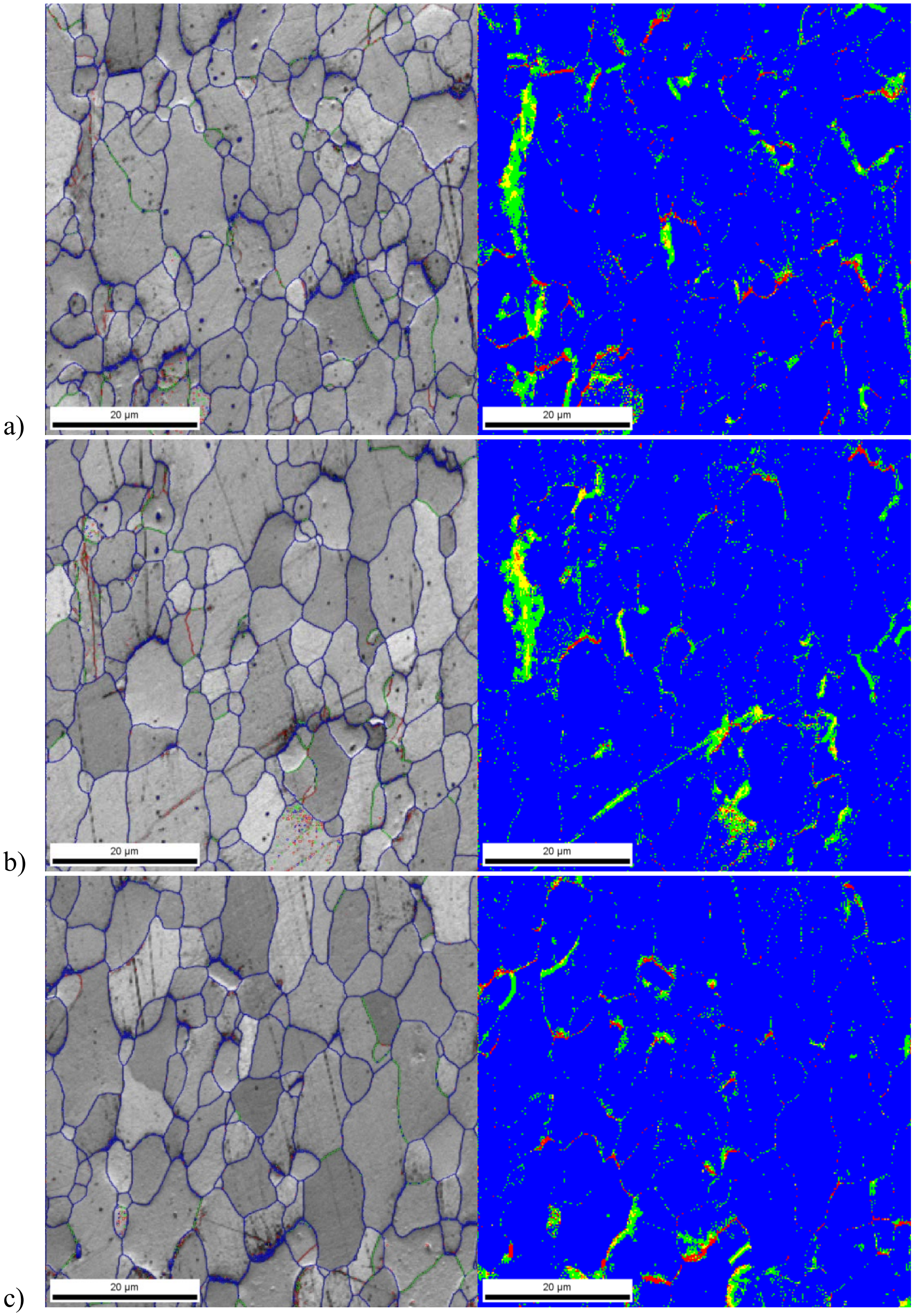

Figure 36. EBSD IQ reconstructed images (left) and Kernel Average Misorientation distribution maps (right) at a) center layer, b) quarter point layer, and c) surface layer of Ti-bearing steel at 670°C soaking for 6 hours

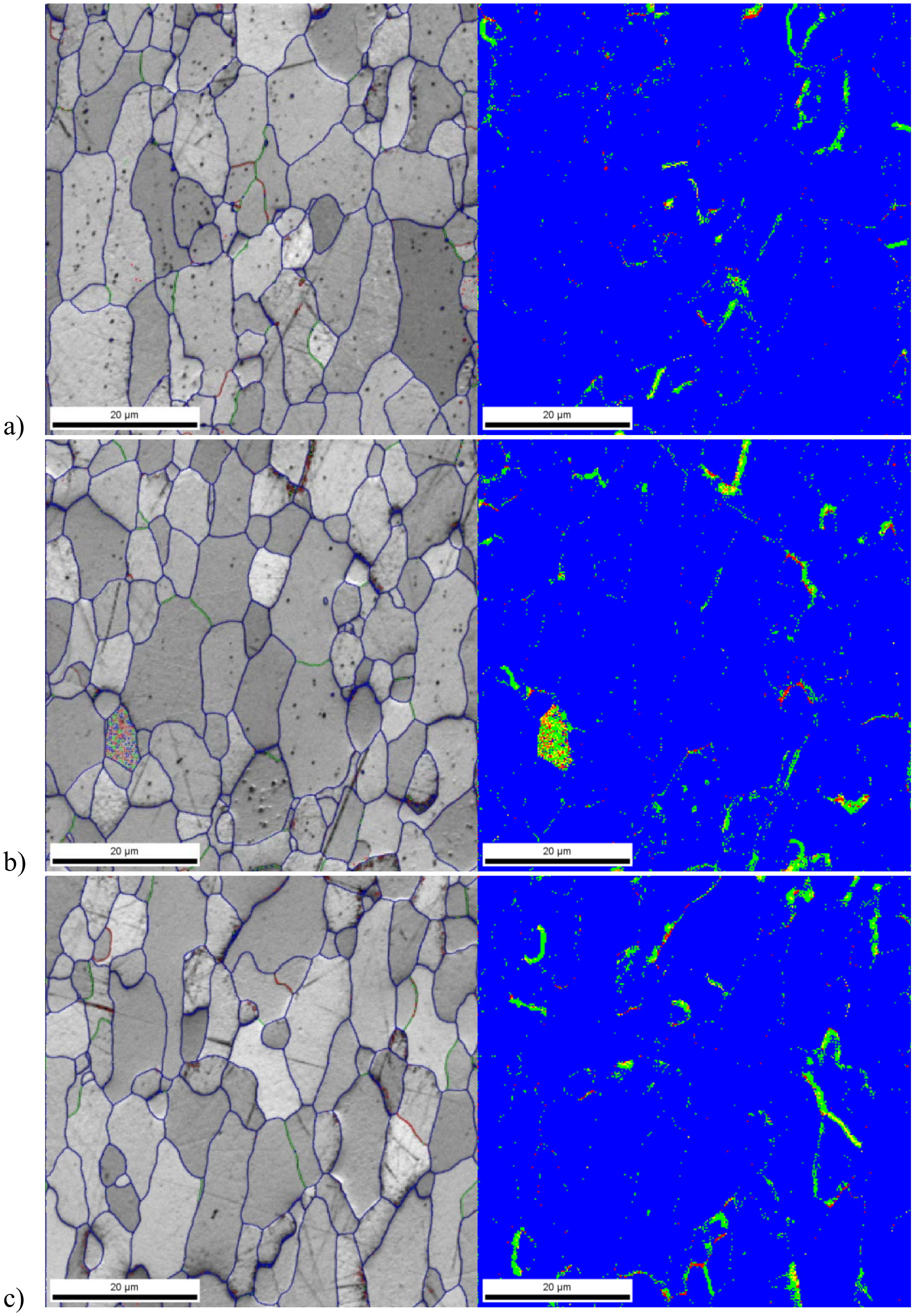

Figure 37. EBSD IQ reconstructed images (left) and Kernel Average Misorientation distribution maps (right) at a) center layer, b) quarter point layer, and c) surface layer of Nb-bearing steel at 670°C soaking for 6 hours

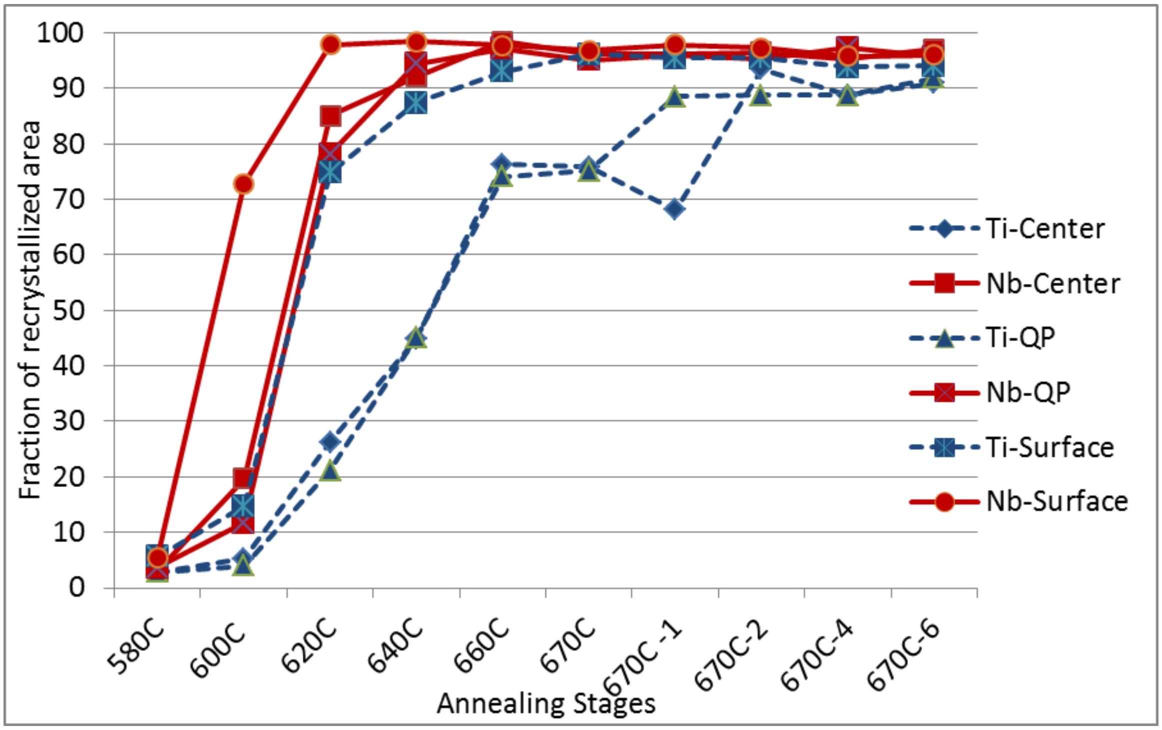

Figure 38. The changing trend of the fraction of recrystallized area (Ti-bearing steel VS Nb-bearing steel) at different annealing temperatures and time

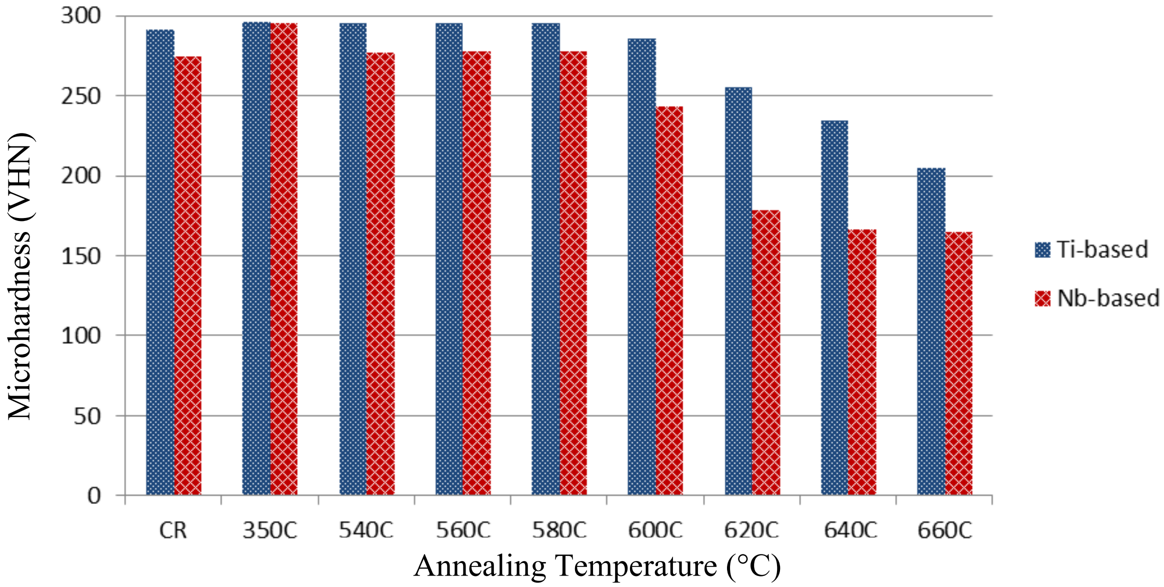

Figure 39. Three layers average microhardness (VHN) changing trend comparison for Ti-bearing steel and Nb-bearing steel

Stored energy distribution maps and changing trends calculated from the EBSD scanning data using the sub-grain method are shown from Figure 40 to Figure 44 and in Table 2. During batch annealing, the stored energy in the full-hard or cold rolled samples was continuously consumed to supply the initial driving force for recovery and recrystallization. The stored energy in Nb-bearing steel was consumed faster than in the Ti-bearing steel, which is consistent with the changing trends of the fraction of recrystallized area as shown in Figure 40, Figure 41 and Figure 42. For cold rolled samples as shown in Figure 43 and Table 2, the stored energy in the surface layer is about 7% higher than the center later for both steels, and the stored energy in Nb-bearing steel is about 10% higher than Ti-bearing steel at both surface and center layers. This could be the answer to the observed different annealing behavior at different locations and different steels. Higher stored energy in the starting cold rolled state supply higher initial driving force for recrystallization which made a higher recrystallization speed. At similar cold work percentage and reduction rate, the stored energy difference in the cold rolled samples can only be inherited from the hot band condition. If the dislocation density, i.e. stored energy, in the hot band condition is higher, more dislocations would be present after cold deformation, which would cause higher stored energy in the cold rolled condition. From Figure 44 and Table 2, the stored energy differences for hot band samples were compared, the difference between surface layer and center layer for the same steel is up to 60% and the difference between different steels at the same sample layer is up to 86%.

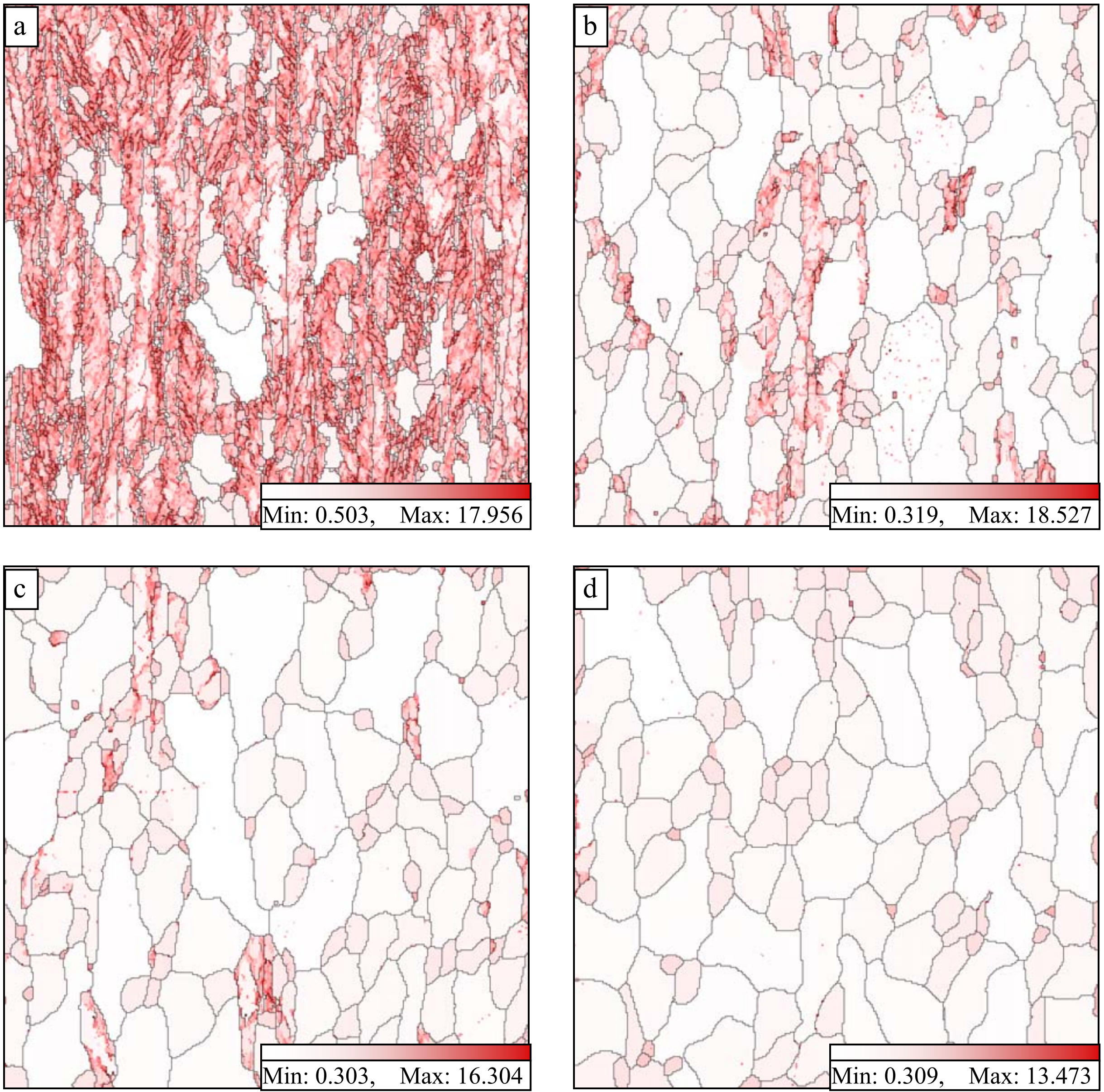

Figure 40. Stored energy distribution maps of Nb-bearing steel at center layer: a) 4.88J/cm^3 at 600°C, b) 1.27J/cm^3 at 620°C, c) 0.92J/cm^3 at 640°C, d) 0.71J/cm^3 at 660°C

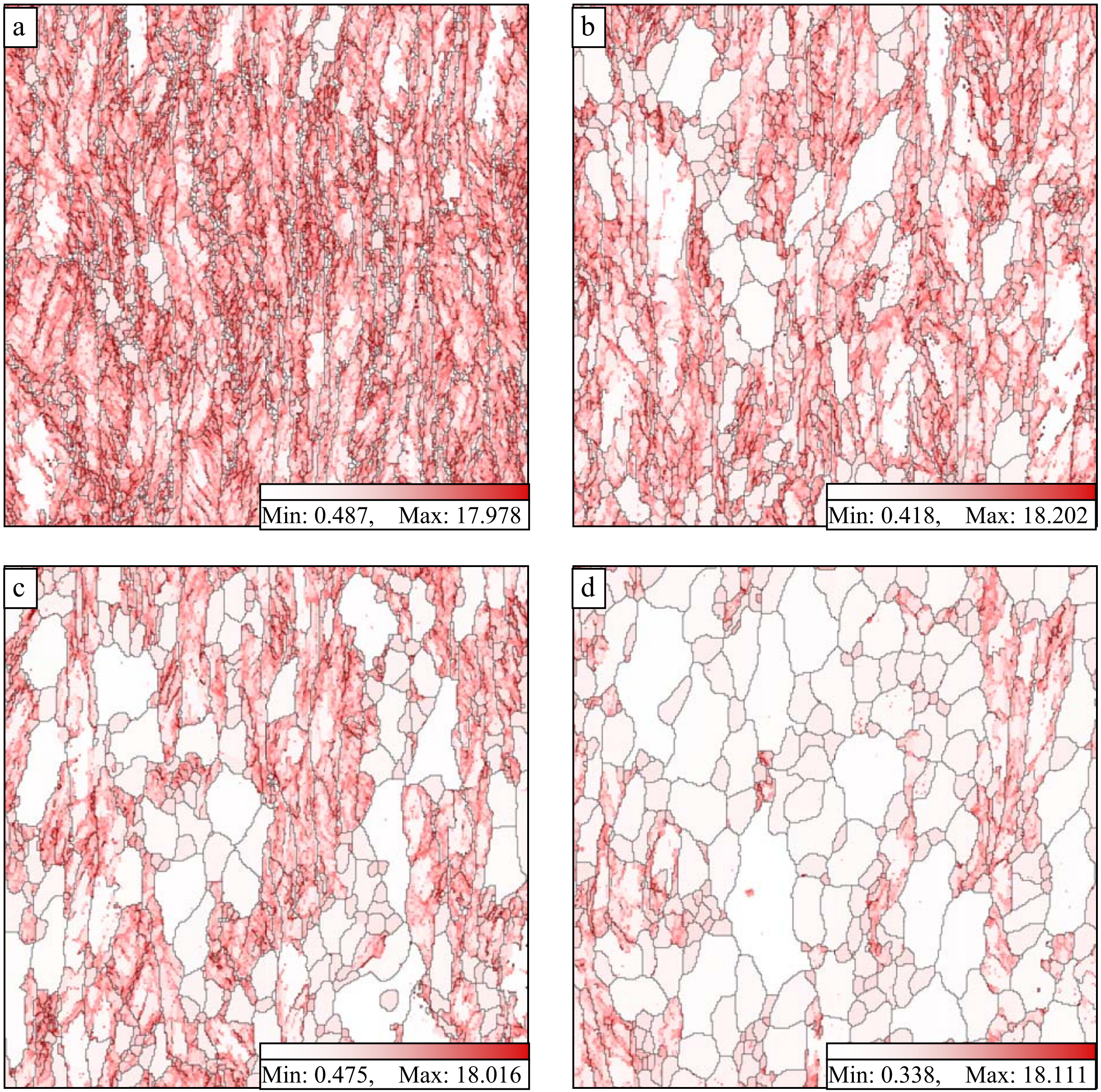

Figure 41. Stored energy distribution maps of Ti-bearing steel at center layer: a) 5.12J/cm^3 at 600°C, b) 3.73J/cm^3 at 620°C, c) 3.08J/cm^3 at 640°C, d) 1.64J/cm^3 at 660°C

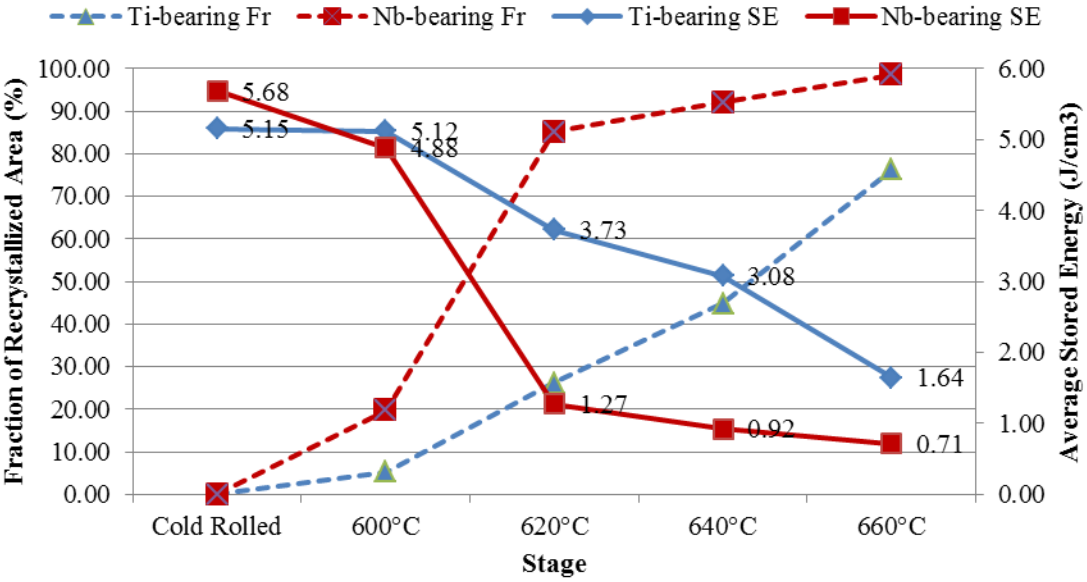

Figure 42. The average stored energy of scanned area at center layers and the fraction of recrystallized area changing trends during annealing

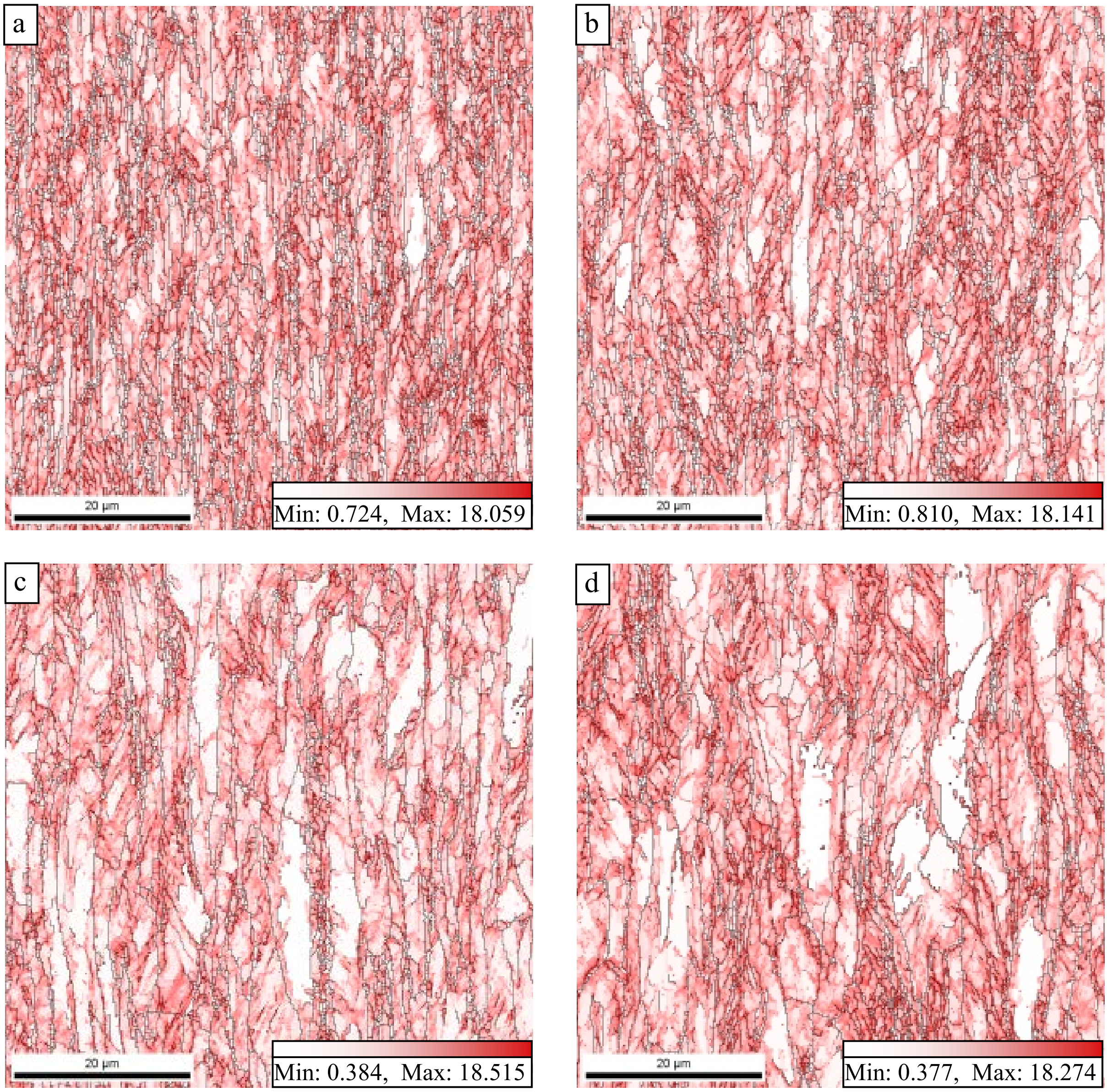

Figure 43. Stored energy distribution maps for cold rolled samples of a) Nb steel at surface layer, b) Nb steel at center layer, c) Ti steel at surface layer, d) Ti steel at center layer

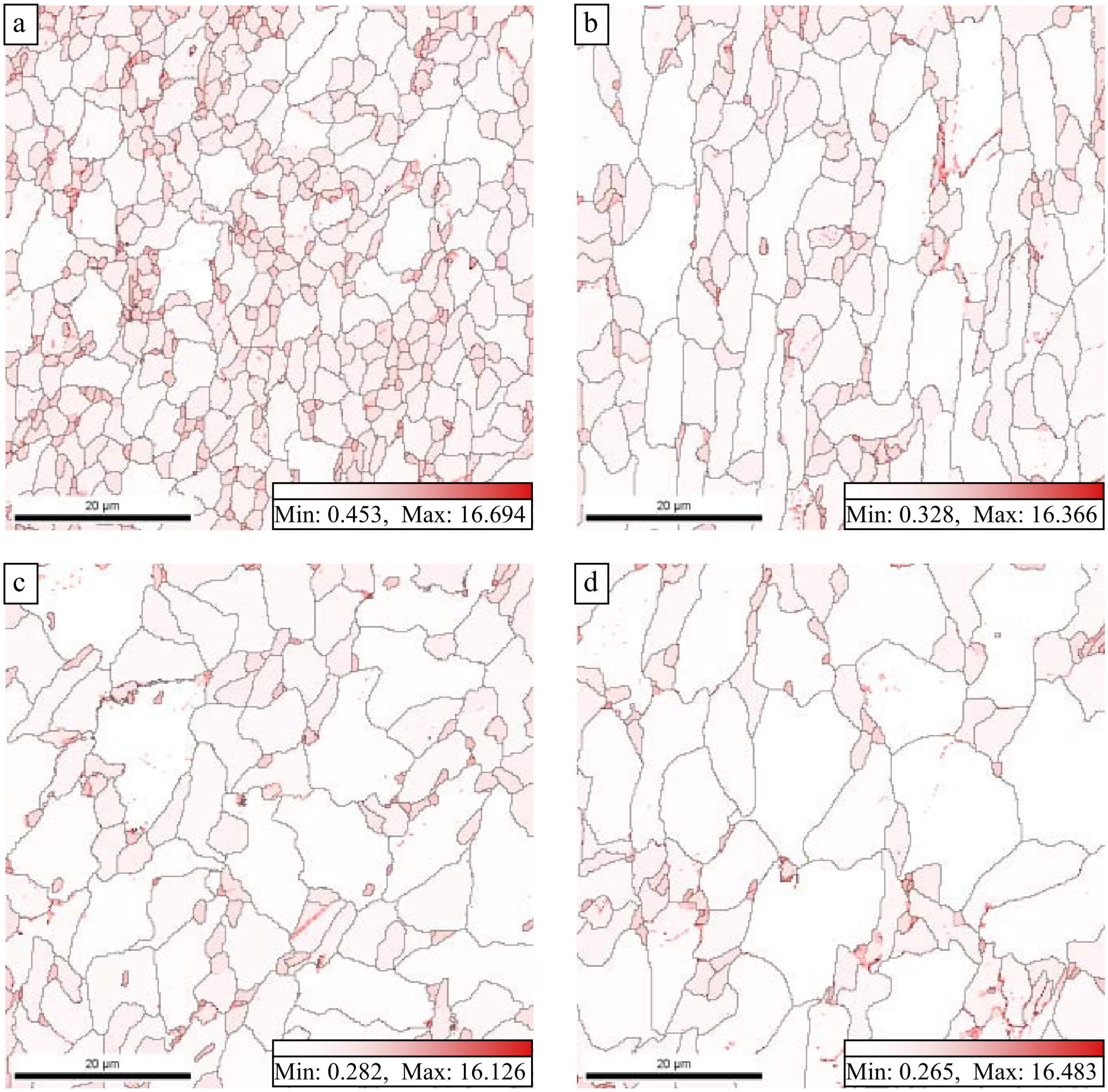

Figure 44. Stored energy distribution maps for hot band samples of a) Nb steel at surface layer, b) Nb steel at center layer, c) Ti steel at surface layer, d) Ti steel at center layer

Table 2. Comparison of the stored energy of hot band and cold rolled samples

	Nb-Steel Surface	Nb-Steel Center	Ti-Steel Surface	Ti-Steel Center
Hot Band	1.40J/cm^3	0.87J/cm^3	0.75J/cm^3	0.65J/cm^3
Cold Rolled	6.09J/cm^3	5.68J/cm^3	5.52J/cm^3	5.15J/cm^3

Stored energy distribution is not random or uniform. It's texture or orientation dependent. The stored energy around γ-fiber ({111} parallel to the normal direction) area is normally higher than that around α-fiber ({101} parallel to the rolling direction) area because more severe deformation normally happens around γ-fiber area. This was confirmed in this study by comparing the Crystal Direction map (Figure 45) from EBSD data and the stored energy distribution map (Figure 46). The green area in the Crystal Direction map stands for α-fiber area. The corresponding area in the stored energy distribution map shows less intense color, which stands for lower stored energy than the blue area (γ-fiber area) in the Crystal Direction map. If the fraction of γ-fiber in the Nb-bearing steel is much higher than that in the Ti-bearing steel, the higher stored energy area would be larger in the Nb-bearing steel, which could be a reason to cause the higher recrystallization speed of Nb-bearing steel. But after comparison of the texture fiber distribution maps, it's found that the fraction of both γ-fiber area and α-fiber area for both steels are at the same level as shown in Figure 47 and Figure 48. The fraction of γ-fiber is 27.7% in Ti-bearing steel versus 27.4% in Nb-bearing steel, and the fraction of α -fiber is 45.7% in Ti-bearing steel versus 48.4% in Nb-bearing steel. So the texture factor does not seem to be a critical reason to make the different annealing speed.

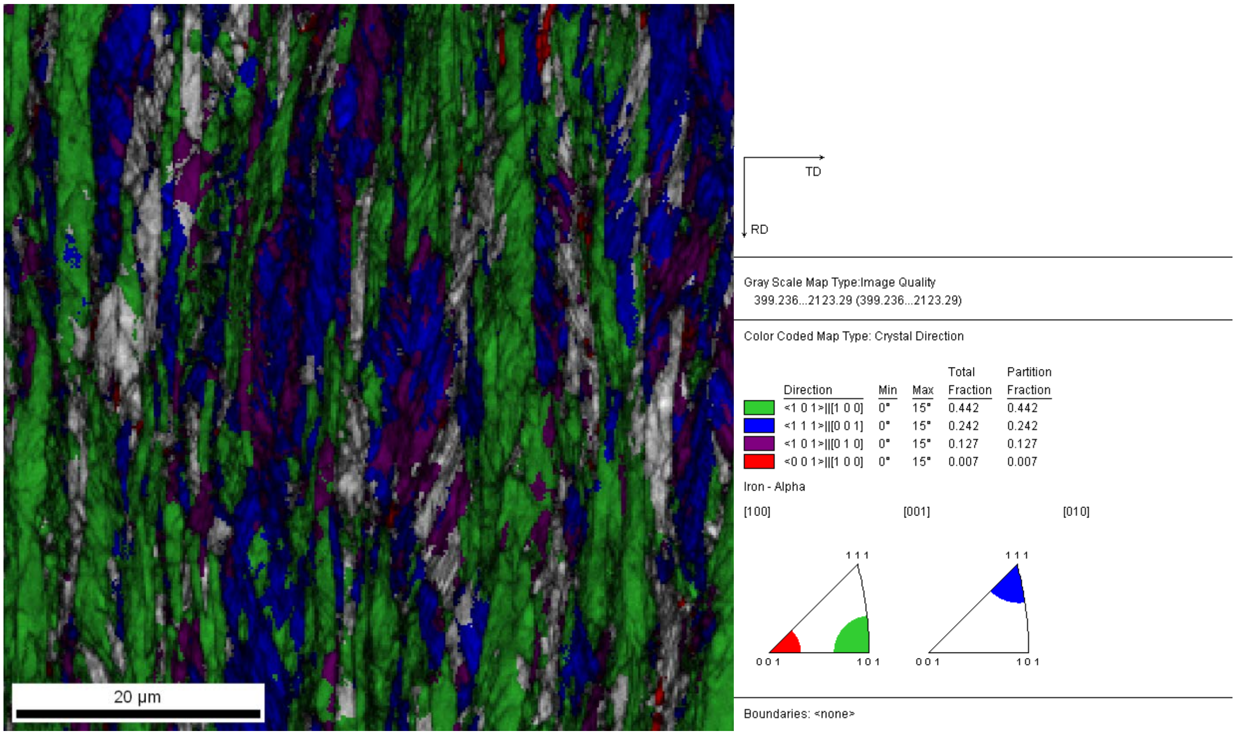

Gray Scale Map Type:Image Quality
399.236...2123.29 (399.236...2123.29)

Color Coded Map Type: Crystal Direction

	Direction	Min	Max	Total Fraction	Partition Fraction
🟩	<1 0 1>||[1 0 0]	0°	15°	0.442	0.442
🟦	<1 1 1>||[0 0 1]	0°	15°	0.242	0.242
🟪	<1 0 1>||[0 1 0]	0°	15°	0.127	0.127
🟥	<0 0 1>||[1 0 0]	0°	15°	0.007	0.007

Boundaries: <none>

Figure 45. EBSD Crystal Direction map of cold rolled Nb-bearing steel

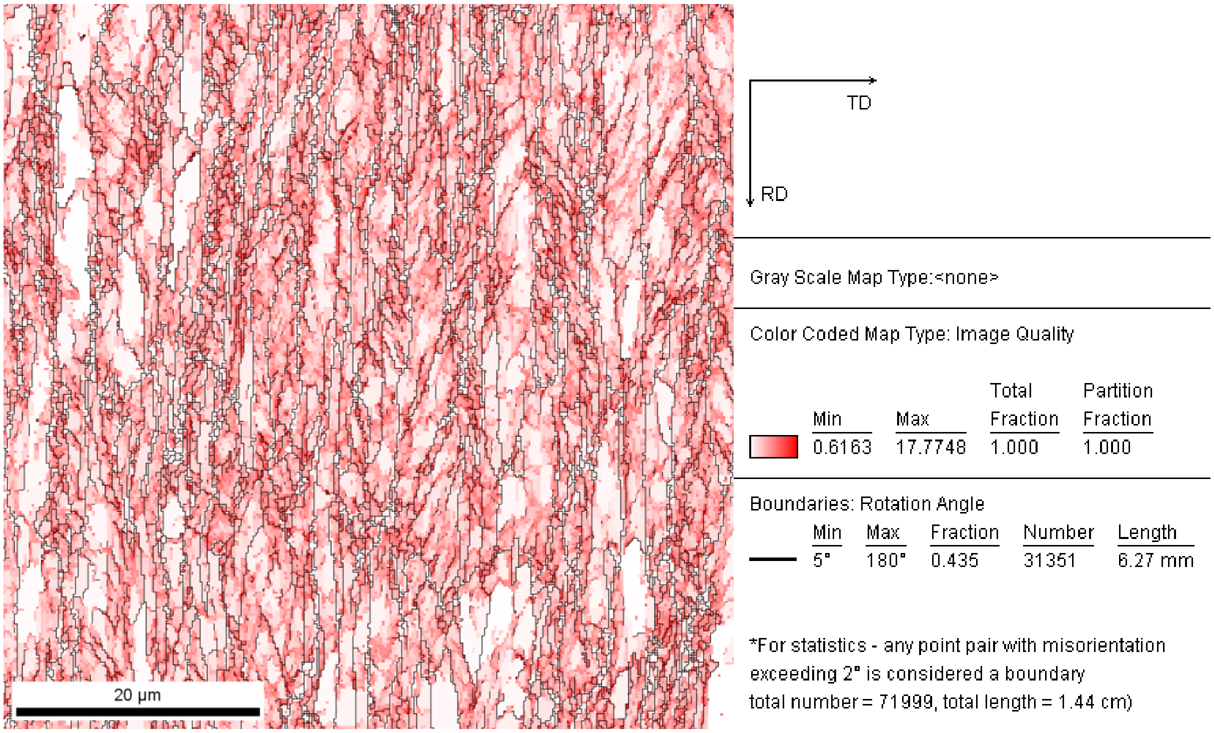

Gray Scale Map Type:<none>

Color Coded Map Type: Image Quality

	Min	Max	Total Fraction	Partition Fraction
🟥	0.6163	17.7748	1.000	1.000

Boundaries: Rotation Angle

	Min	Max	Fraction	Number	Length
—	5°	180°	0.435	31351	6.27 mm

*For statistics - any point pair with misorientation
exceeding 2° is considered a boundary
total number = 71999, total length = 1.44 cm)

Figure 46. Stored energy distribution map of cold rolled Nb-bearing steel

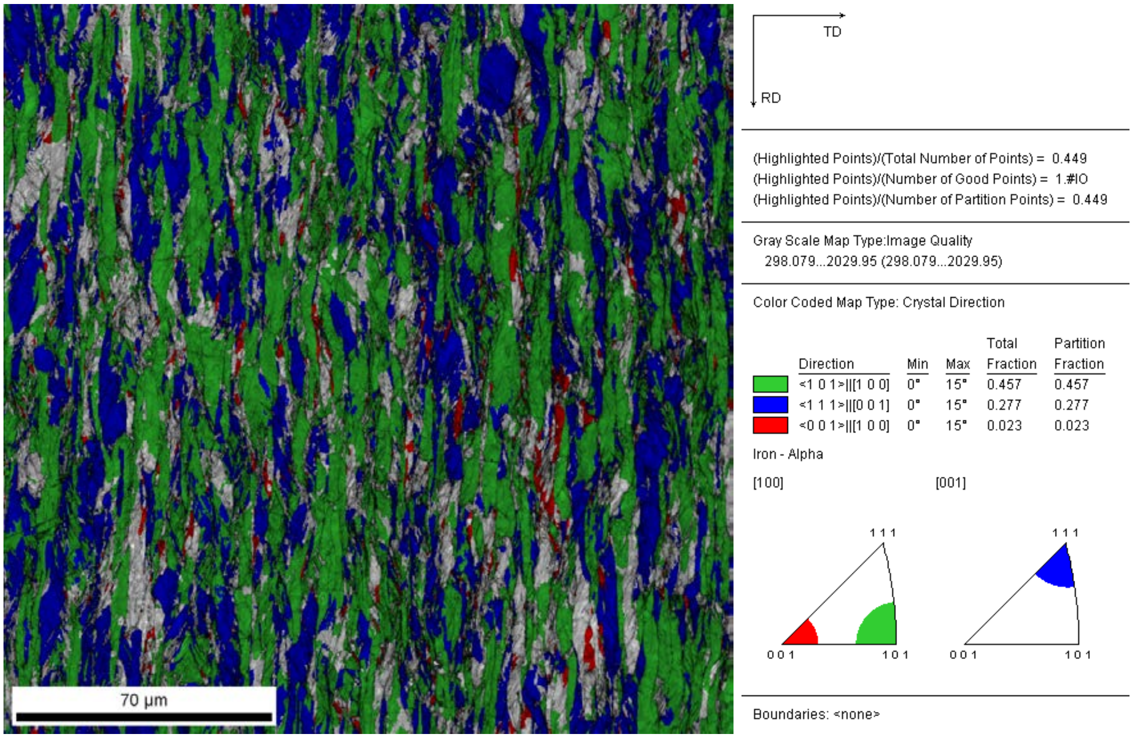

(Highlighted Points)/(Total Number of Points) = 0.449
(Highlighted Points)/(Number of Good Points) = 1.#IO
(Highlighted Points)/(Number of Partition Points) = 0.449

Gray Scale Map Type:Image Quality
298.079...2029.95 (298.079...2029.95)

Color Coded Map Type: Crystal Direction

	Direction	Min	Max	Total Fraction	Partition Fraction
🟩	<1 0 1>||[1 0 0]	0°	15°	0.457	0.457
🟦	<1 1 1>||[0 0 1]	0°	15°	0.277	0.277
🟥	<0 0 1>||[1 0 0]	0°	15°	0.023	0.023

Iron - Alpha

Boundaries: <none>

Figure 47. EBSD Crystal Direction map of cold rolled Ti-bearing steel showing texture fibers

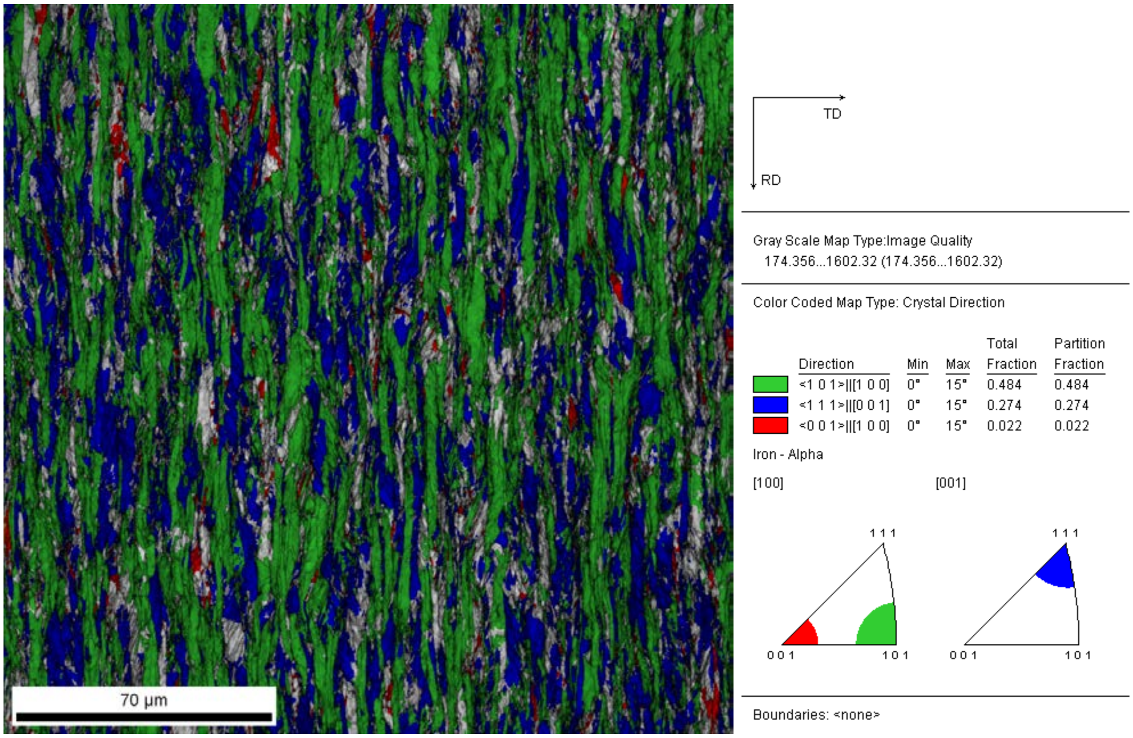

Gray Scale Map Type:Image Quality
174.356...1602.32 (174.356...1602.32)

Color Coded Map Type: Crystal Direction

	Direction	Min	Max	Total Fraction	Partition Fraction
🟩	<1 0 1>||[1 0 0]	0°	15°	0.484	0.484
🟦	<1 1 1>||[0 0 1]	0°	15°	0.274	0.274
🟥	<0 0 1>||[1 0 0]	0°	15°	0.022	0.022

Iron - Alpha

Boundaries: <none>

Figure 48. EBSD Crystal Direction map of cold rolled Nb-bearing steel showing texture fibers

Precipitation behavior of both steels was theoretically calculated and experimentally observed using SEM, EDS, TEM, and HRTEM in this study (Figures 49 to 109). Based on the concentration of Nb, Ti, C, and N elements in the steels, the maximum amount of precipitates that could be formed was calculated. For Ti-bearing steel, the density of ferrite is 7.8773g/cm^3, the density of TiC is about 4.93 g/cm^3. So the maximum volume fraction of TiC, $f_v(TiC)_{MAX}$, can be calculated in equation 1:

$$f_v(TiC)_{MAX}=W_{TiC} \times (D_{Ferrite} / D_{TiC}) = 1.5978W_{TiC}$$

. Since

$$W_{TiC}= W_{Ti} \times [1 + (\text{Atom Weight})_C / (\text{Atom Weight})_{Ti}] = 1.251W_{Ti}$$

, so

$$f_v(TiC)_{MAX} = 1.5978\ W_{TiC} = 1.5978 \times 1.251\ W_{Ti} = 1.9988W_{Ti}$$

.The concentrations of C, N, and Ti in weight percent are 0.0455, 0.0086, and 0.0577 respectively. If Ti will be partially consumed by forming TiN, one Ti will need 3.42 times of N, so 0.0294 weight percent of Ti will be consumed by N. Then 0.0283 weight percent will be left to form TiC as long as there are enough C. Assuming $W_{Ferrite}$ is 1g and W_{Ti} is:

$$W_{Ti}=(W\%)_{Ti} / 100$$

, then

$$f_v(TiC)_{MAX} =1.9988W_{Ti} = 1.9988 \times 0.0283 / 100 = 5.6566 \times 10^{-4}$$

. If no TiN was formed in the Ti-bearing steel during recrystallization, the maximum volume fraction of TiC precipitates would be:

$$f_v(TiC)_{MAX} =1.9988W_{Ti} = 1.9988 \times 0.0577 / 100 = 11.5331 \times 10^{-4}$$

.

For Nb-bearing steel, using same method, we can calculate that the maximum volume fraction of NbC would be:

$$f_v(NbC)_{MAX} = 1.1397W_{Nb}$$

.The concentrations of C, N, and Nb in weight percent are 0.0526, 0.0073, a nd 0.0317 respectively. If Nb will be partially consumed by forming NbN, one Nb will need 6.636 times of N, so 0.0073 weight percent of N will consume 0.0484 weight percent of Nb, which means Nb will be consumed out by N. If no N bN was formed in the Nb-bearing steel during recrystallization, the maximum volume fraction of NbC precipitates would be:

$$f_v(NbC)_{MAX} = 1.1397W_{Nb} = 1.1397W_{Nb} \times 0.0317 / 100 = 3.6128 \times 10^{-4}$$

. From the calculation, the volume fraction TiC precipitates formed in Ti-bearing steel should be much higher than NbC precipitates formed in Nb-bearing steel. This situation was confirmed by experimental observations. Actually, no NbC or any other precipitates were observed in the partially or fully recrystallized cold rolled Nb-bearing steel. But TiC precipitates were observed in the partially or fully recrystallized cold rolled Ti-bearing steel. The TiC precipitates were not observed in the hot band Ti-bearing steel, which meant that the TiC precipitates were formed during the annealing process. The orientation relationship between the TiC precipitate and the ferrite matrix further confirmed this conclusion. The diameters of TiC precipitates in the annealed Ti-bearing steel which could be observed were from 2nm to 50nm, the average is around 15nm. Assuming all the Ti elements were precipitated as TiC, the Zener pinning pressure can be calculated:

$$P_Z = \frac{3F_V\gamma}{2r} = 3 \times (11.5331\times10^{-4}) \times \gamma \div (15\times10^{-9}) = 2.3066 \times 10^{5}\gamma$$

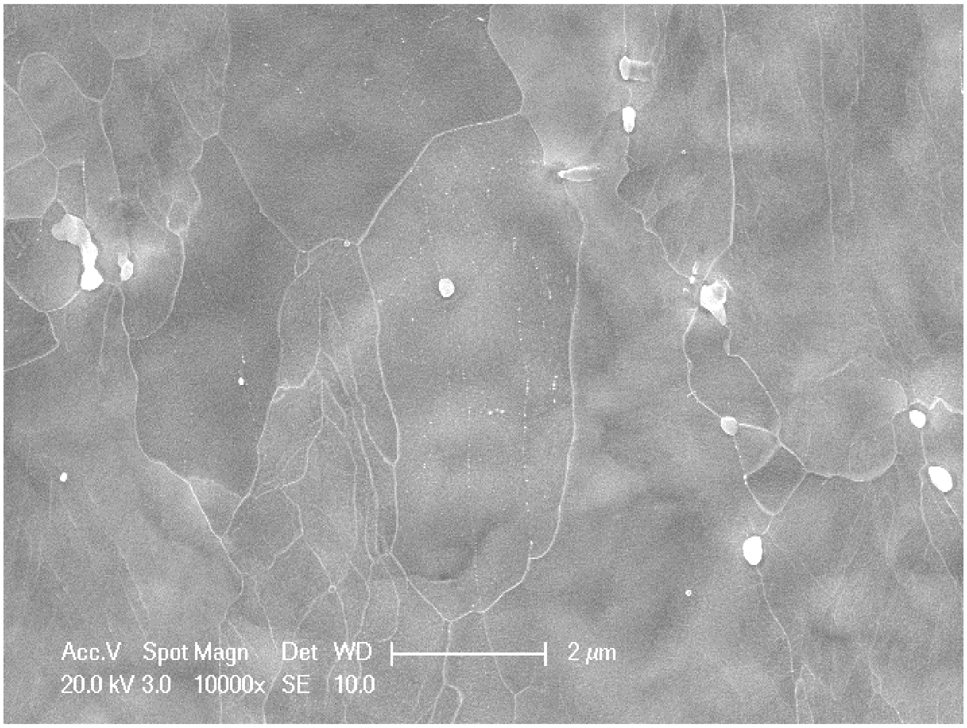

Figure 49. TiC precipitates in Ti-bearing steel at 640°C (location 1 & SEM 10000X)

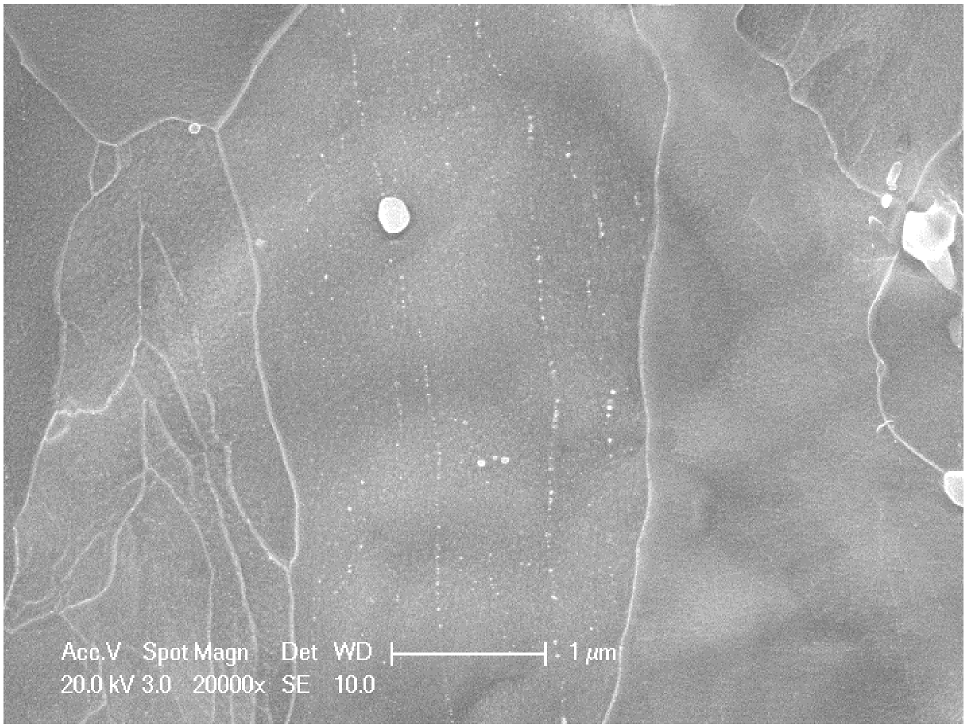

Figure 50. TiC precipitates in Ti-bearing steel at 640°C (location 1 & SEM 20000X)

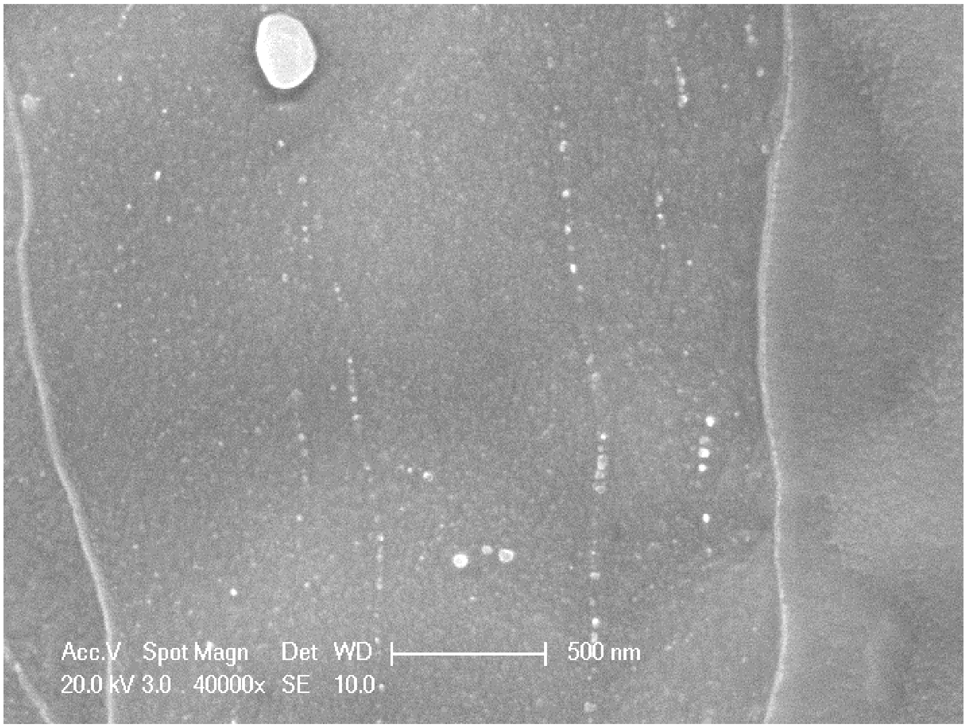

Figure 51. TiC precipitates in Ti-bearing steel at 640°C (location 1 & SEM 40000X)

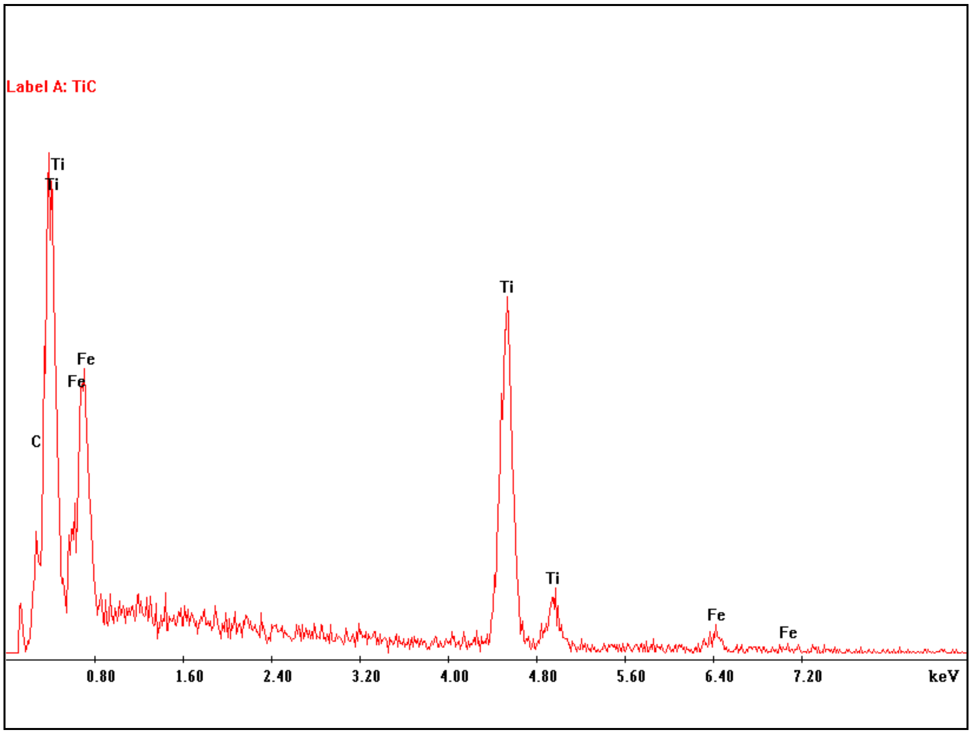

Figure 52. TiC precipitates in Ti-bearing steel at 640°C (location 1 & EDS)

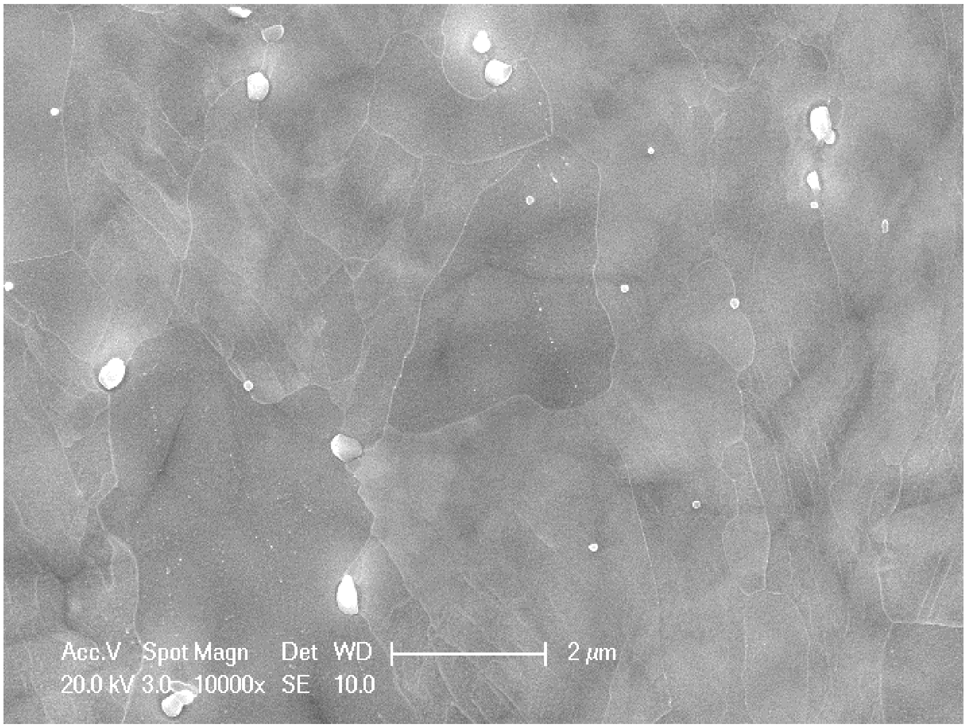

Figure 53. TiC precipitates in Ti-bearing steel at 640°C (location 2 & SEM 10000X)

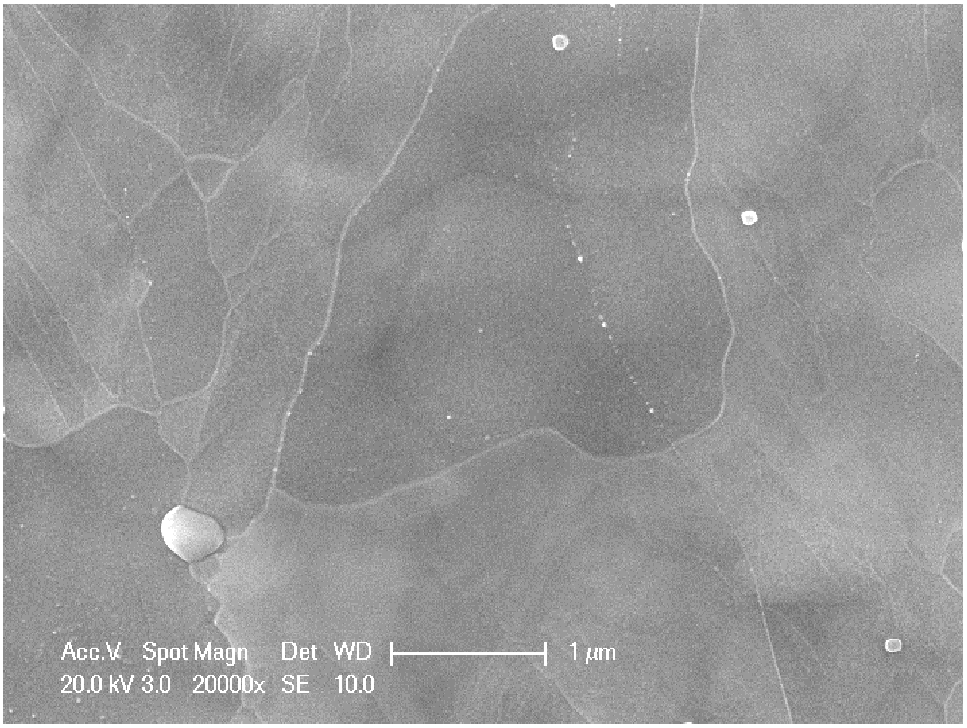

Figure 54. TiC precipitates in Ti-bearing steel at 640°C (location 2 & SEM 20000X)

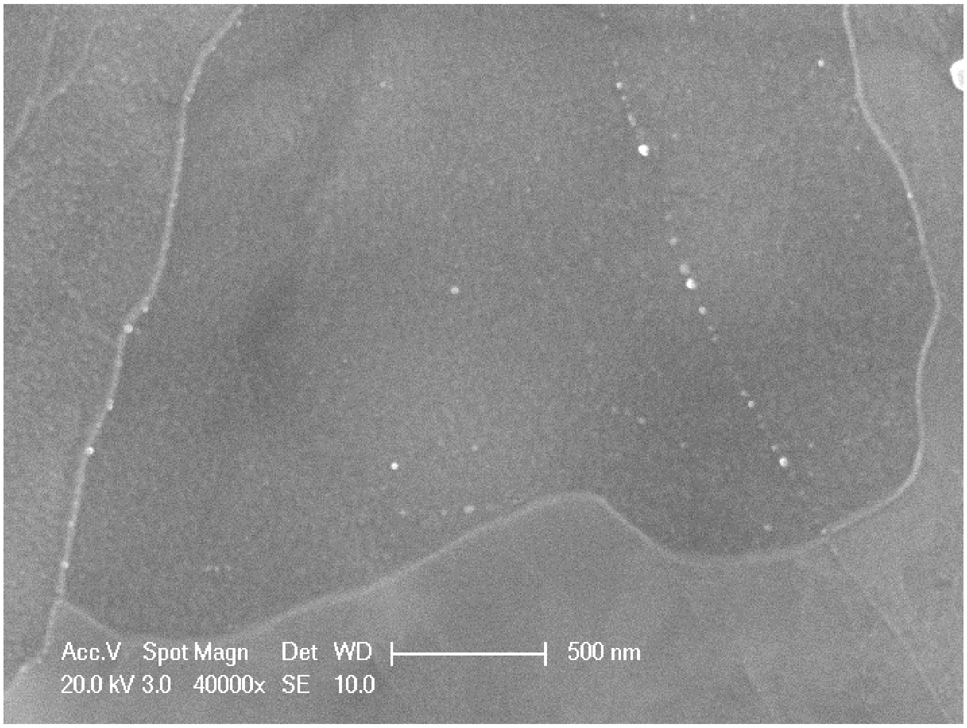

Figure 55. TiC precipitates in Ti-bearing steel at 640°C (location 2 & SEM 40000X)

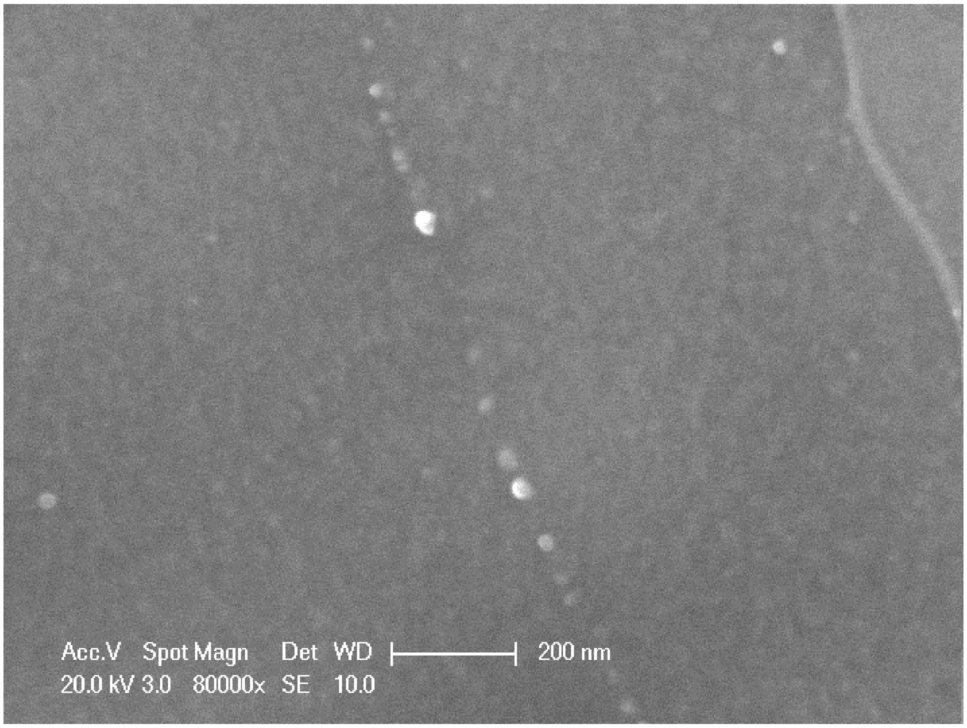

Figure 56. TiC precipitates in Ti-bearing steel at 640°C (location 2 & SEM 80000X a)

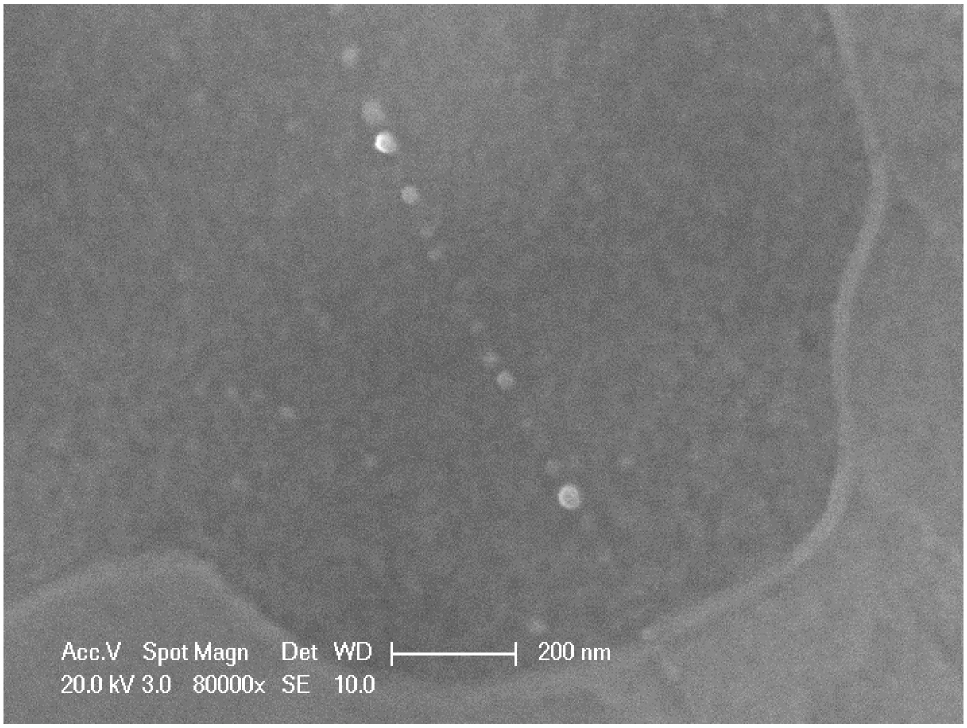

Figure 57. TiC precipitates in Ti-bearing steel at 640°C (location 2 & SEM 80000X b)

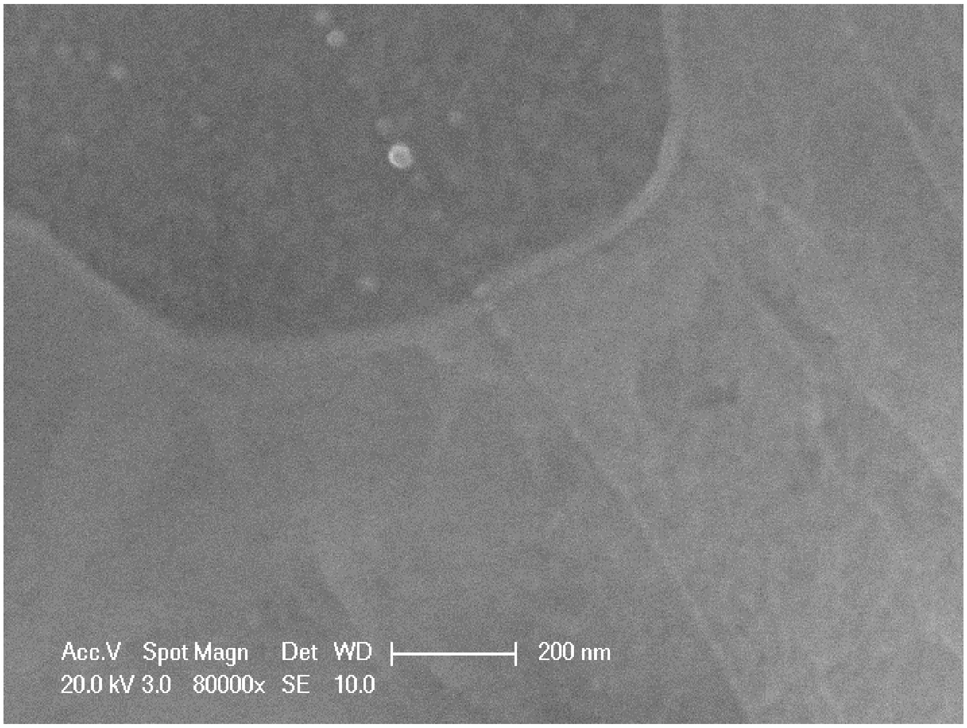

Figure 58. TiC precipitates in Ti-bearing steel at 640°C (location 2 & SEM 80000X c)

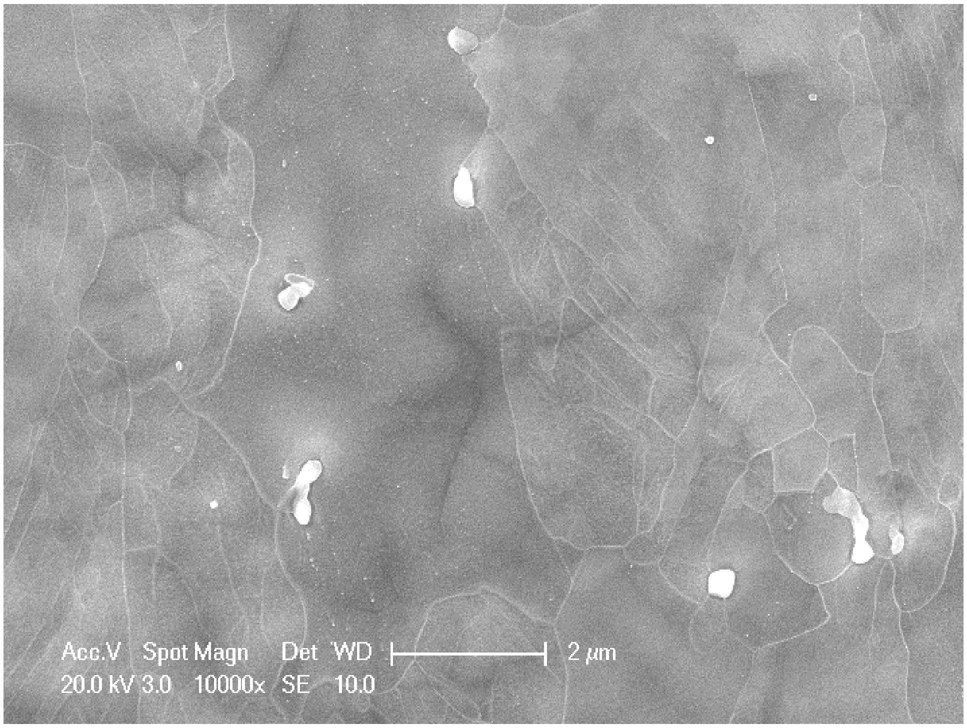

Figure 59. TiC precipitates in Ti-bearing steel at 640°C (location 3 & SEM 10000X)

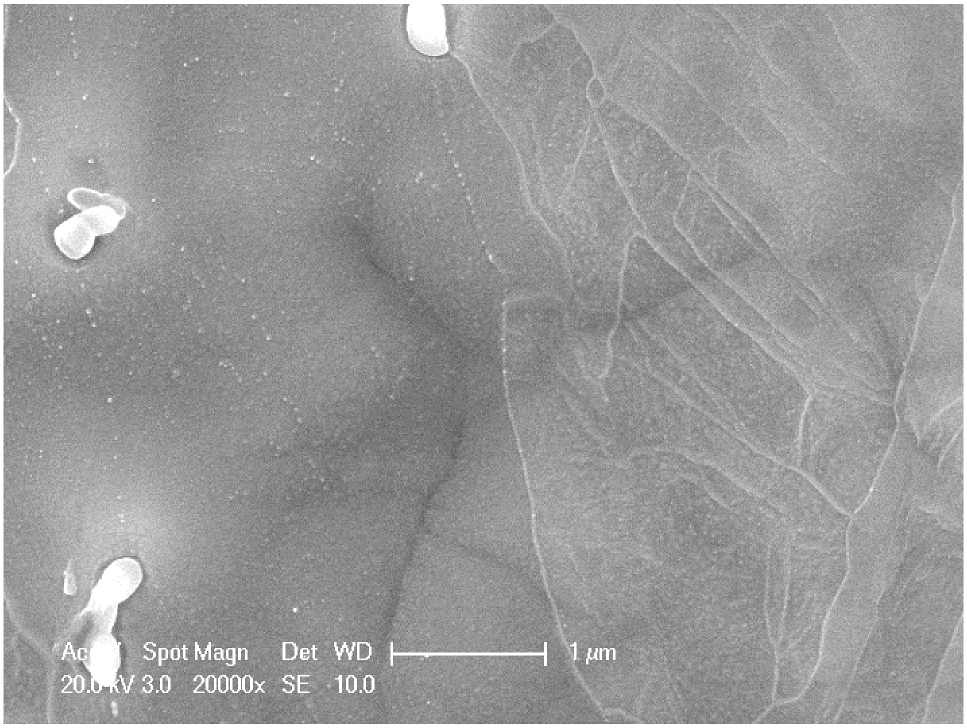

Figure 60. TiC precipitates in Ti-bearing steel at 640°C (location 3 & SEM 20000X)

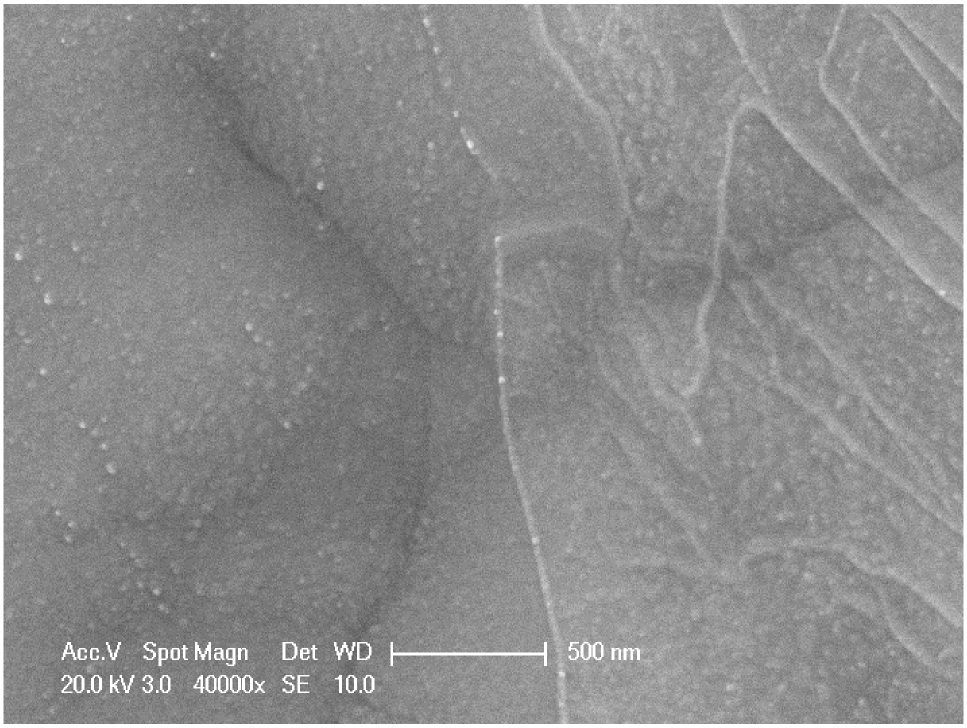

Figure 61. TiC precipitates in Ti-bearing steel at 640°C (location 3 & SEM 40000X)

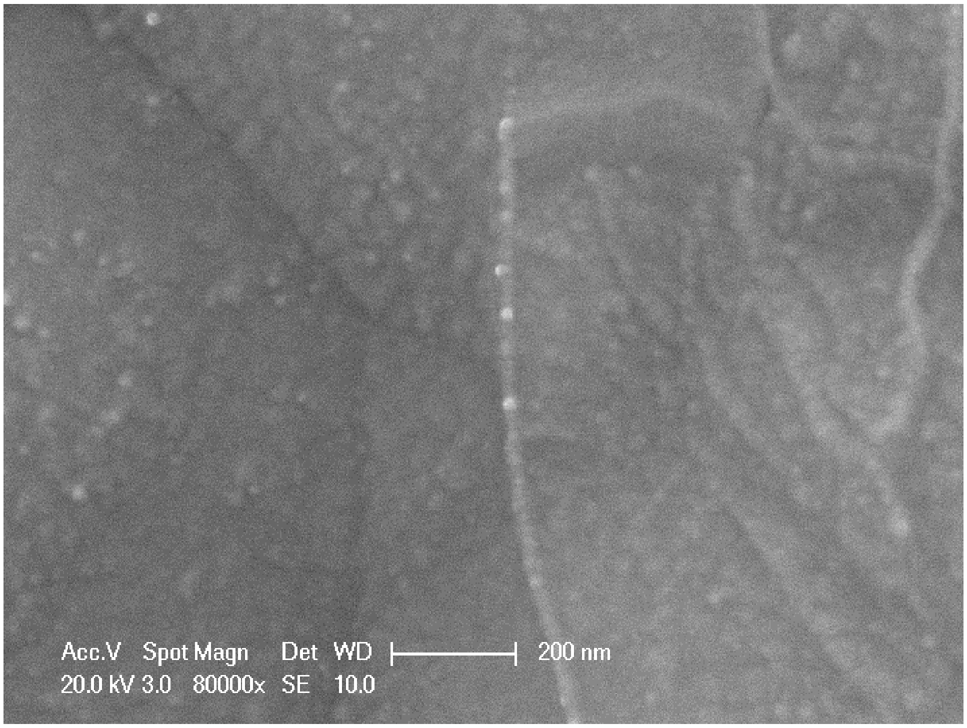

Figure 62. TiC precipitates in Ti-bearing steel at 640°C (location 3 & SEM 80000X)

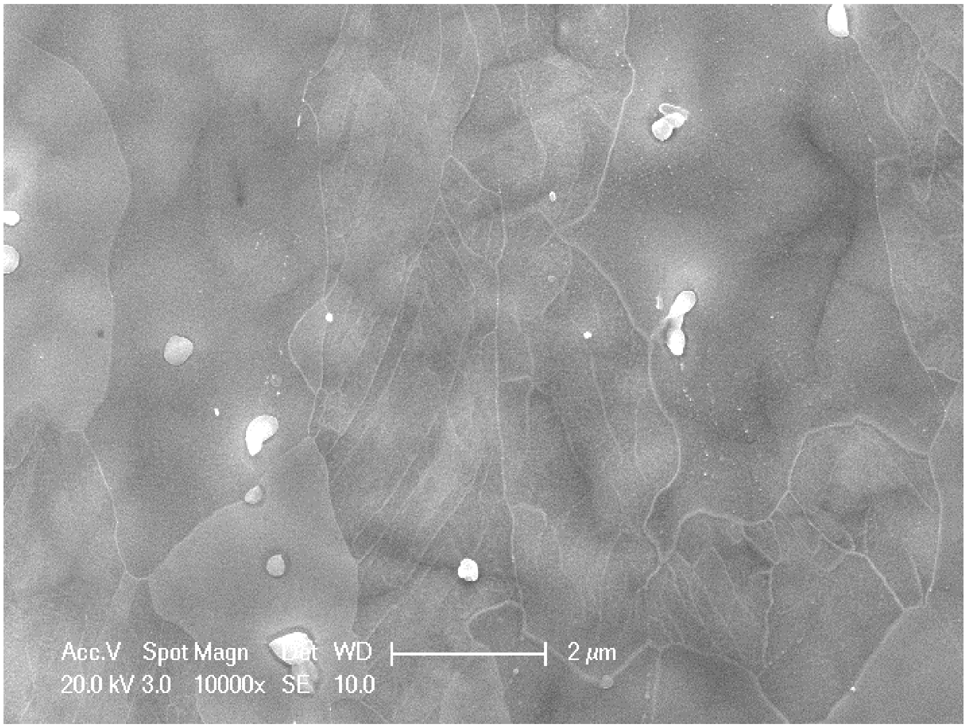

Figure 63. TiC precipitates in Ti-bearing steel at 640°C (location 4 & SEM 10000X)

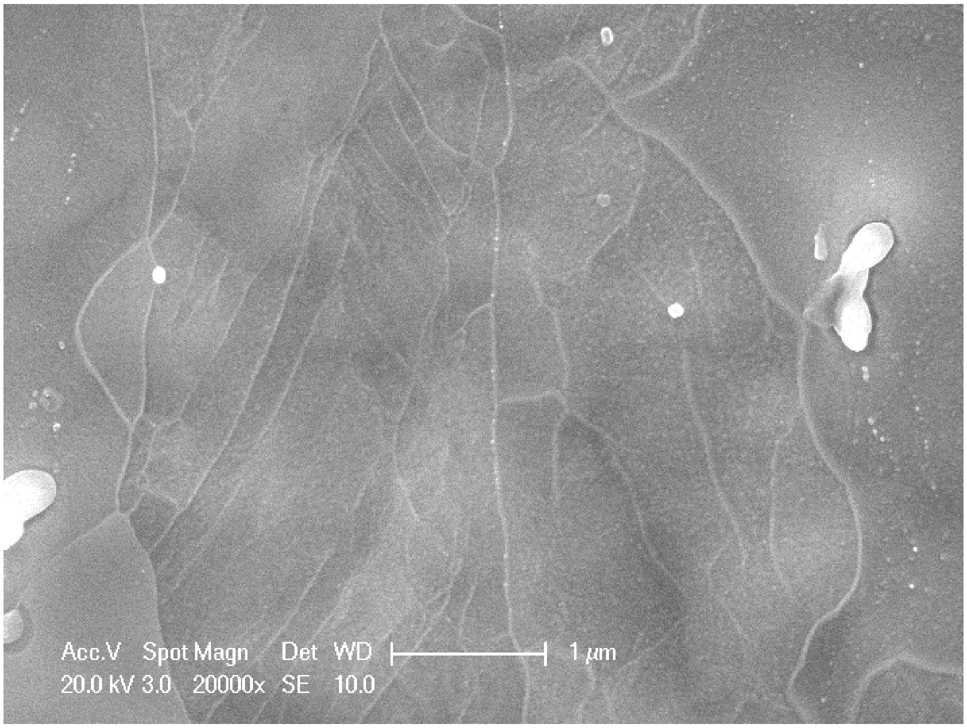

Figure 64. TiC precipitates in Ti-bearing steel at 640°C (location 4 & SEM 20000X)

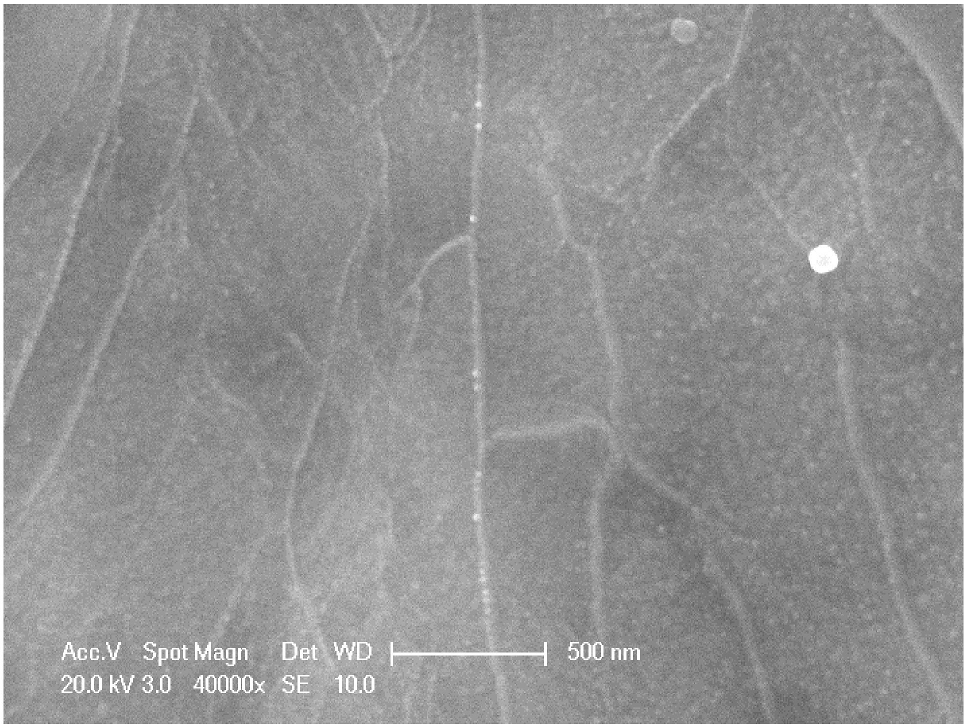

Figure 65. TiC precipitates in Ti-bearing steel at 640°C (location 4 & SEM 40000X)

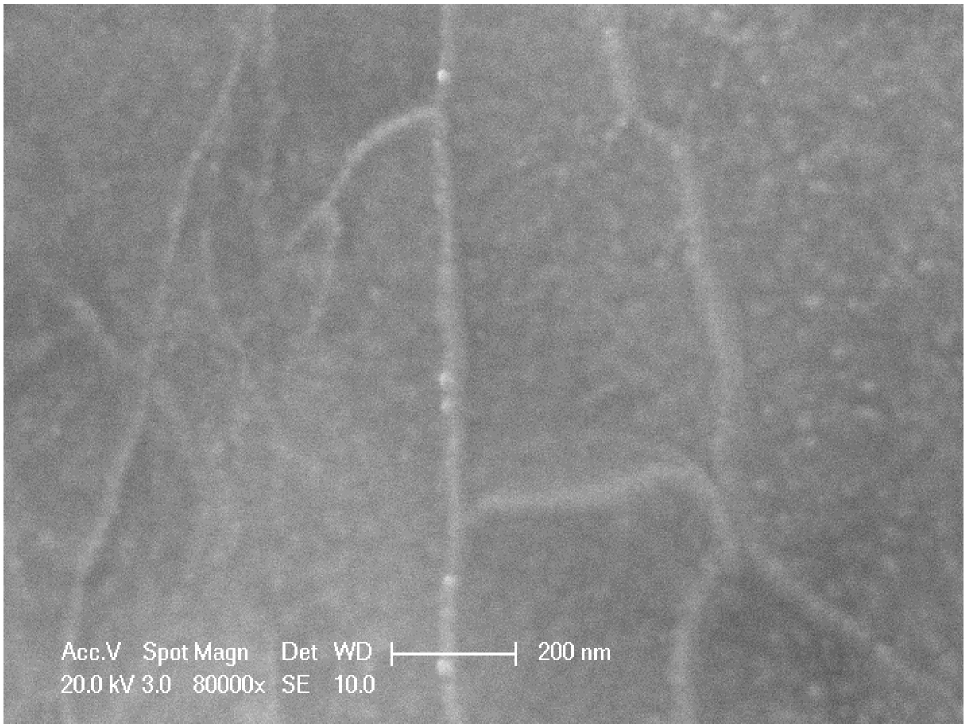

Figure 66. TiC precipitates in Ti-bearing steel at 640°C (location 4 & SEM 80000X)

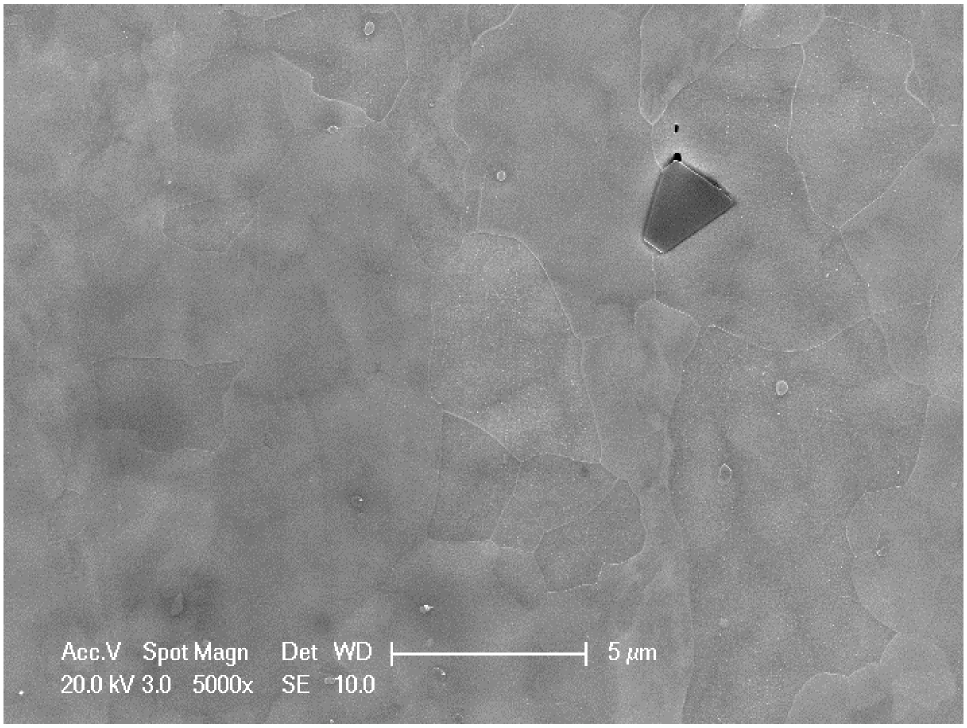

Figure 67. TiC precipitates in Ti-bearing steel at 660°C (location 1 & SEM 5000X)

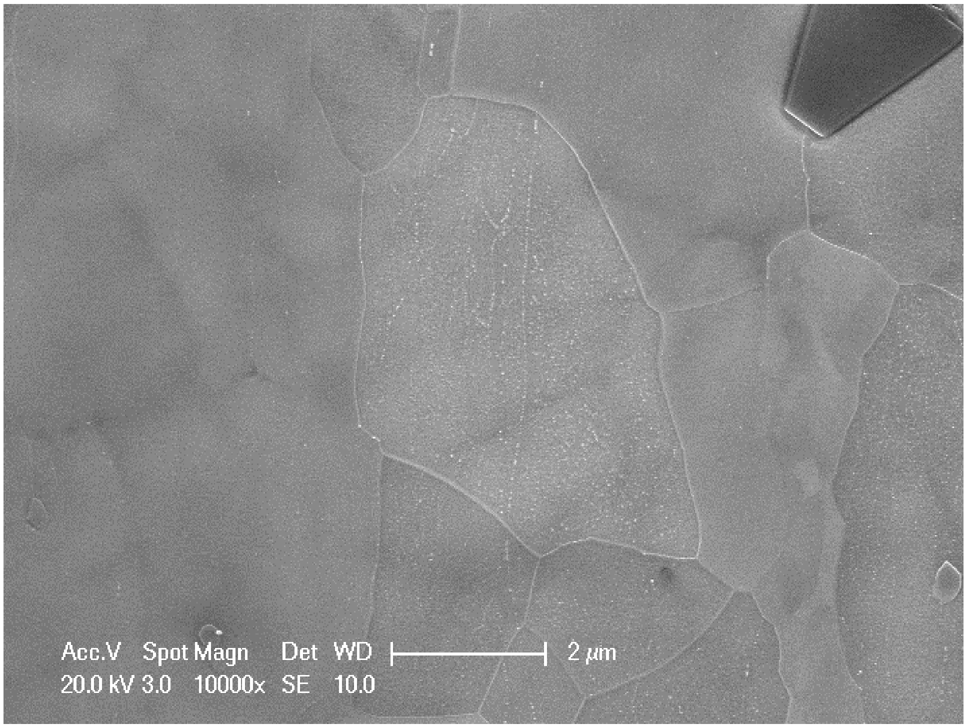

Figure 68. TiC precipitates in Ti-bearing steel at 660°C (location 1 & SEM 10000X)

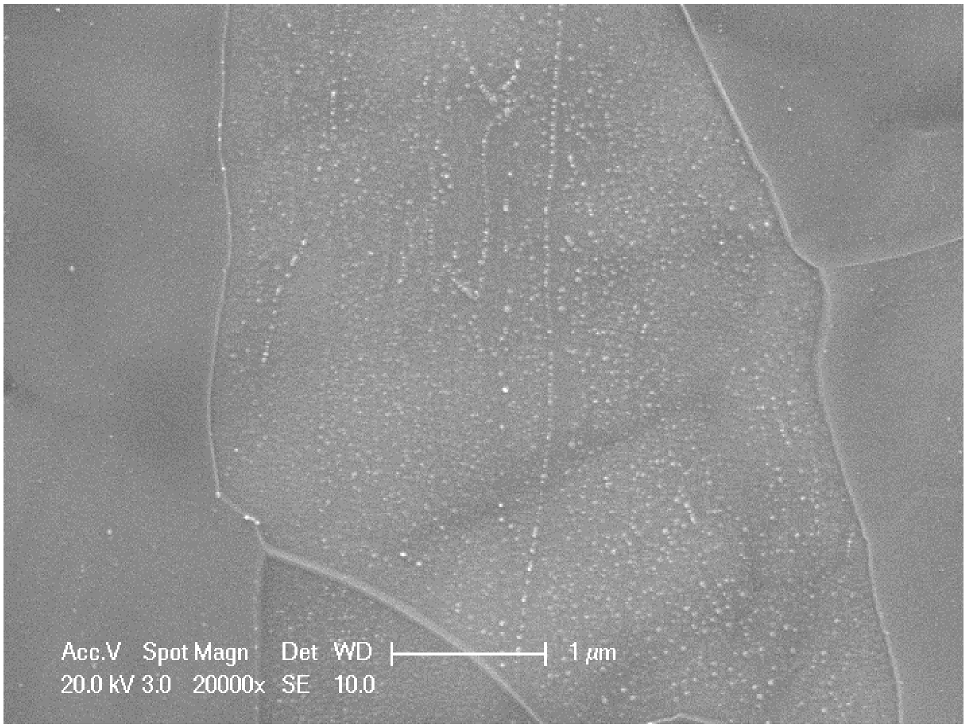

Figure 69. TiC precipitates in Ti-bearing steel at 660°C (location 1 & SEM 20000X)

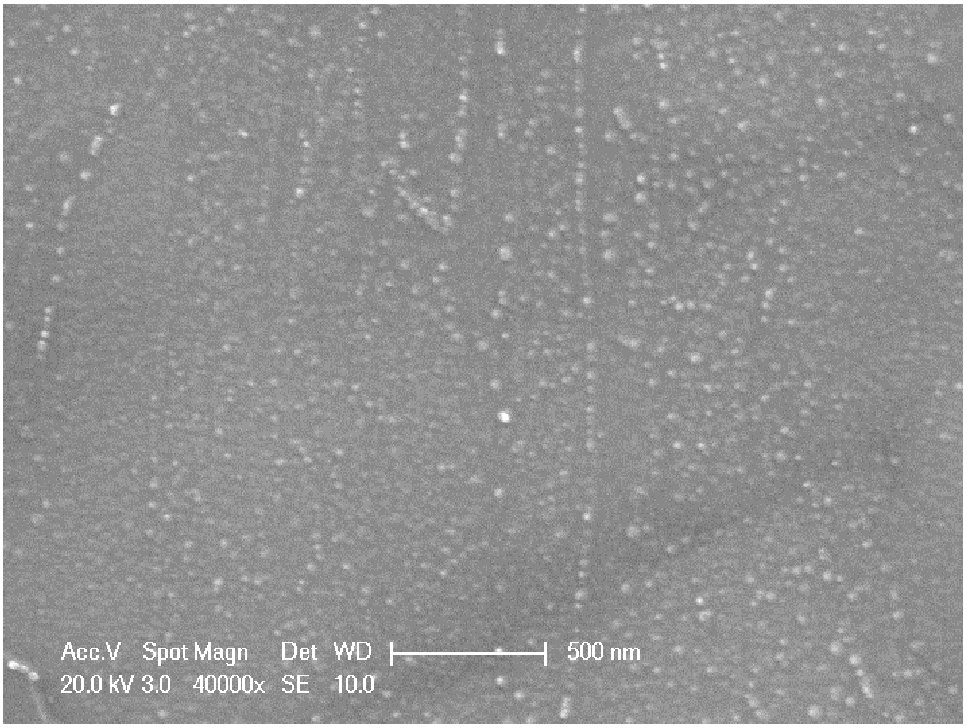

Figure 70. TiC precipitates in Ti-bearing steel at 660°C (location 1 & SEM 40000X)

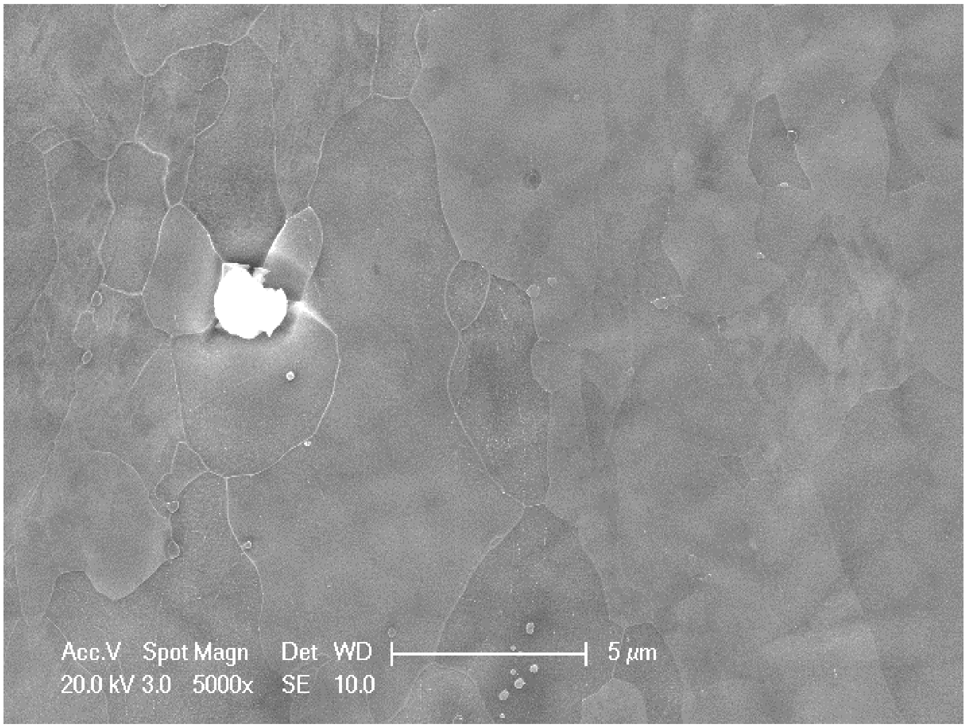

Figure 71. TiC precipitates in Ti-bearing steel at 660°C (location 2 & SEM 5000X)

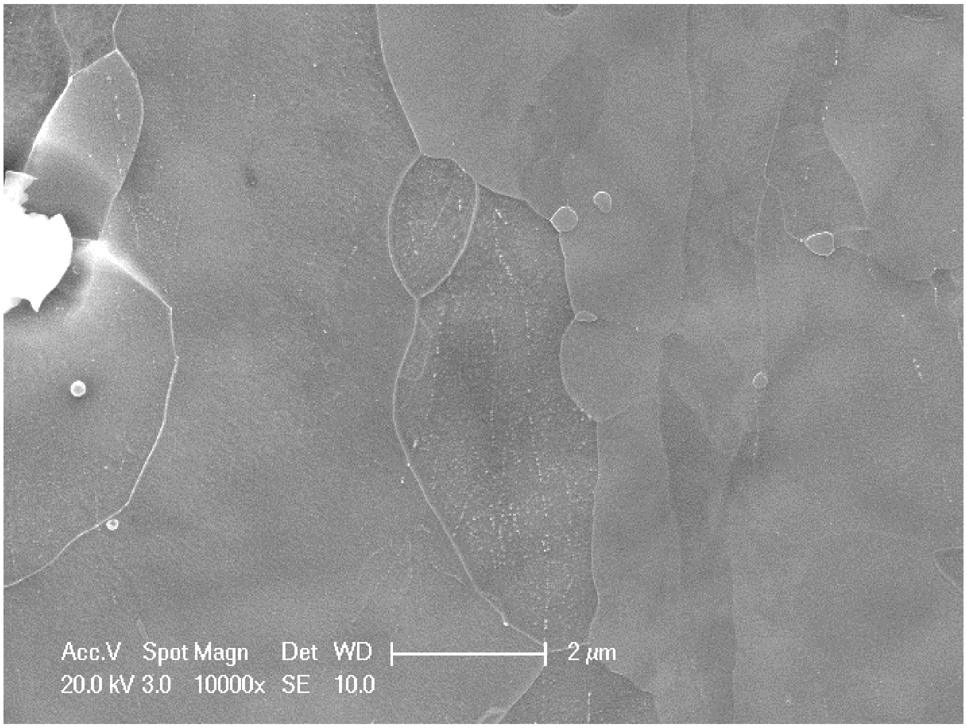

Figure 72. TiC precipitates in Ti-bearing steel at 660°C (location 2 & SEM 10000X)

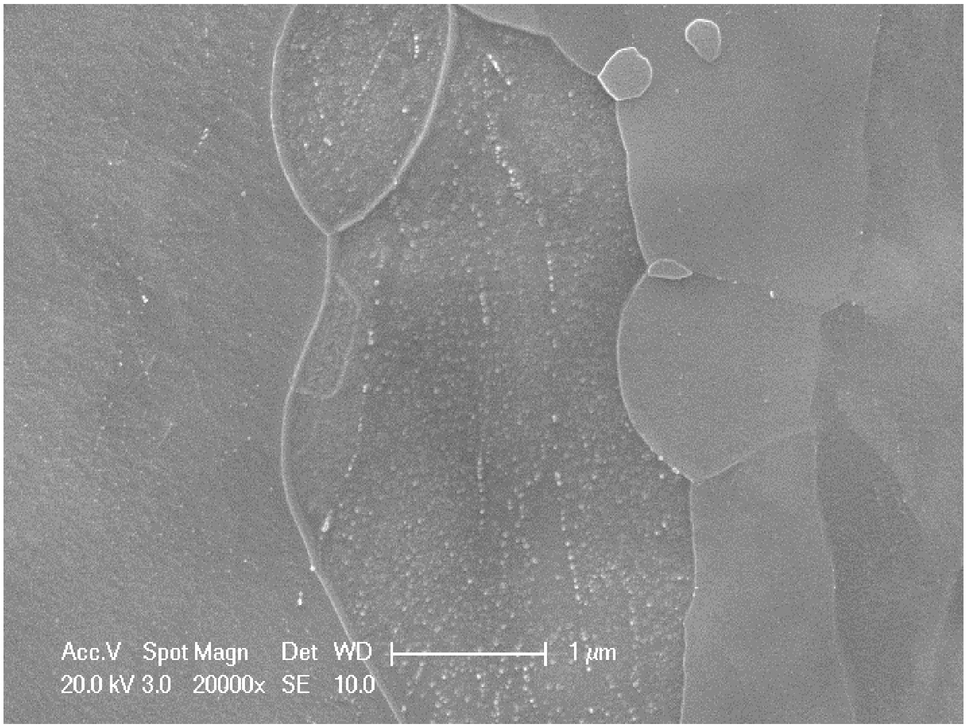

Figure 73. TiC precipitates in Ti-bearing steel at 660°C (location 2 & SEM 20000X)

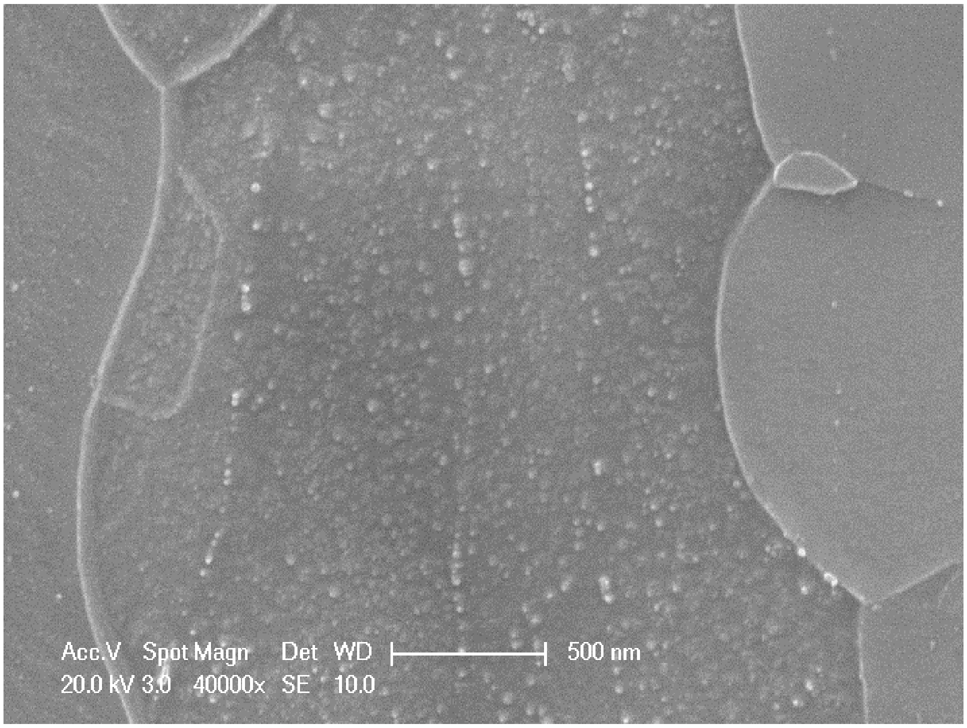

Figure 74. TiC precipitates in Ti-bearing steel at 660°C (location 2 & SEM 40000X)

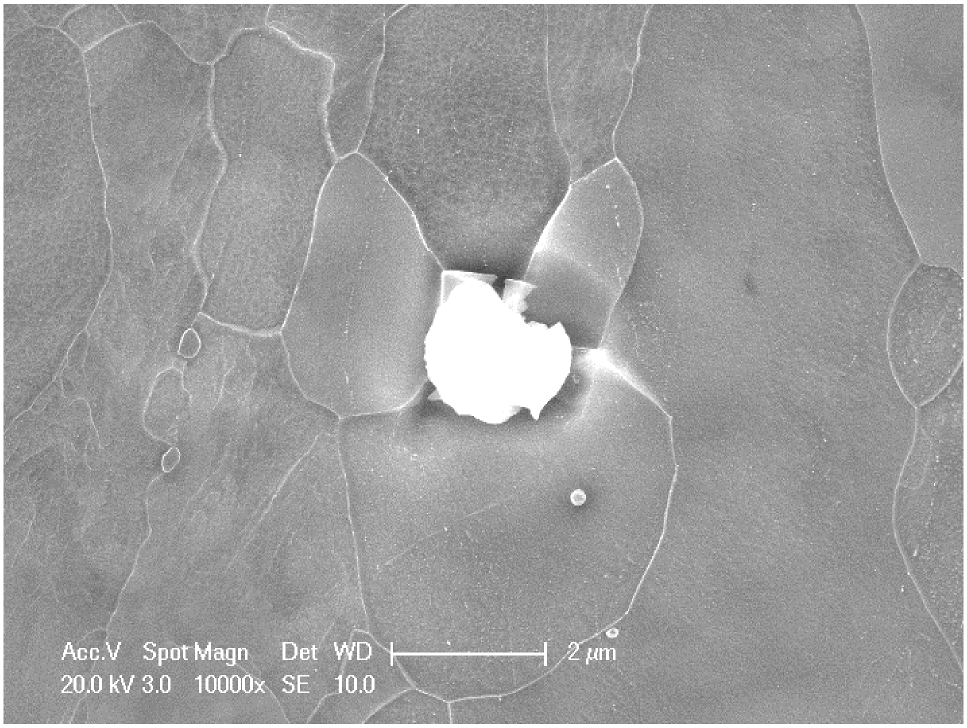

Figure 75. TiC precipitates in Ti-bearing steel at 660°C (location 3 & SEM 10000X)

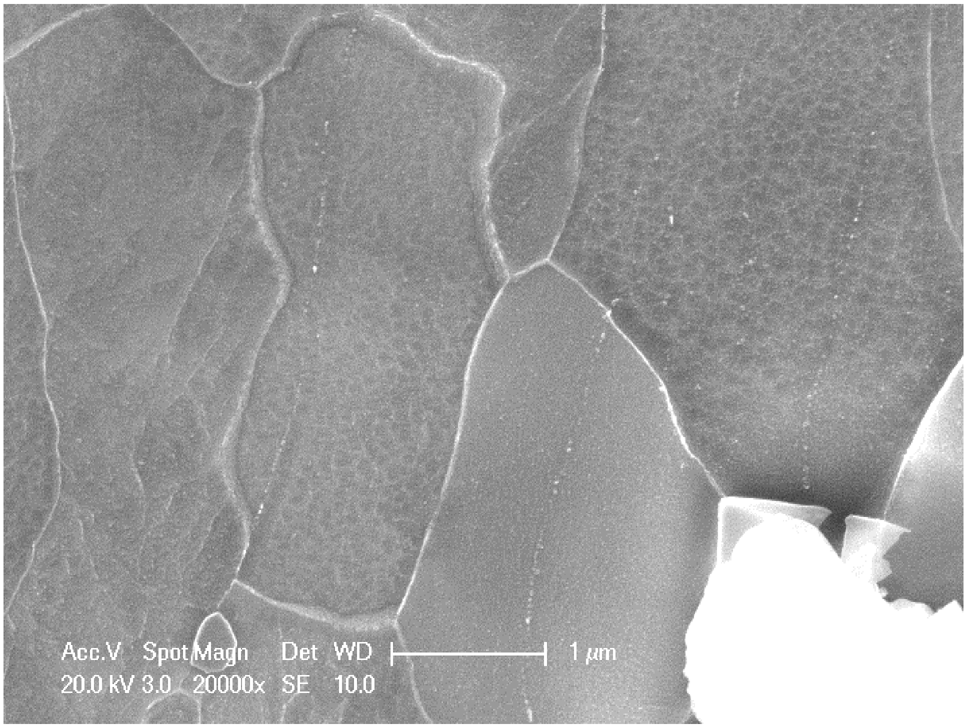

Figure 76. TiC precipitates in Ti-bearing steel at 660°C (location 3 & SEM 20000X)

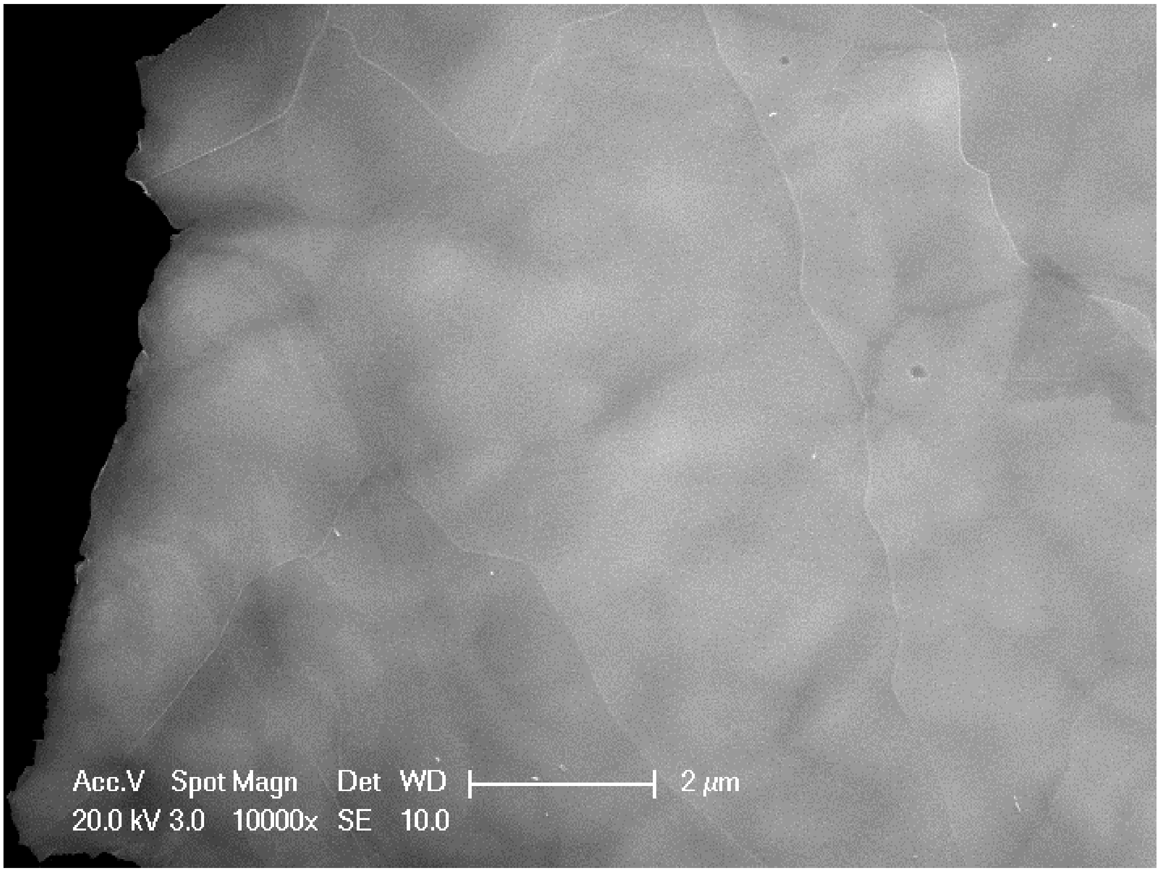

Figure 77. No TiC precipitates observed in Ti-bearing hot band steel samples (SEM 10000X)

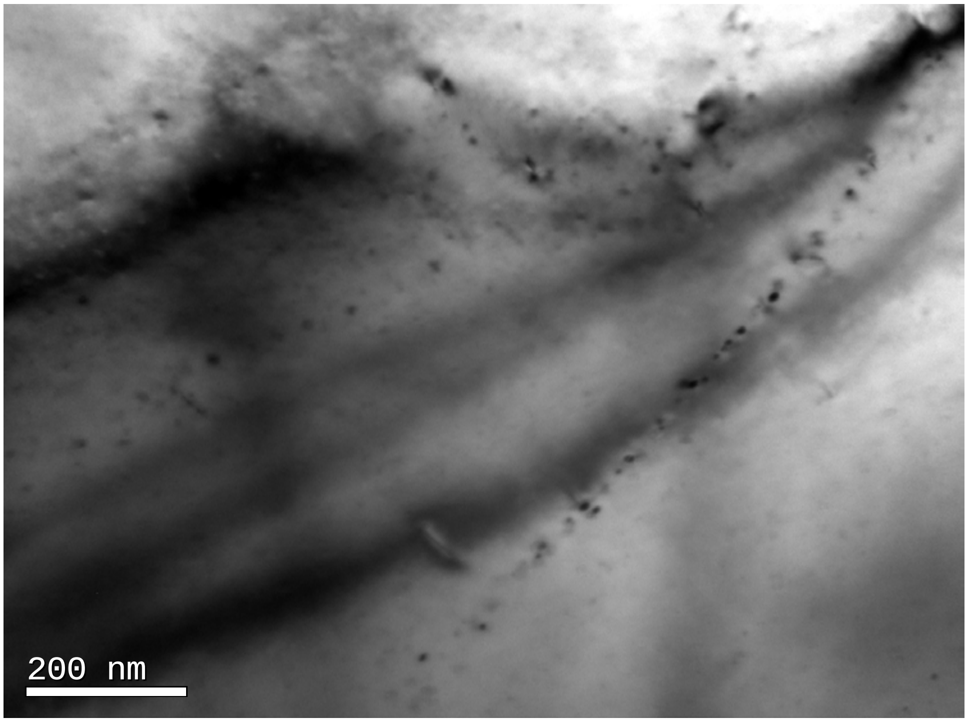

Figure 78. TiC precipitates in Ti-bearing steel at 660°C (location 1 & TEM Bright Field a)

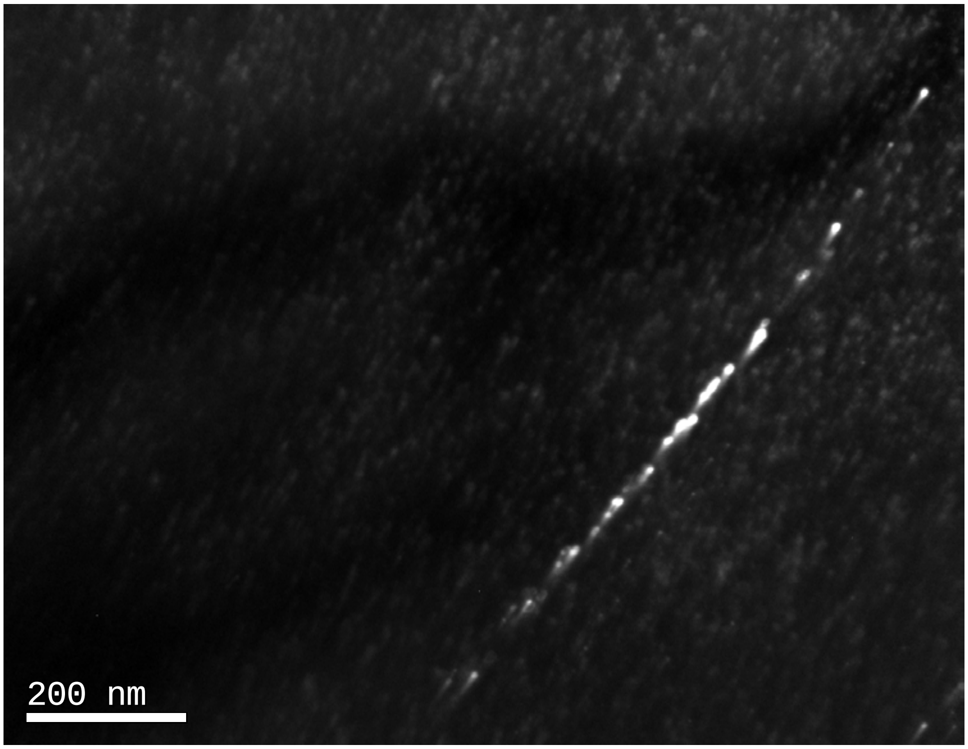

Figure 79. TiC precipitates in Ti-bearing steel at 660°C (location 1 & TEM Dark Field a)

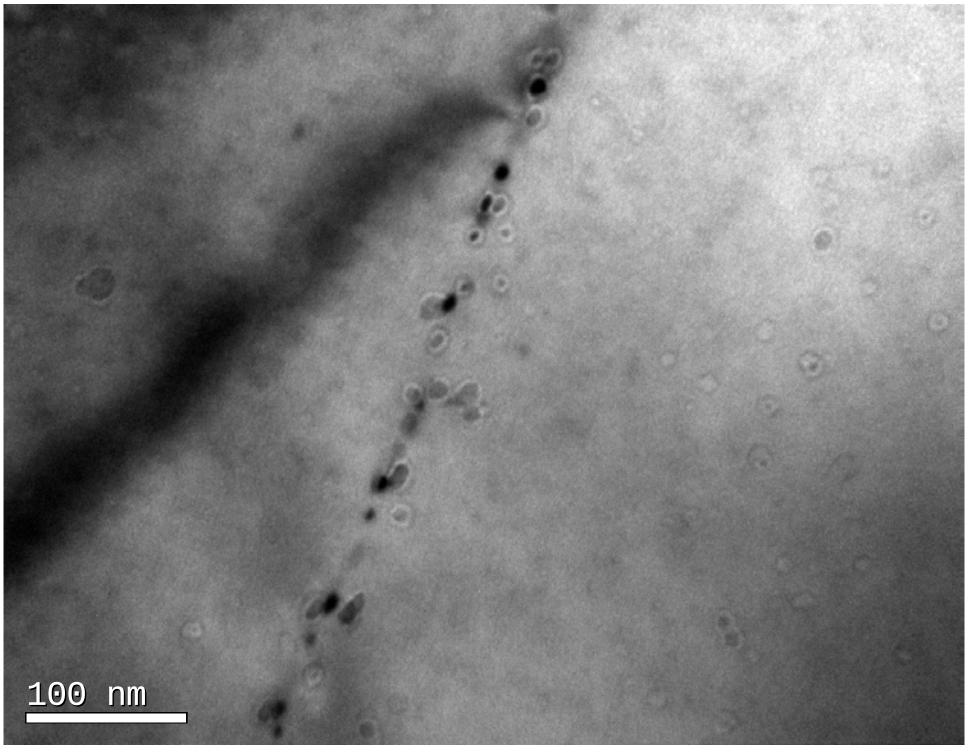

Figure 80. TiC precipitates in Ti-bearing steel at 660°C (location 1 & TEM Bright Field b)

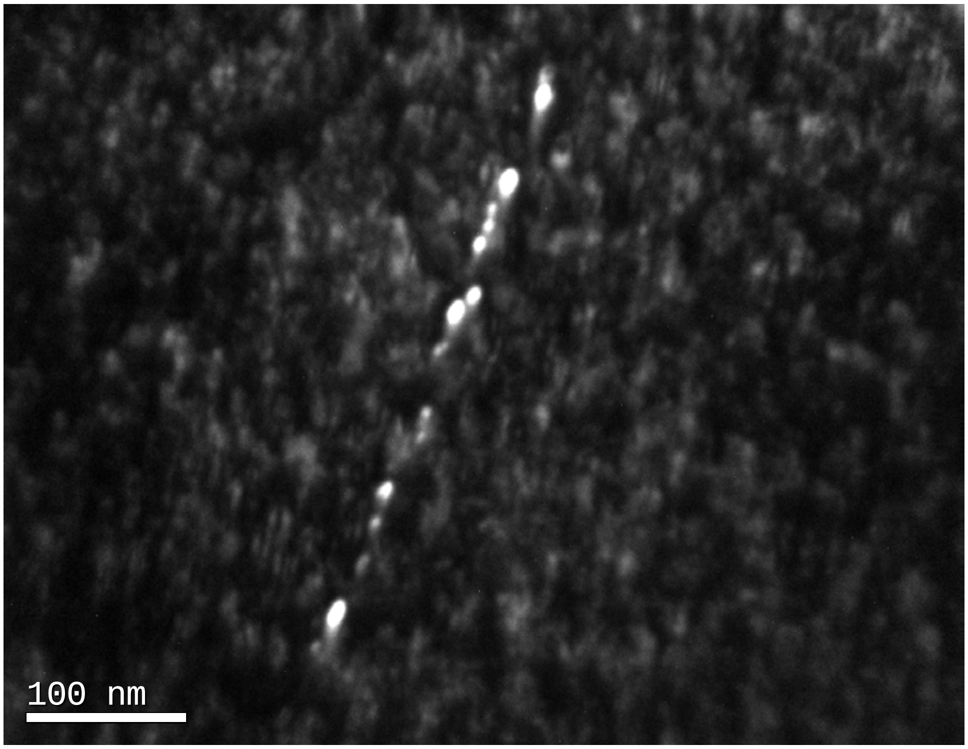

Figure 81. TiC precipitates in Ti-bearing steel at 660°C (location 1 & TEM Dark Field b)

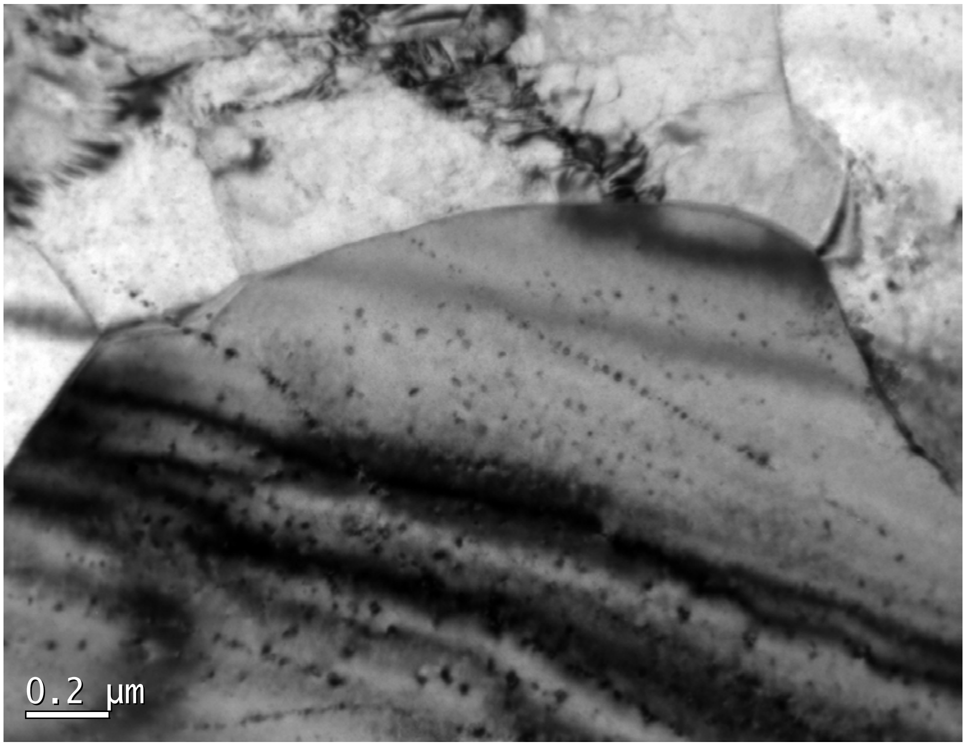

Figure 82. TiC precipitates in Ti-bearing steel at 660°C (location 2 & TEM Bright Field a)

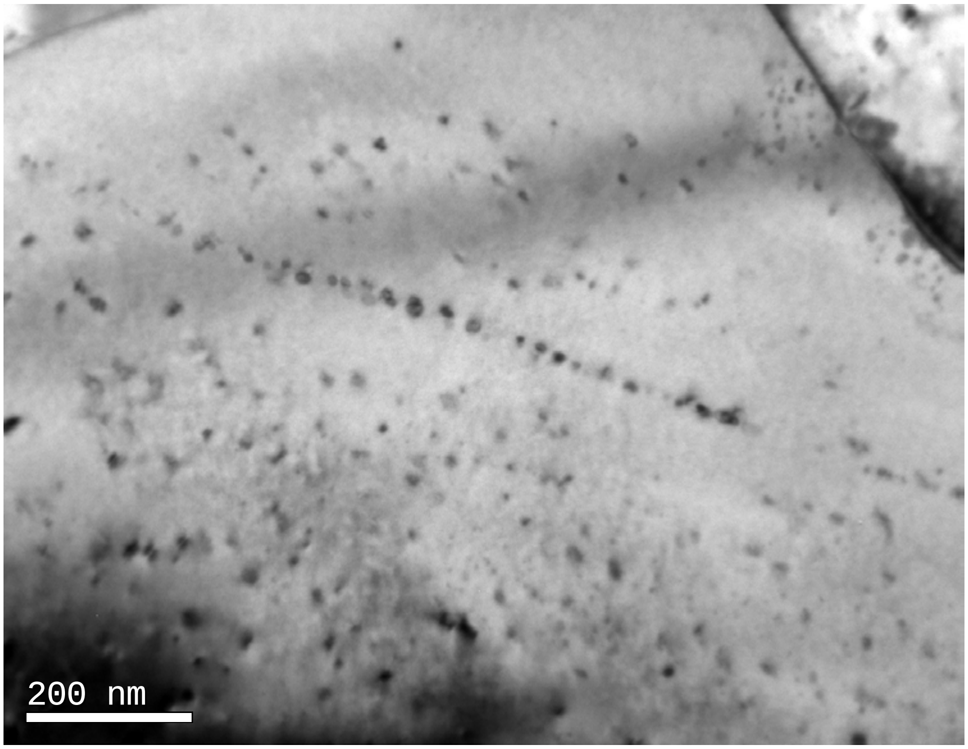

Figure 83. TiC precipitates in Ti-bearing steel at 660°C (location 2 & TEM Bright Field b)

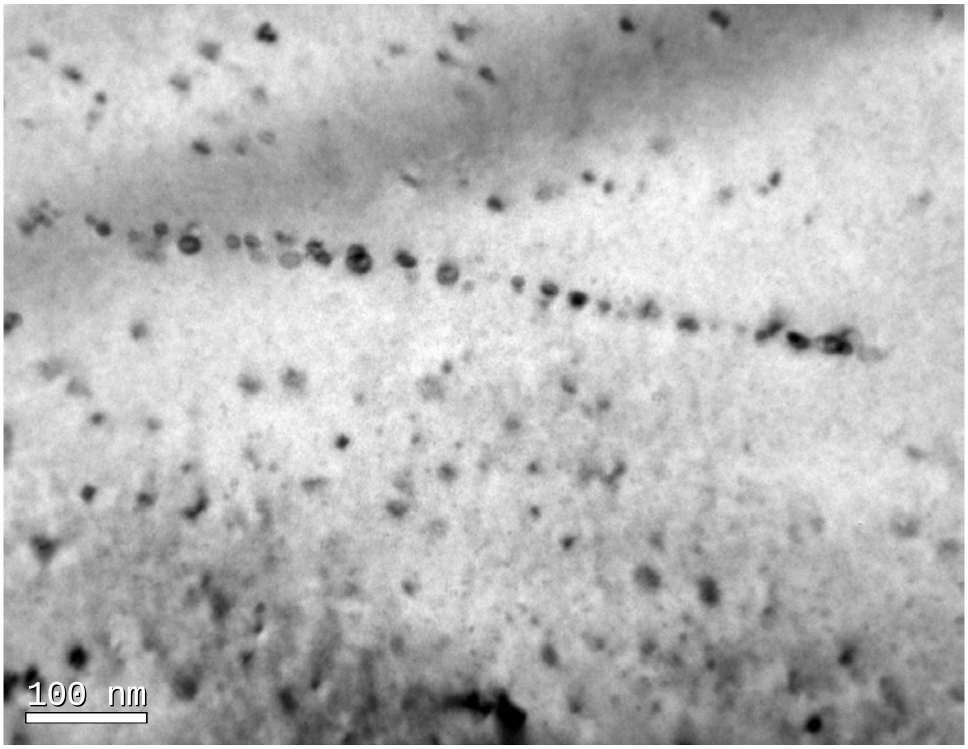

Figure 84. TiC precipitates in Ti-bearing steel at 660°C (location 2 & TEM Bright Field c)

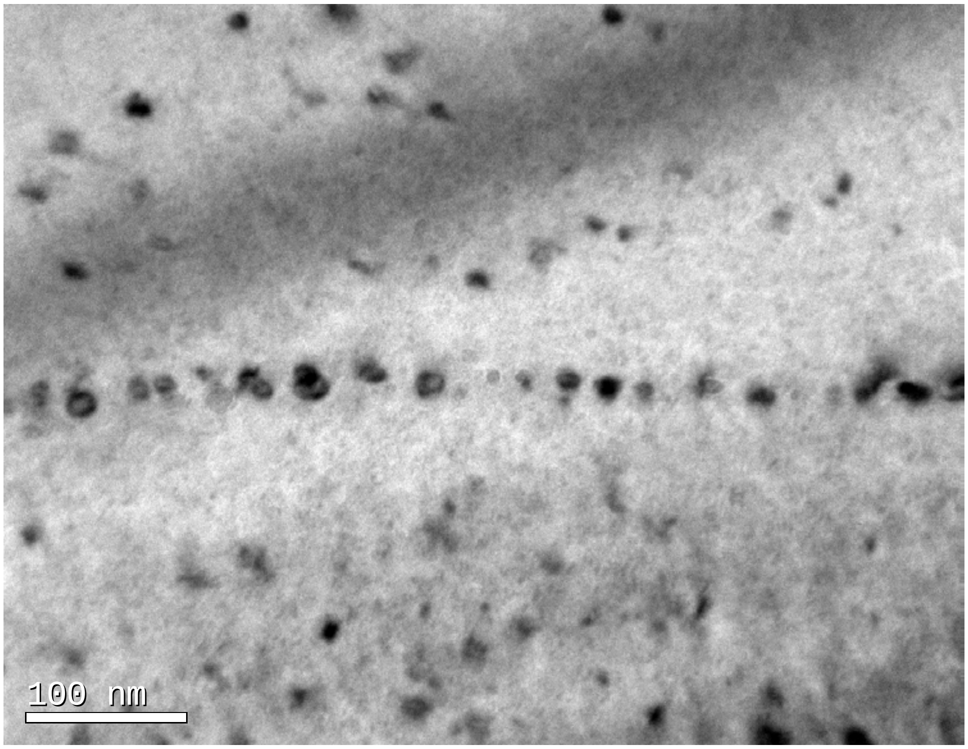

Figure 85. TiC precipitates in Ti-bearing steel at 660°C (location 2 & TEM Bright Field d)

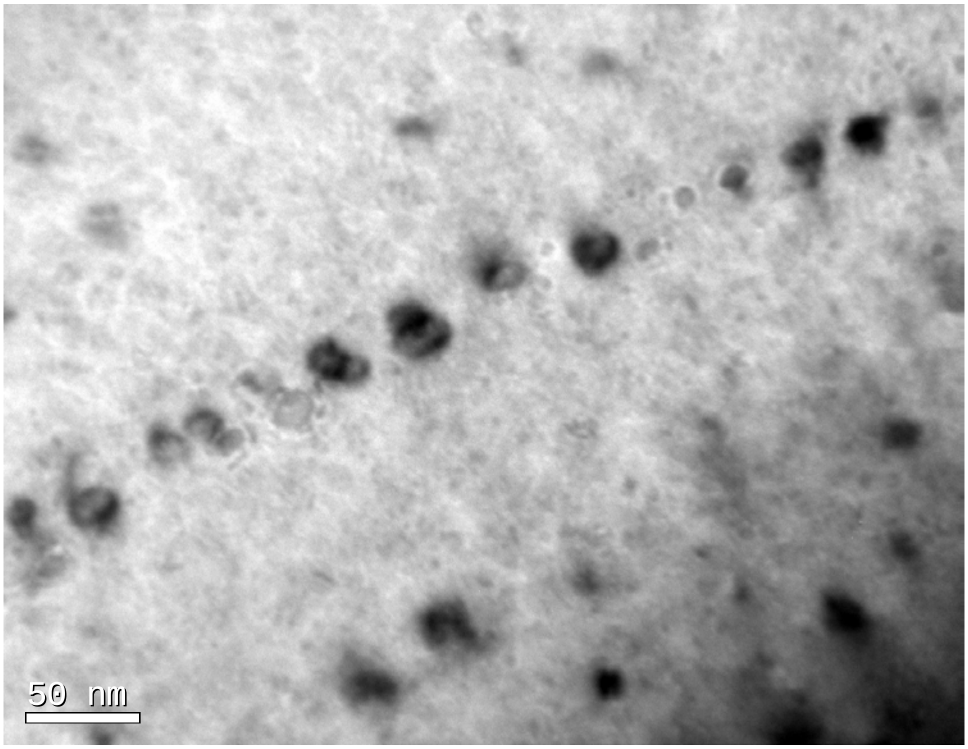

Figure 86. TiC precipitates in Ti-bearing steel at 660°C (location 2 & TEM Bright Field e)

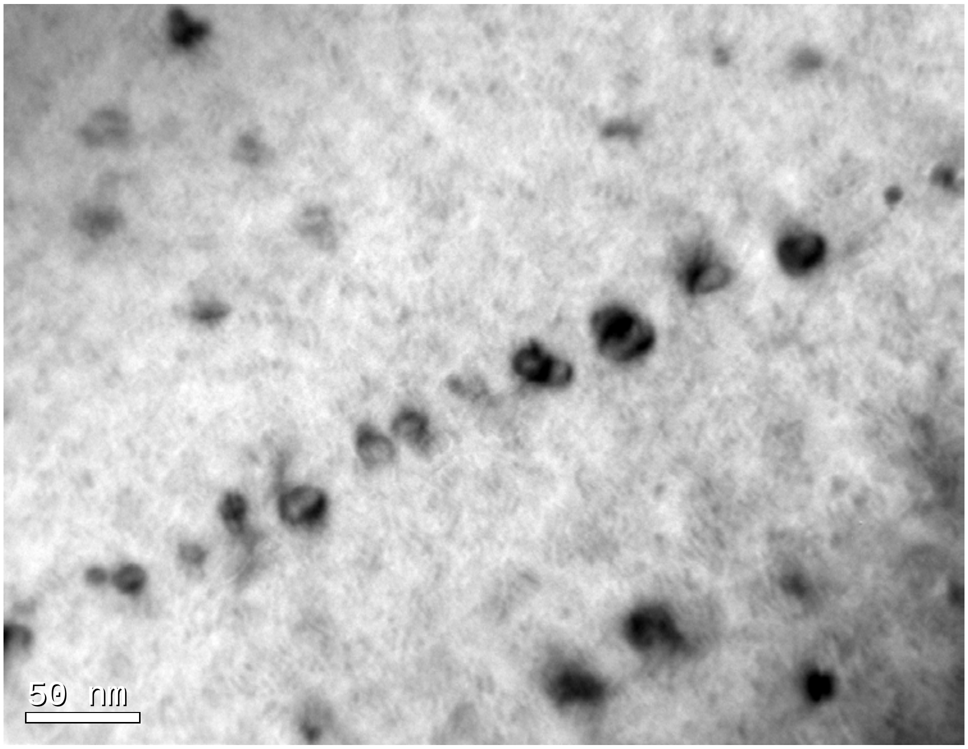

Figure 87. TiC precipitates in Ti-bearing steel at 660°C (location 2 & TEM Bright Field f)

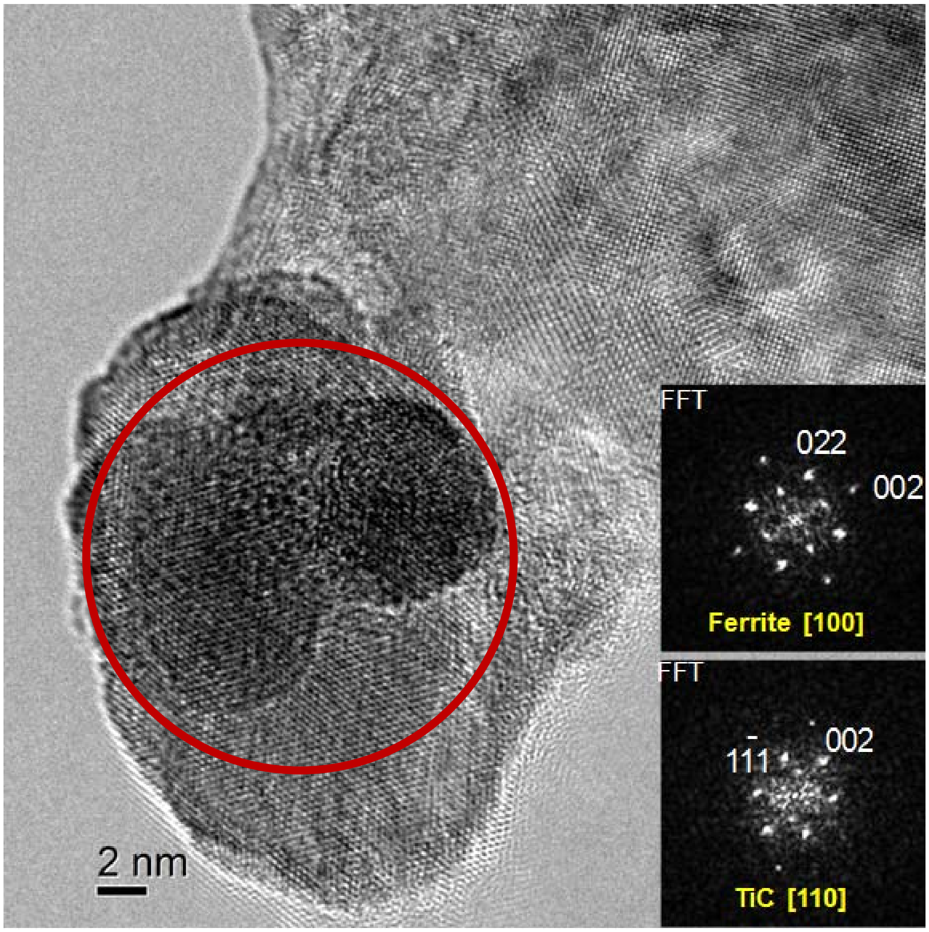

Figure 88. TiC precipitates (circled) in Ti-bearing steel at 660°C (location 1 & HRTEM Bright Field Image and Fast Fourier transformation analysis showing that the orientation relationship between the TiC precipitates and the Ferrite Matrix follows Kurdjumov-Sachs orientation relationship)

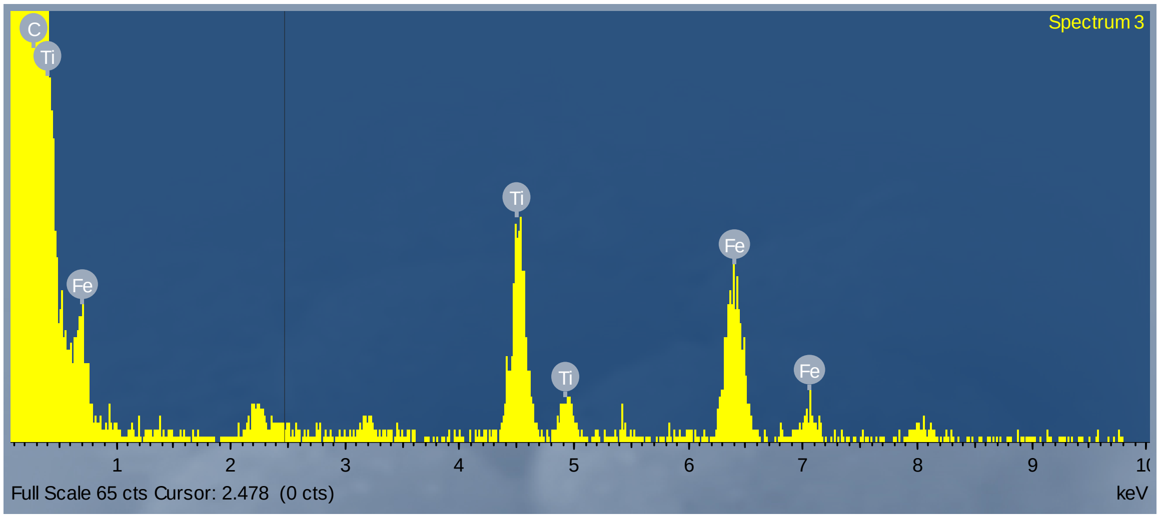

Figure 89. TiC precipitates in Ti-bearing steel at 660°C (location 1 & EDS)

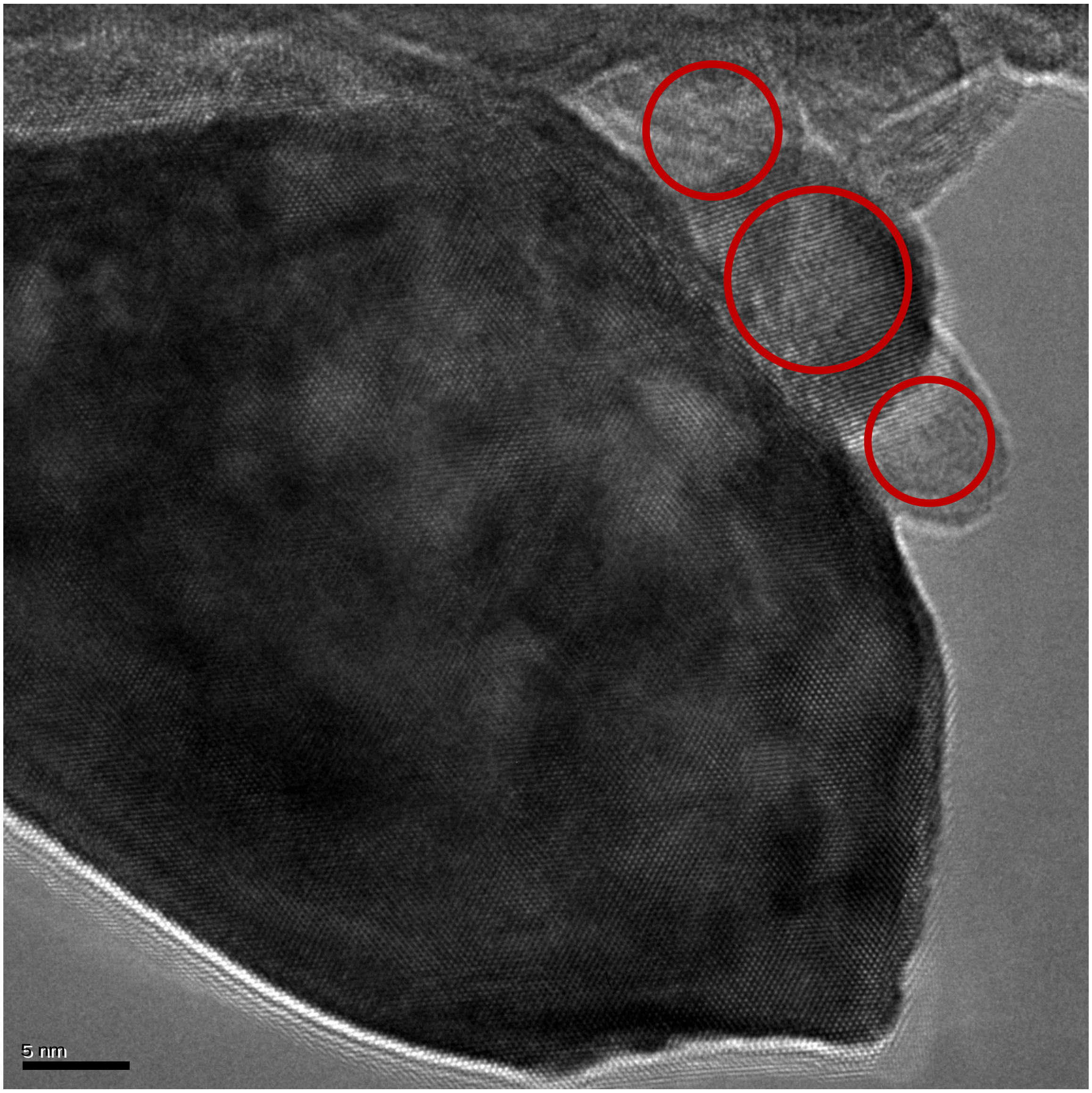

Figure 90. TiC precipitates (circled) in Ti-bearing steel at 660°C (location 2 & HRTEM Bright Field Image a)

Figure 91. TiC precipitates (circled) in Ti-bearing steel at 660°C (location 2 & HRTEM Bright Field Image b)

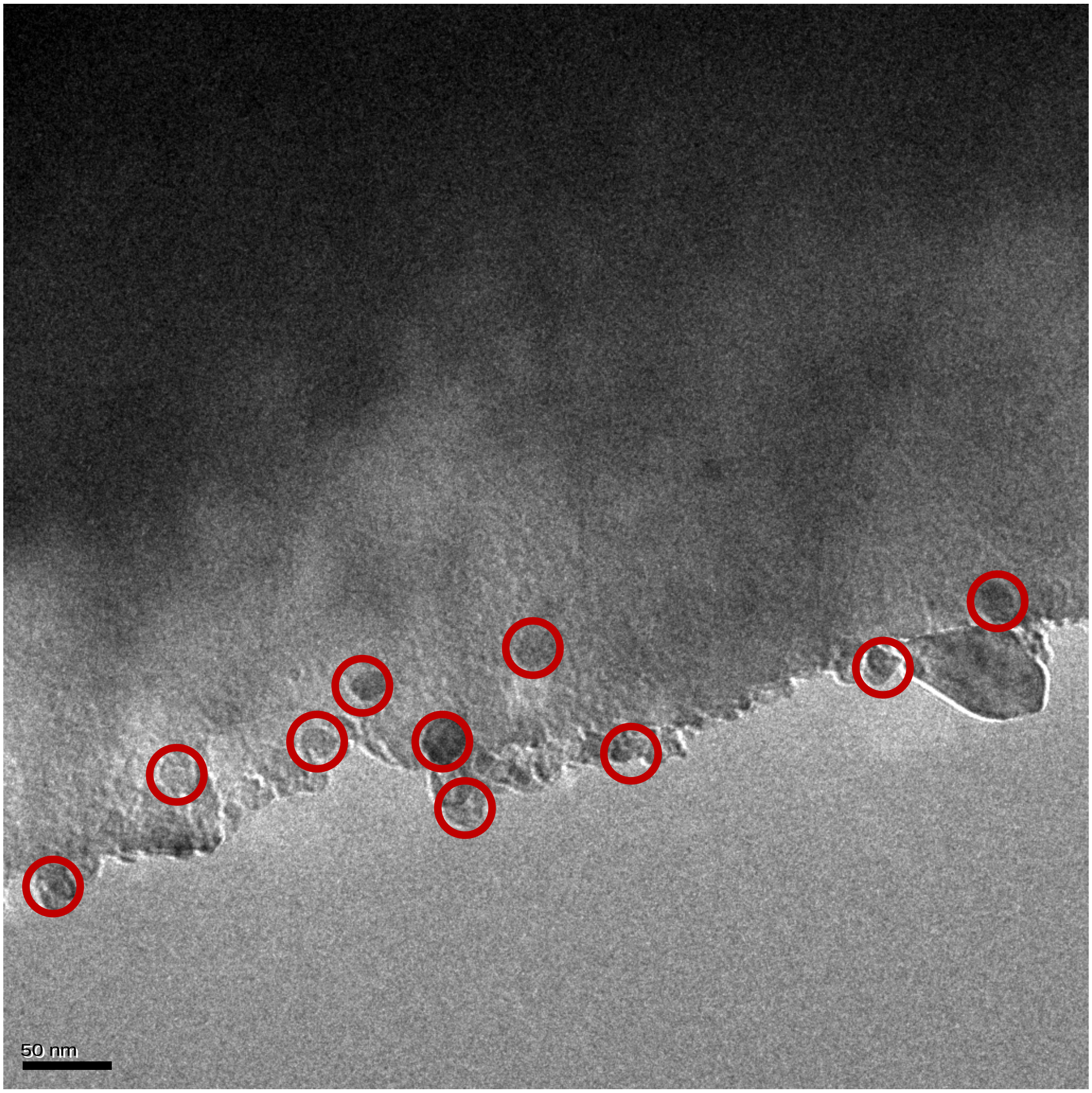

Figure 92. TiC precipitates (circled) in Ti-bearing steel at 660°C (location 2 & HRTEM Bright Field Image c)

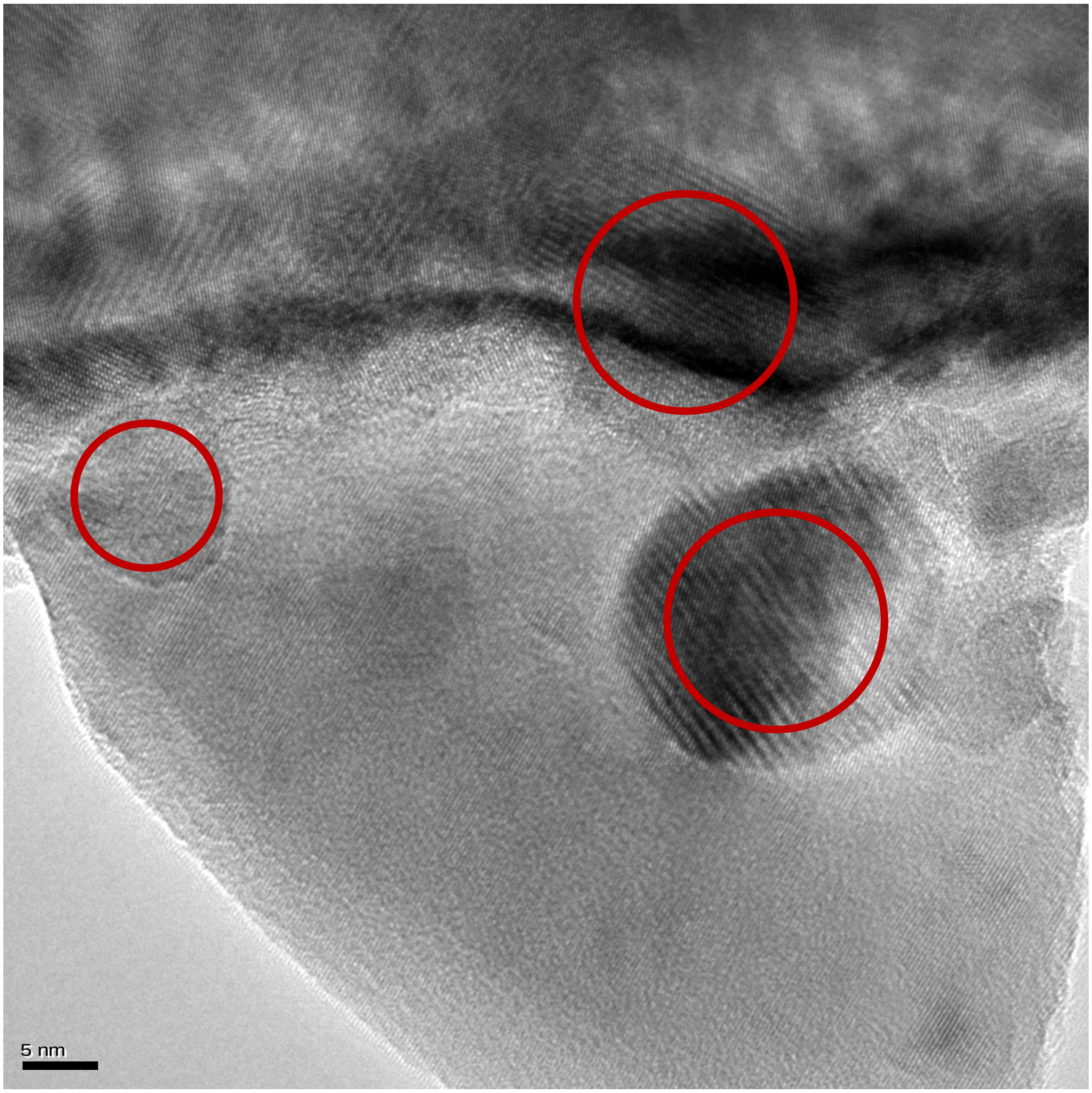

Figure 93. TiC precipitates (circled) in Ti-bearing steel at 660°C (location 2 & HRTEM Bright Field Image d)

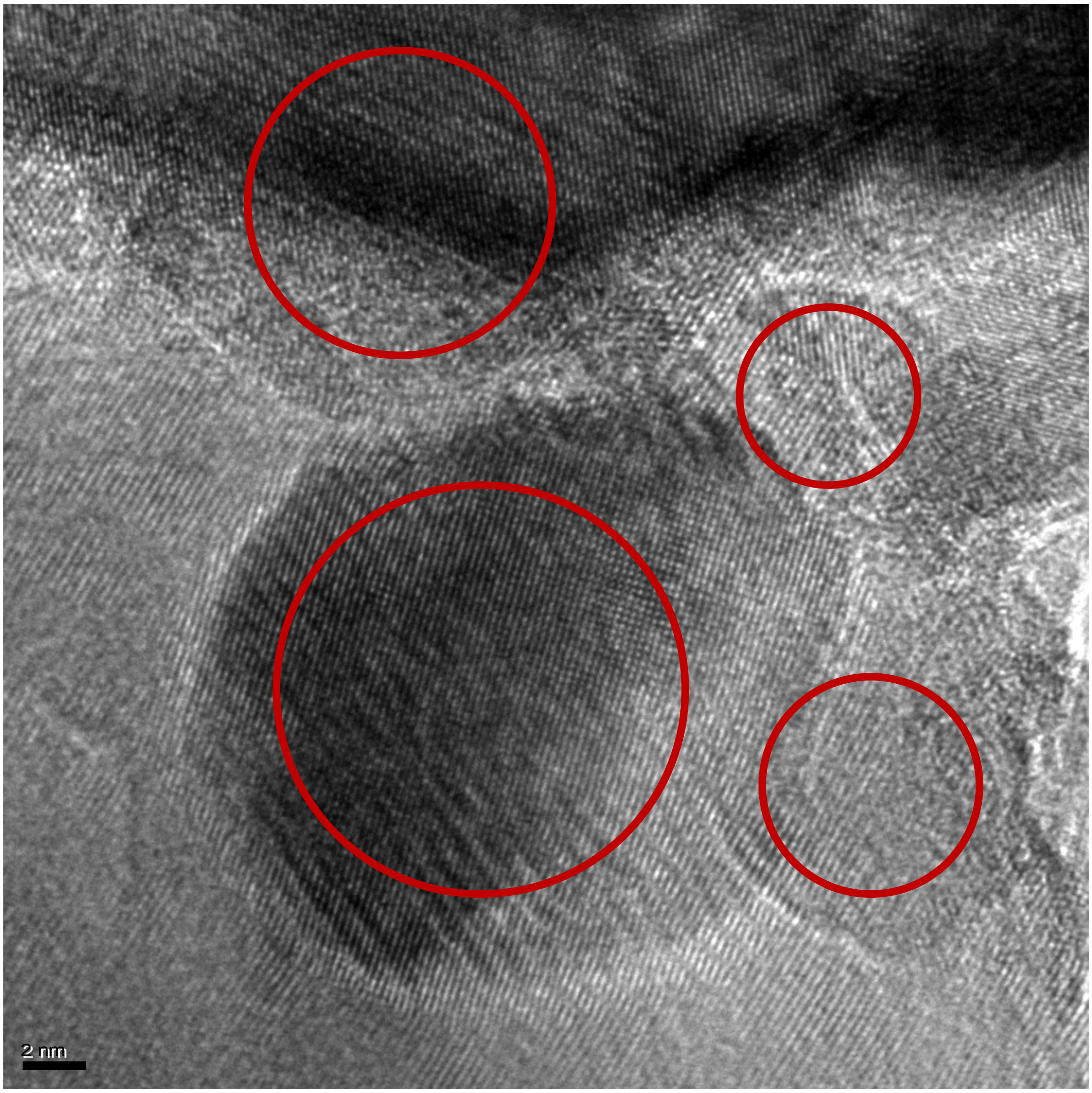

Figure 94. TiC precipitates (circled) in Ti-bearing steel at 660°C (location 2 & HRTEM Bright Field Image e)

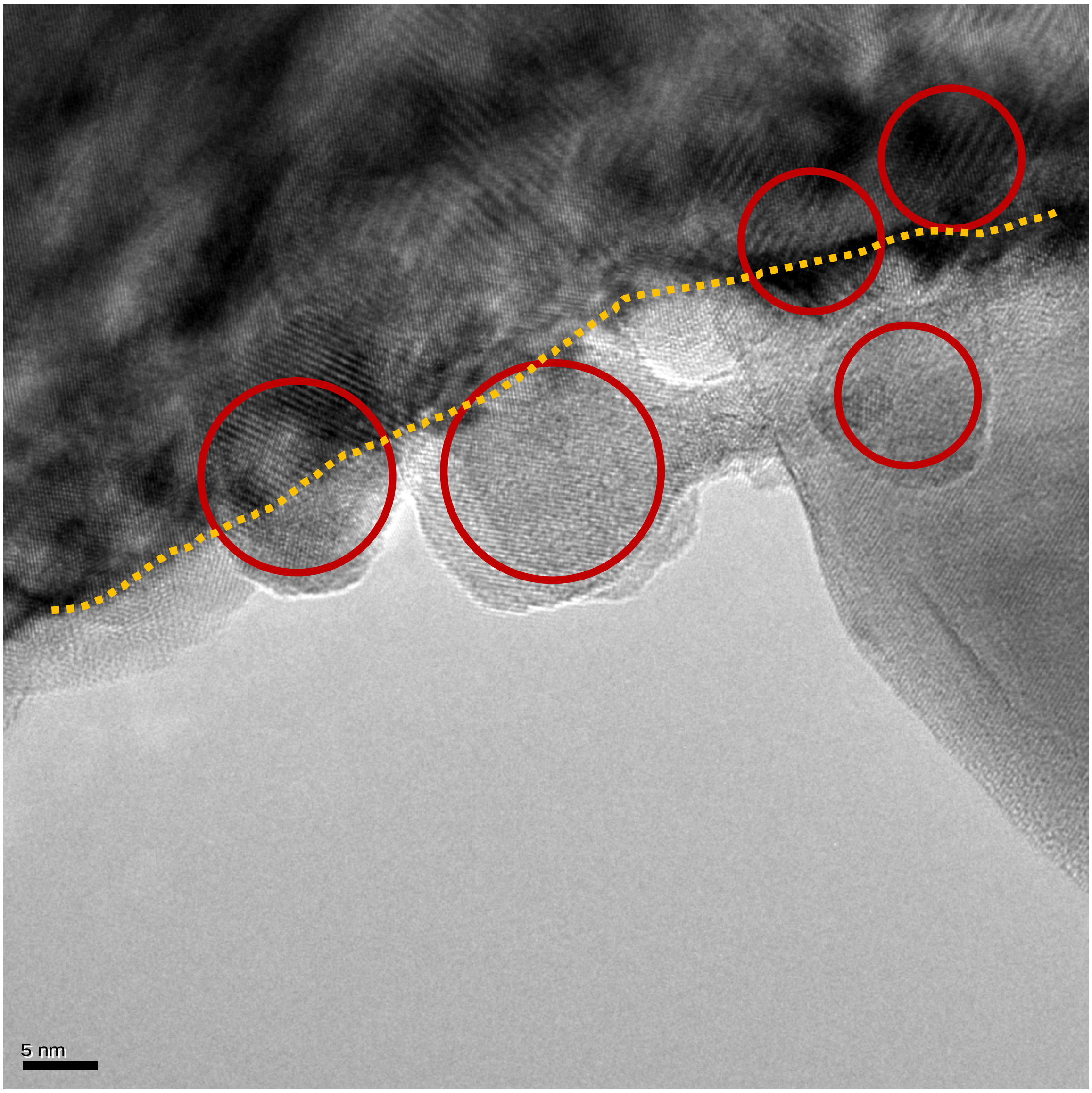

Figure 95. TiC precipitates (circled) along the grain boundary (dashed line) in Ti-bearing steel at 660°C (location 2 & HRTEM Bright Field Image f)

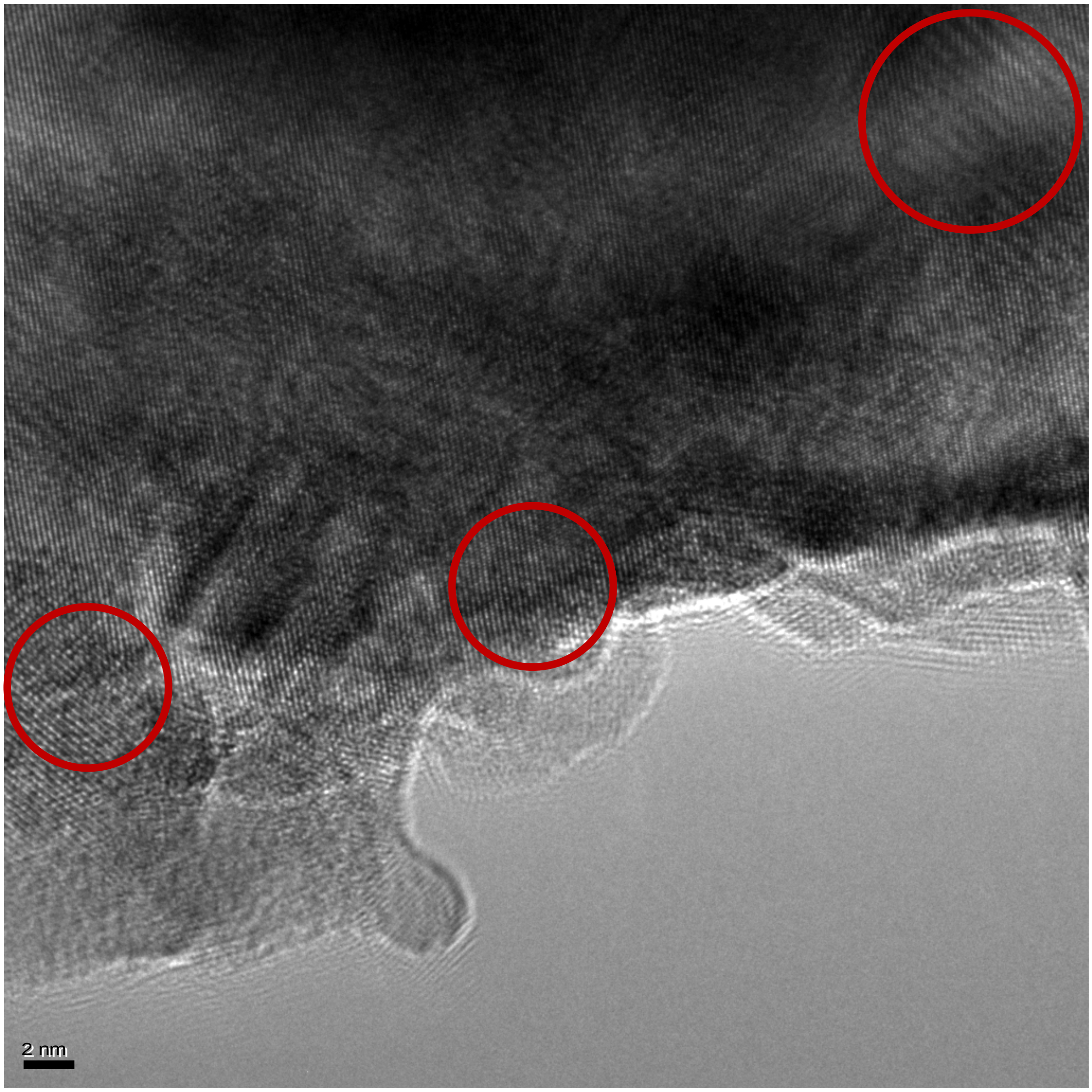

Figure 96. TiC precipitates (circled) in Ti-bearing steel at 660°C (location 2 & HRTEM Bright Field Image g)

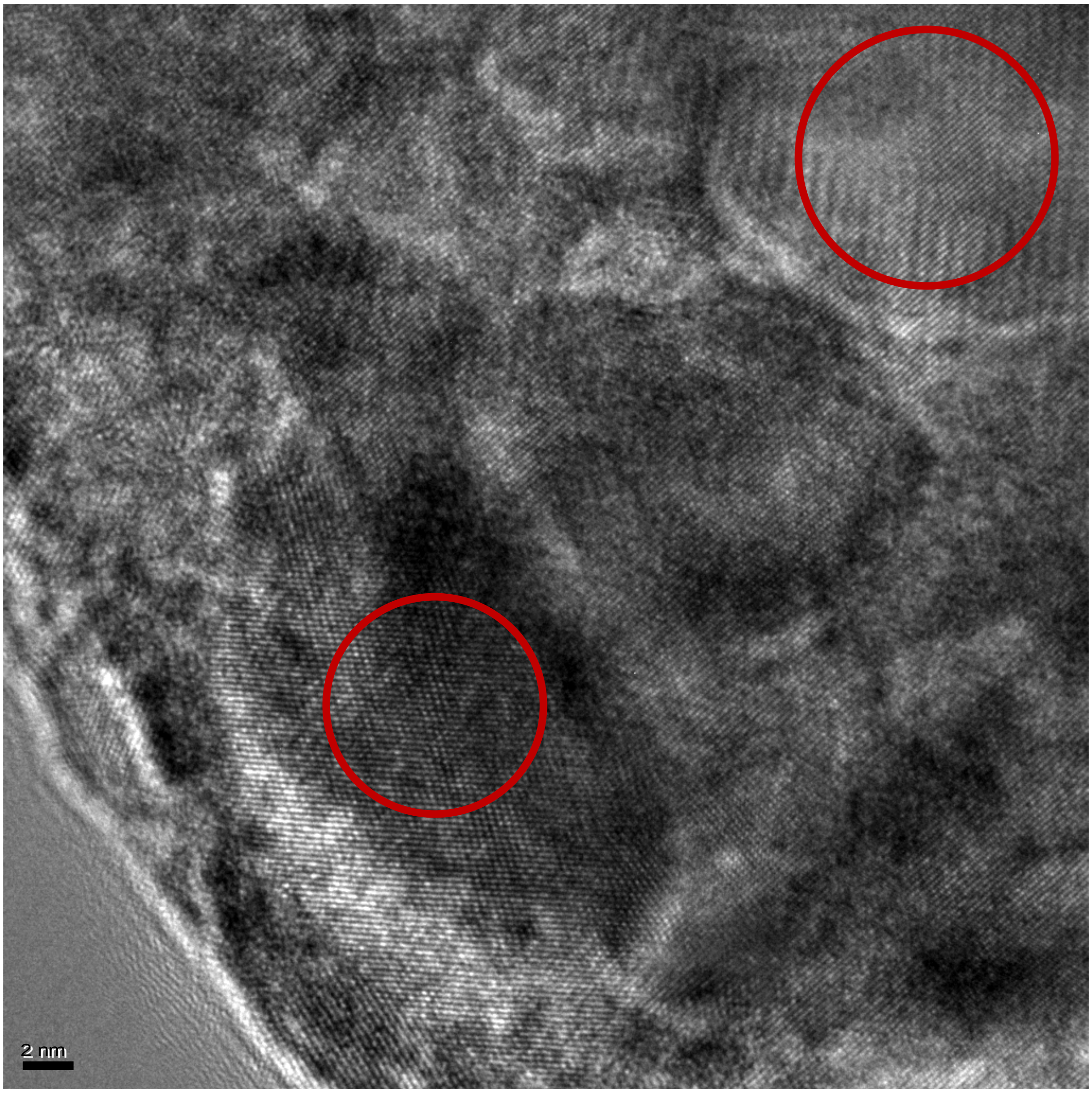

Figure 97. TiC precipitates (circled) in Ti-bearing steel at 660°C (location 2 & HRTEM Bright Field Image h)

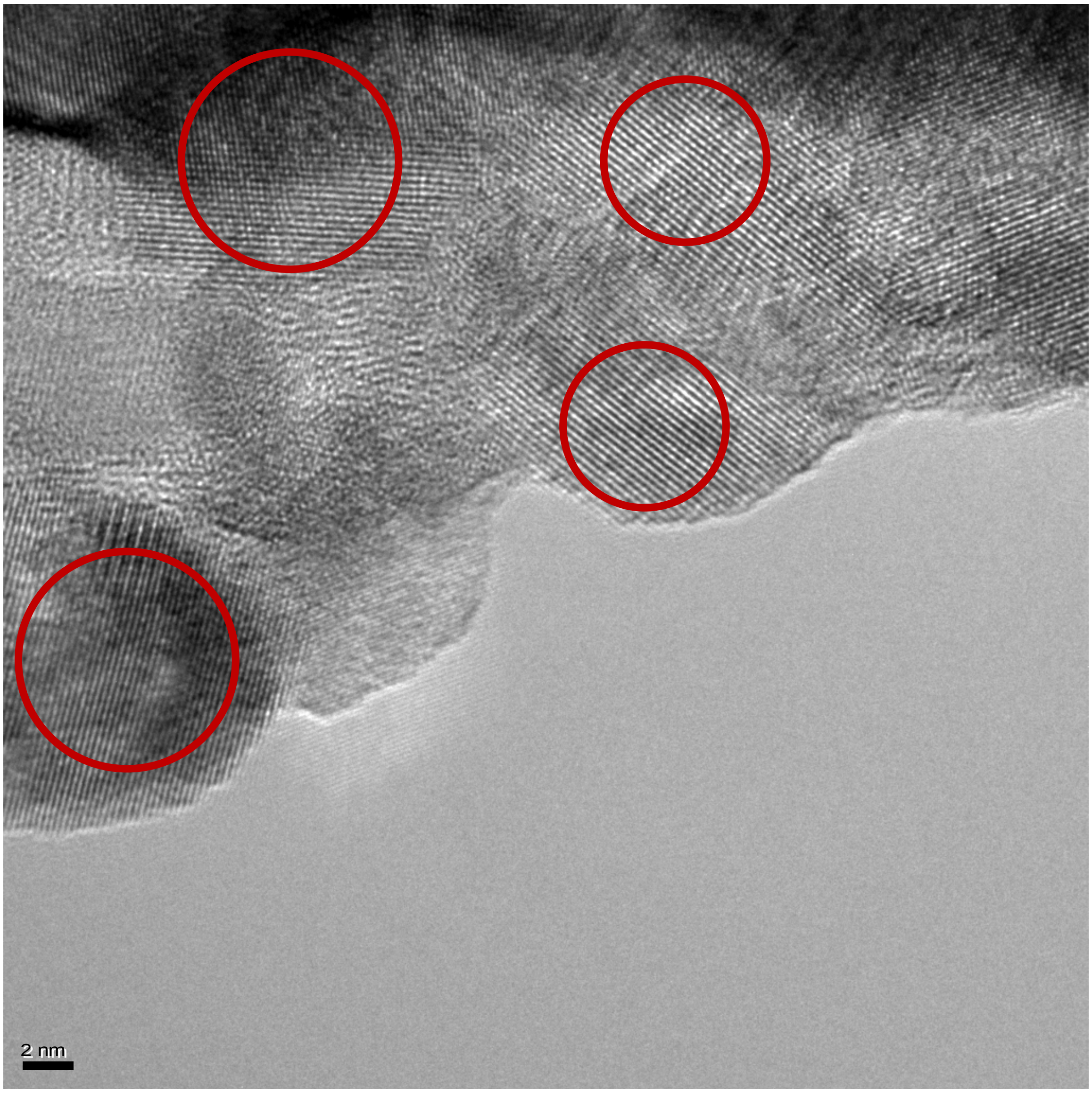

Figure 98. TiC precipitates (circled) in Ti-bearing steel at 660°C (location 2 & HRTEM Bright Field Image i)

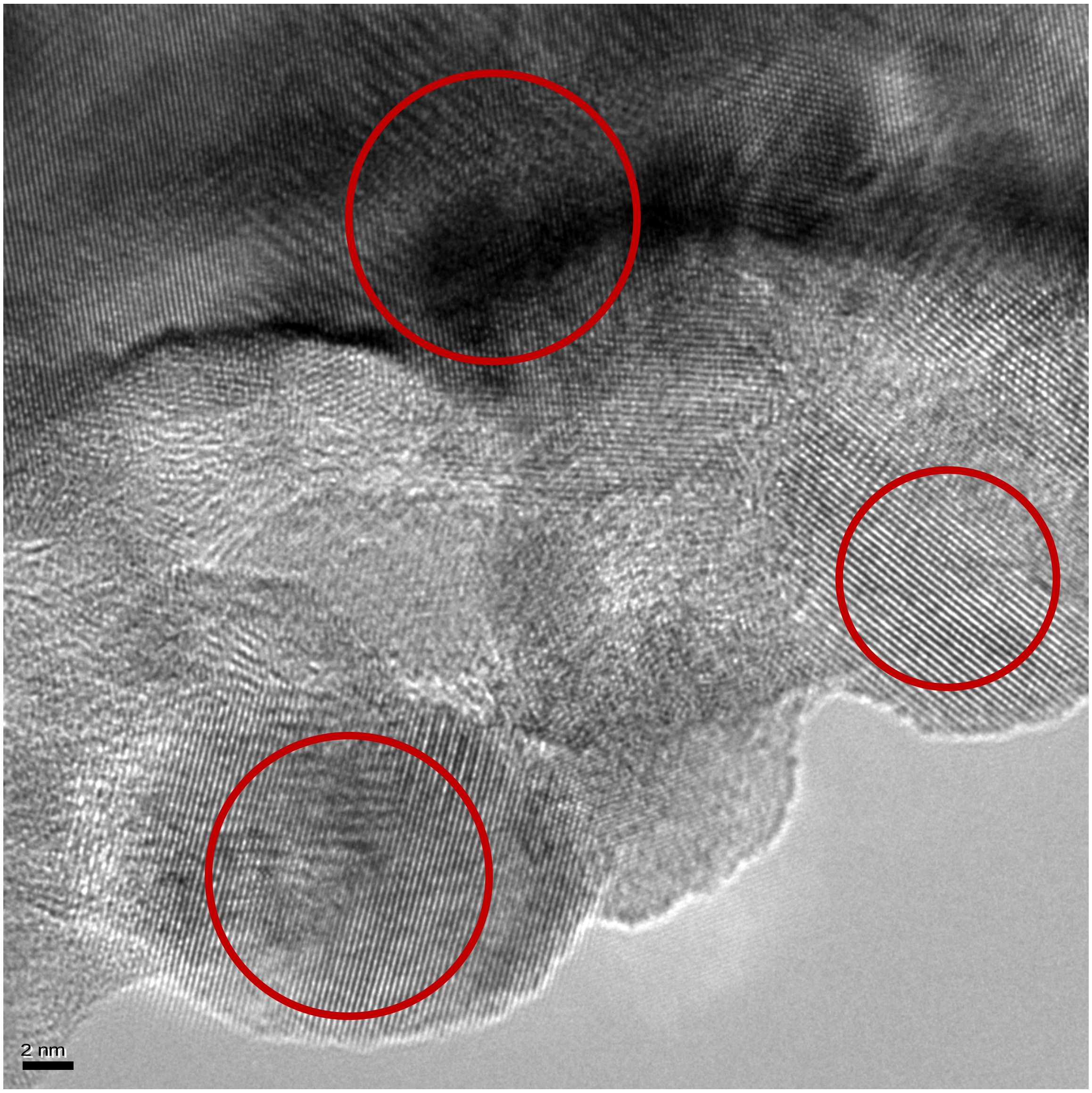

Figure 99. TiC precipitates (circled) in Ti-bearing steel at 660°C (location 2 & HRTEM Bright Field Image j)

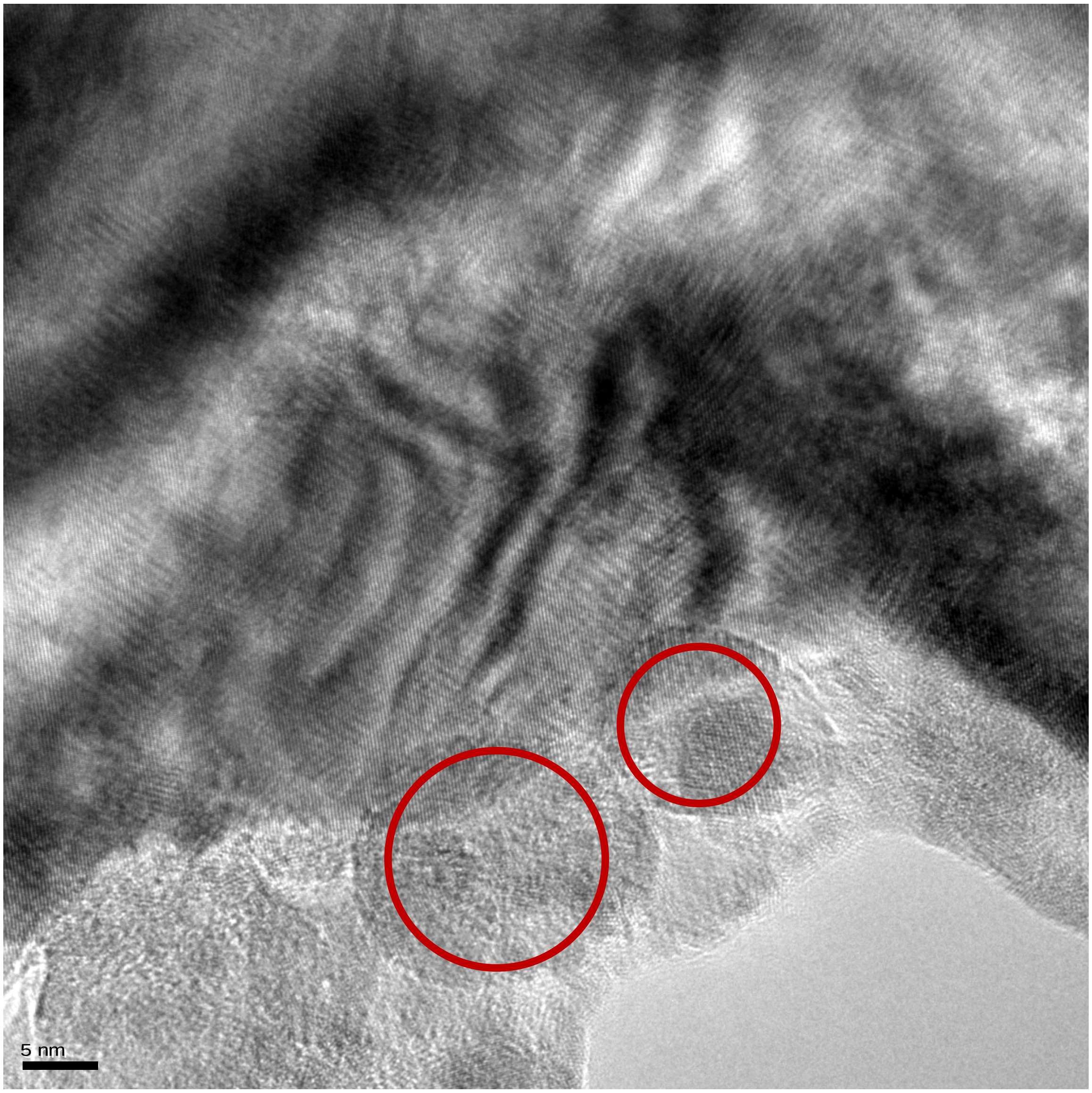

Figure 100. TiC precipitates (circled) in Ti-bearing steel at 660°C (location 2 & HRTEM Bright Field Image k)

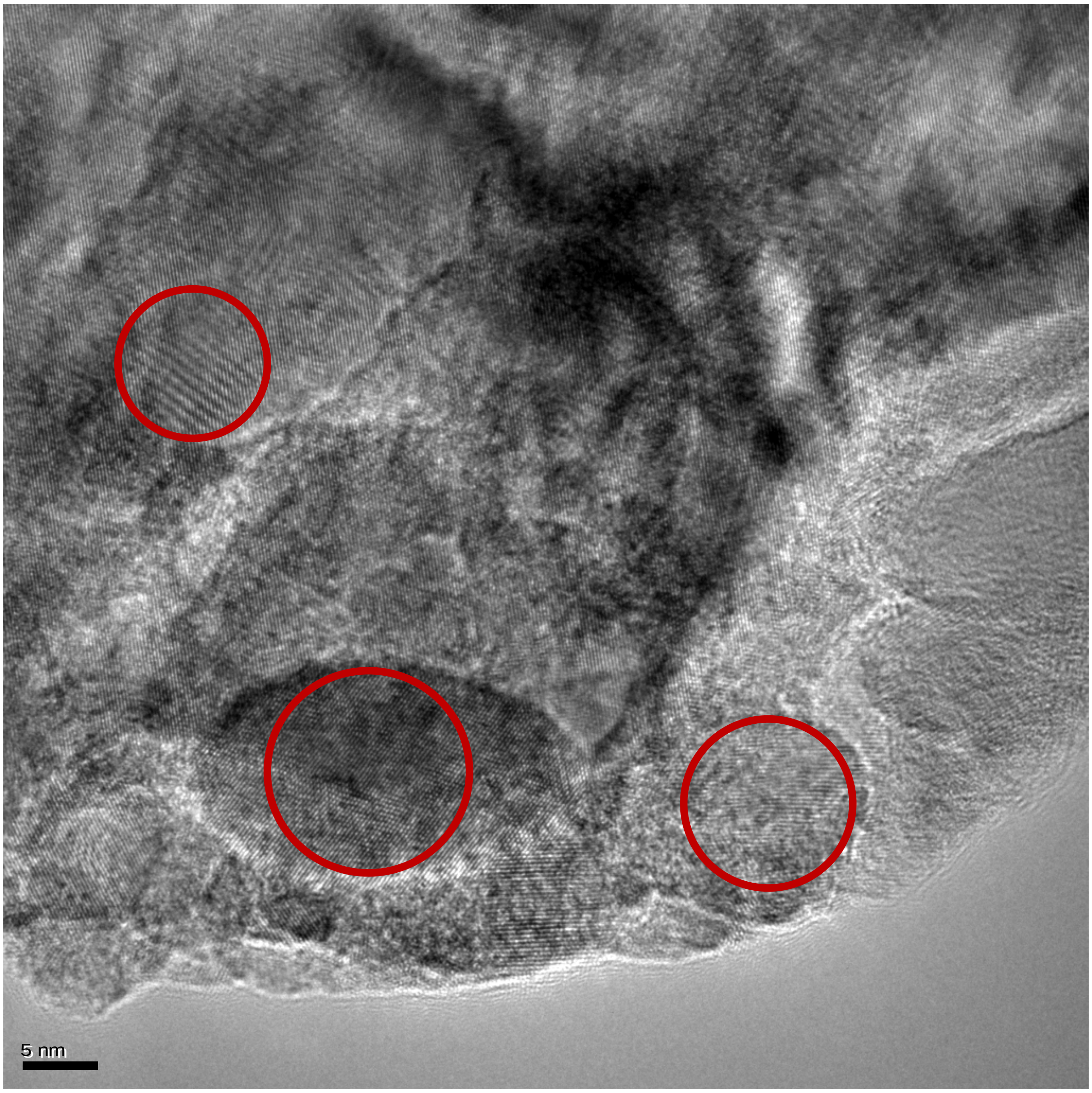

Figure 101. TiC precipitates (circled) in Ti-bearing steel at 660°C (location 2 & HRTEM Bright Field Image l)

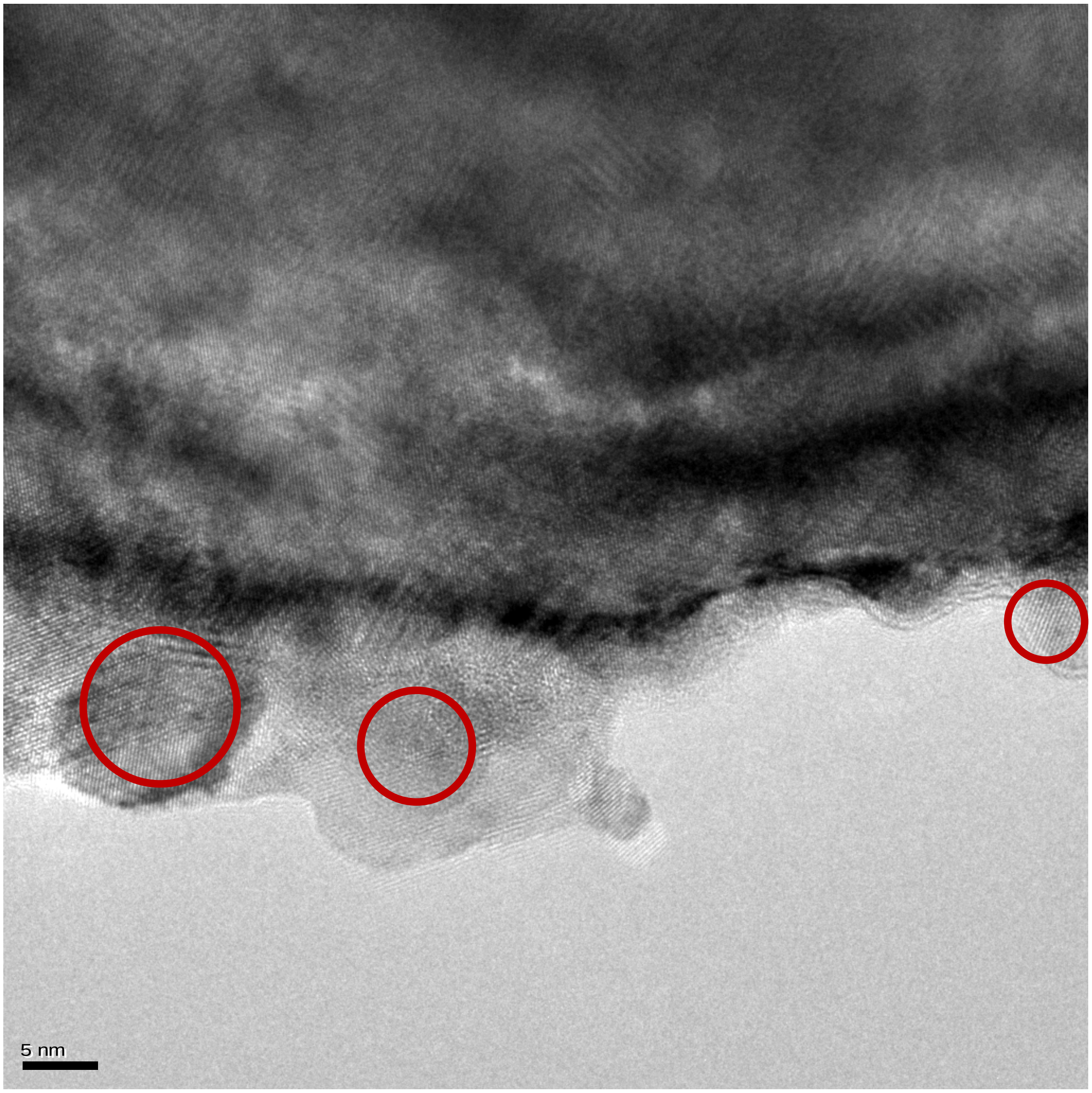

Figure 102. TiC precipitates (circled) in Ti-bearing steel at 660°C (location 2 & HRTEM Bright Field Image m)

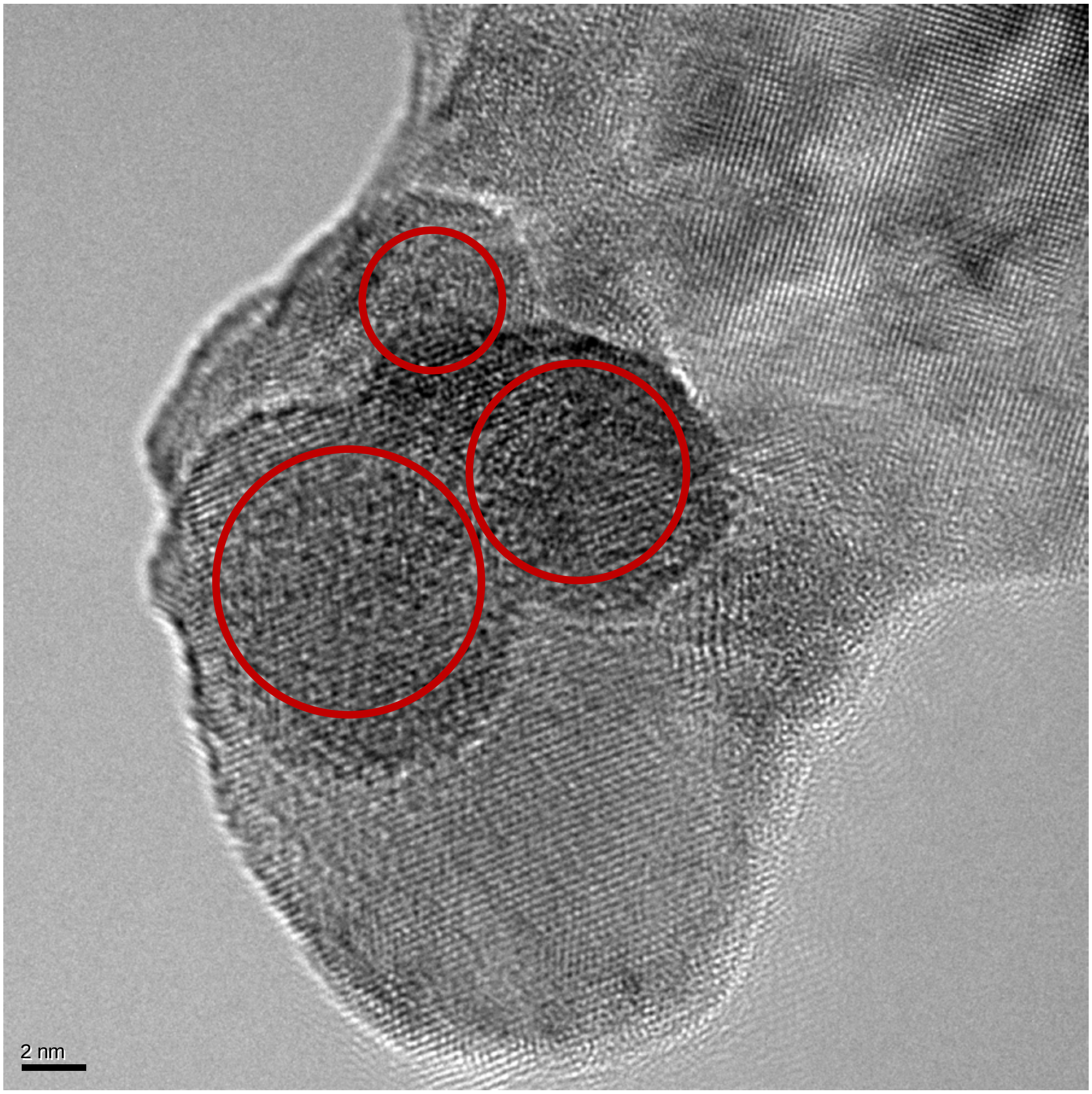

Figure 103. TiC precipitates (circled) in Ti-bearing steel at 660°C (location 2 & HRTEM Bright Field Image n)

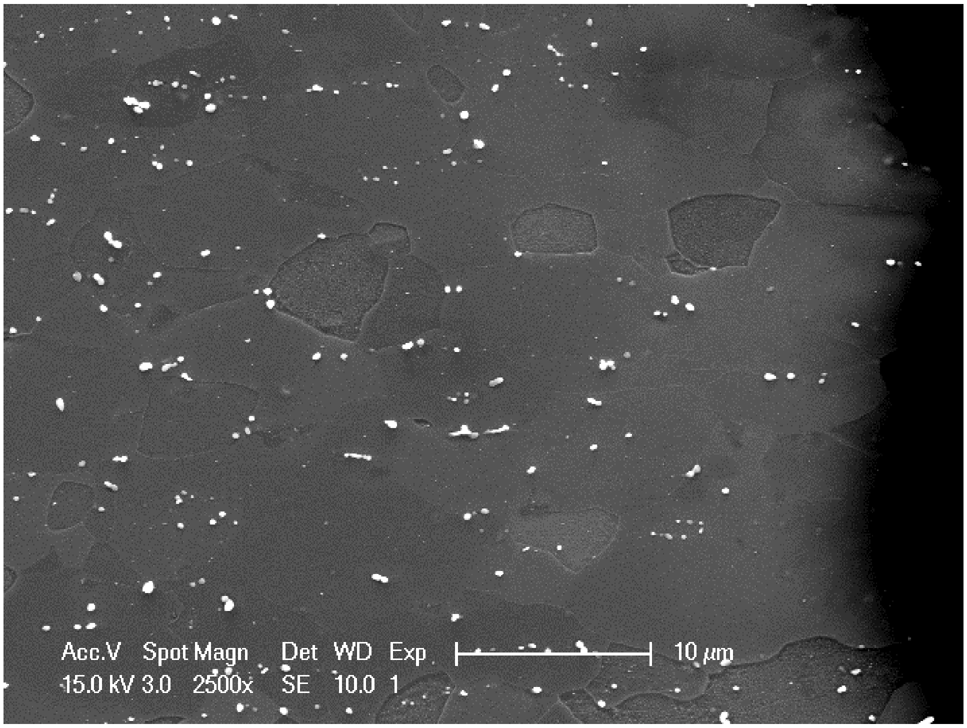

Figure 104. Cementite in Nb-bearing steel at 660°C (location 1 & SEM 2500X)

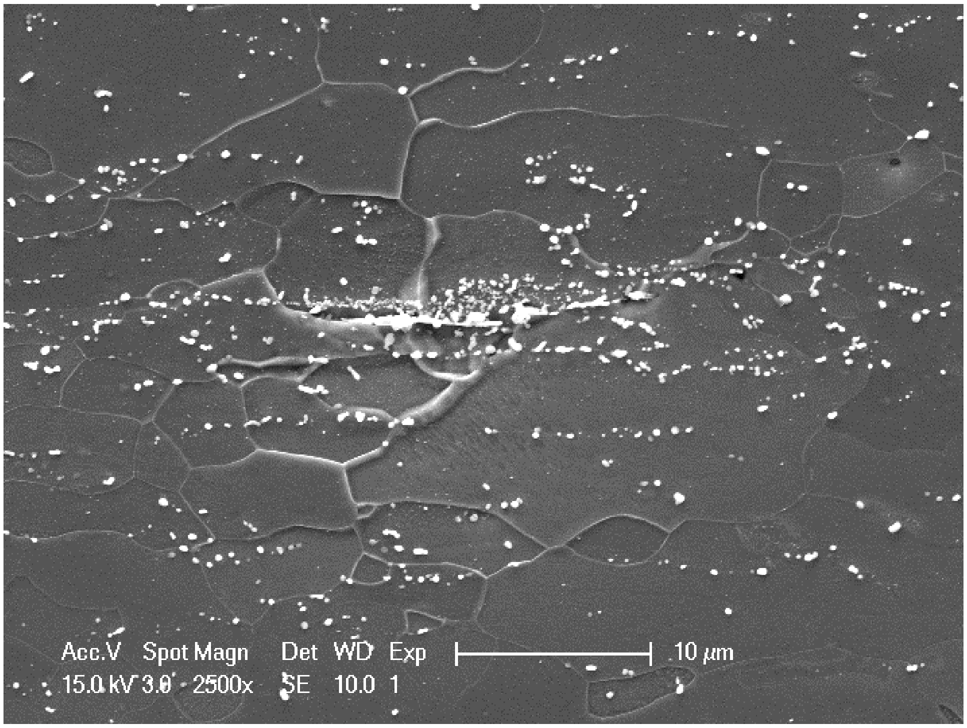

Figure 105. Cementite segregation bands in Nb-bearing steel at 660°C (location 2 & SEM 2500X)

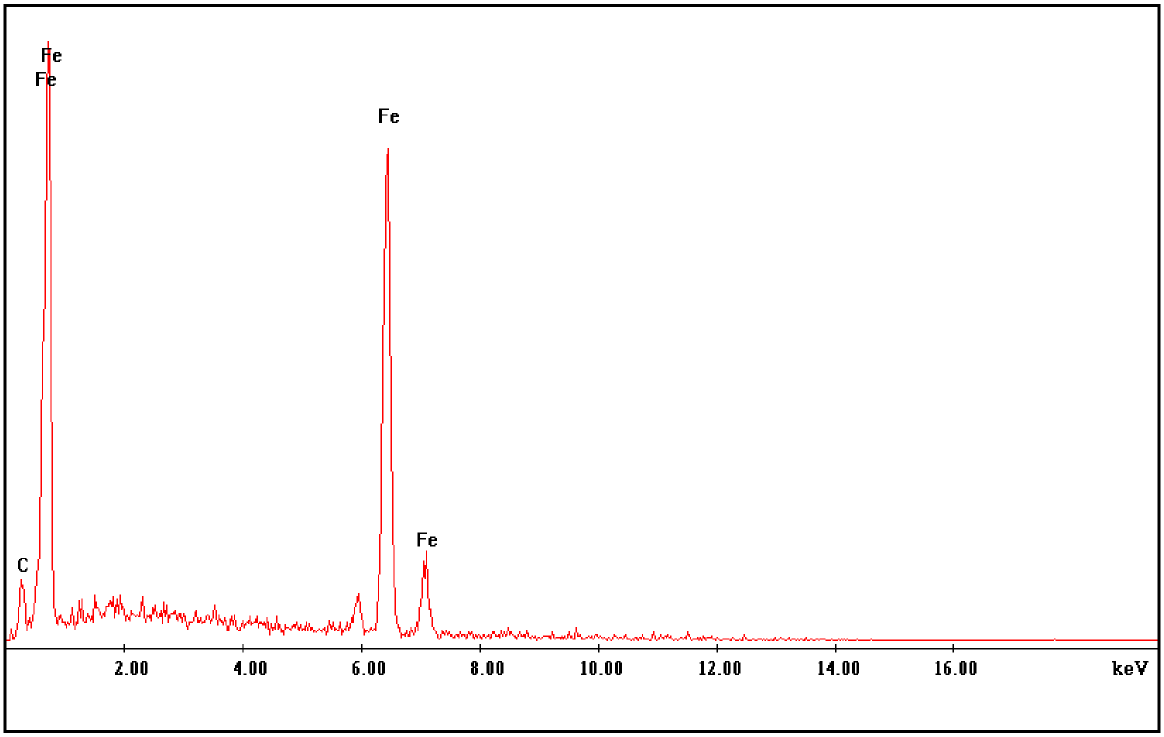

Figure 106. Cementites in Nb-bearing steel at 660°C (location 1 & EDS)

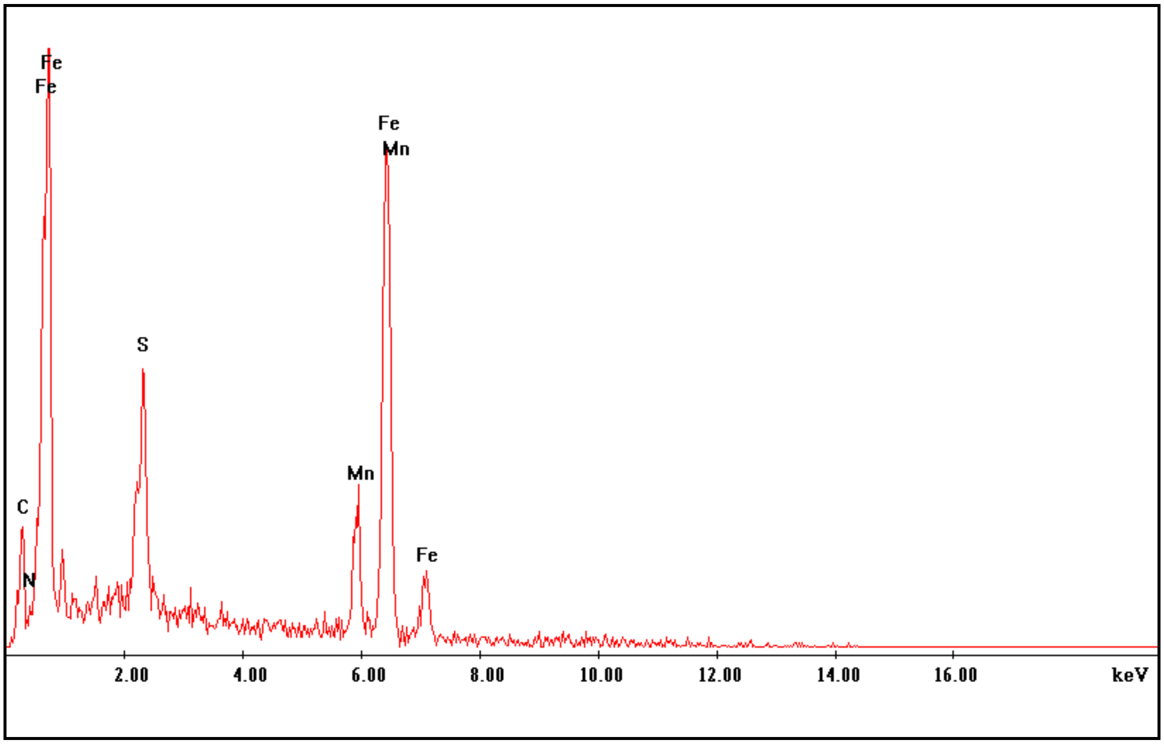

Figure 107. Cementites segregation bands in Nb-bearing steel at 660°C (location 2 & EDS)

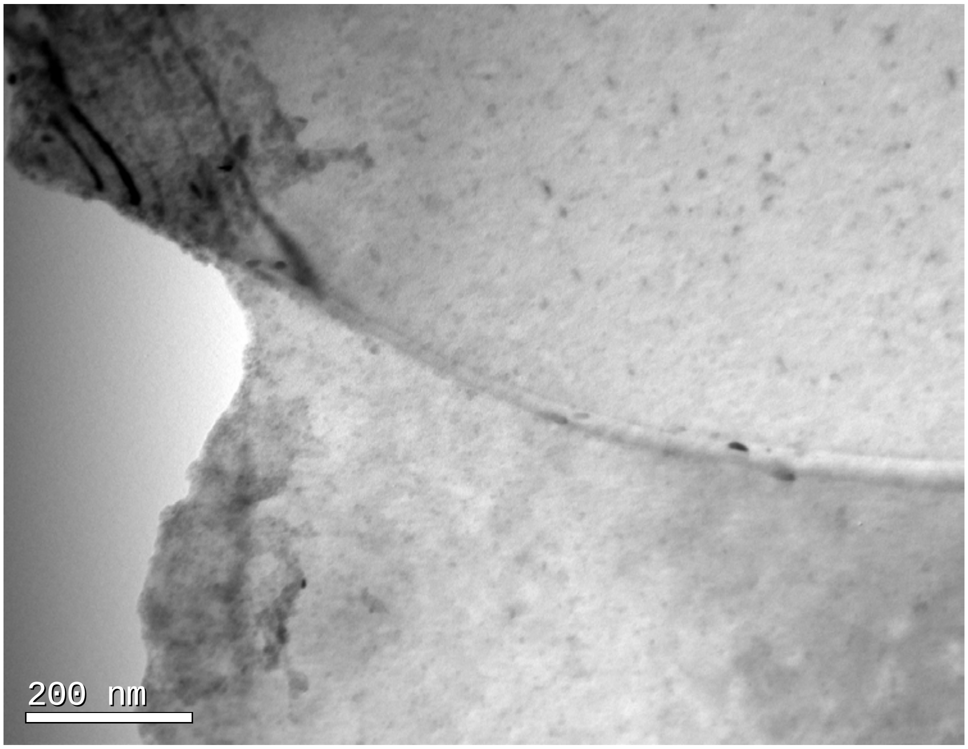

Figure 108. No precipitates formed in Nb-bearing steel at 660°C (location 1 & TEM)

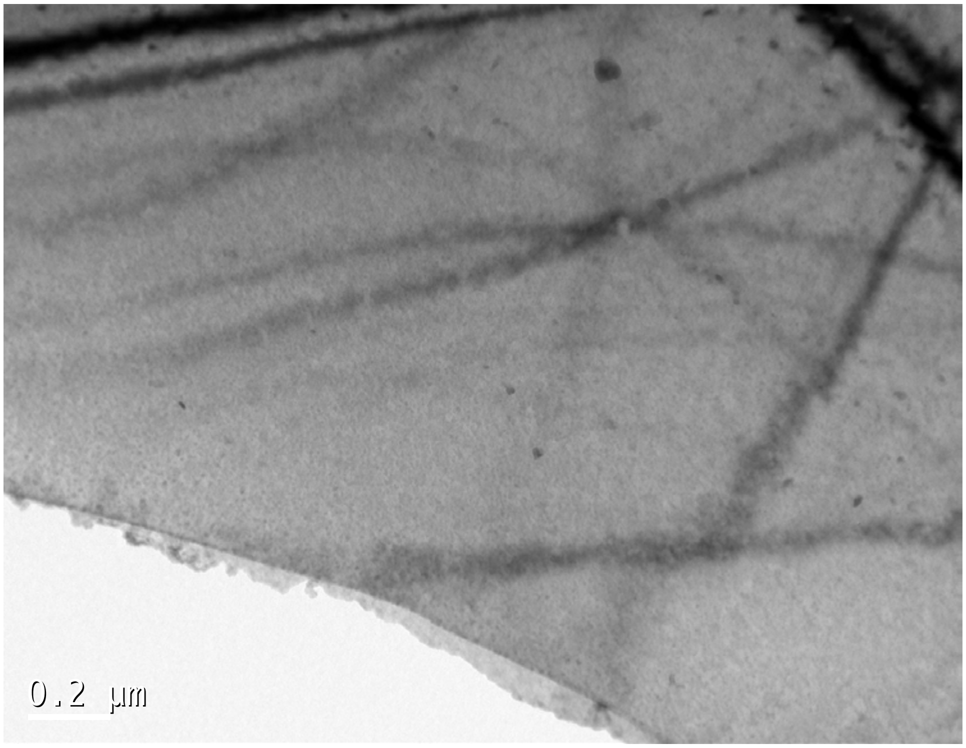

Figure 109. No precipitates formed in Nb-bearing steel at 660°C (location 2 & TEM)

TiC precipitates were formed during annealing process, their formation consumed part of the stored energy and thus reduced the driving force for recrystallization. The new formed fine precipitates also applied certain dragging pinning forces on the grain boundaries to inhibit the moving of them and lowered the recrystallization speed further. This effect became more obvious after 660ºC because larger volume fraction of the TiC precipitates and most stored energy has been consumed. No precipitates were observed in Nb-bearing steel in both hot band and annealed steel samples except some cementite segregation bands due to higher Mn concentration, but these cementites would not apply any dragging effects on the recrystallization process.

Certain special grain boundaries such as Coincidence Site Lattice (CSL) have relatively lower energy and mobility. Their fractions were analyzed at 580°C for Ti-bearing steel and 560°C for Nb-bearing steel. No recrystallized grains formed at these stages for both steels, but recrystallized grains were observed at 600°C for Ti-bearing steel and 580°C for Nb-bearing steel, which meant that the start temperature for Ti-bearing steel is between 580°C and 600°C, and the start temperature for Nb-bearing steel is between 560°C and 580°C. The distribution characteristics of the grain boundaries before the recrystallization stages could explain their influence on the annealing behavior. From Figure 110, we can see that the fraction of CSL boundaries in the Ti-bearing steel at 580°C nearly double of those in the Nb-bearing steel at 560°C. The higher fraction of low mobility CSL boundaries in the Ti-bearing steel could be another reason to cause the slower recrystallization speed of it. The Low Angle Grain Boundaries (LAGB) normally stands for the density of dislocation and stored energy. The lower fraction of LAGB in Ti-bearing steel confirmed the stored energy calculation results using sub-grain method. Therefore the nature of the ferrite grain boundaries prior to cold rolling seems to be relevant.

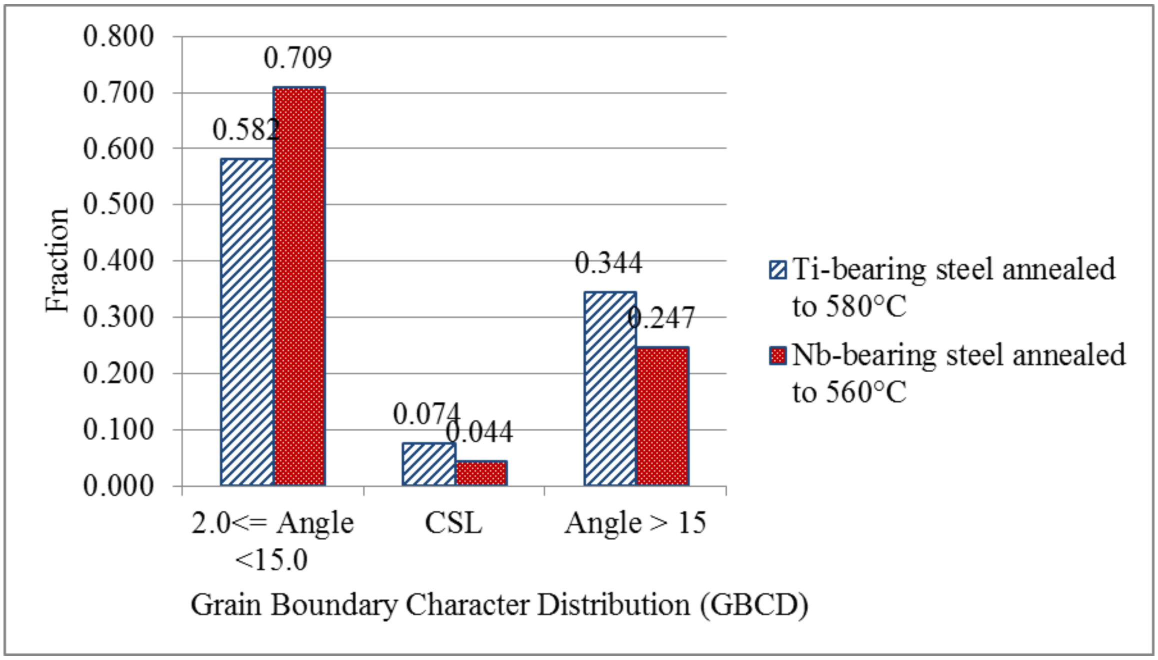

Figure 110. Comparison of Grain Boundary Character Distribution (GBCD) of Ti-bearing steel and Nb-bearing steel before recrystallization start temperature

6.0 DISCUSSION

Niobium is normally recognized as the most effective microalloying addition for retarding recrystallization. But based on our experiments, Nb-bearing cold rolled steel samples start to soften due to recovery or recrystallization at a lower temperature and with higher kinetics than Ti-bearing steel samples, even though the cold rolling rate of Ti-bearing steel samples is a little higher than Nb-bearing steel samples. This might be analyzed and explained from the following aspects: stored energy, precipitation and/or solute drag, precipitates forming stage, special grain boundaries, texture, and multi factors effects. These factors will be discussed one by one in detail.

1) Different composition may cause different hot band microstructure and different amounts of dislocation density, i.e., stored energy, remained in the alloys after hot rolling deformation. Higher dislocation density in the hot band steel will cause even higher dislocation density in the sheet steel after cold rolling deformation, i.e., the higher stored energy in cold rolled Nb-bearing sheet steel was inherited from the higher stored energy in the hot band steel. More stored energy in Nb-bearing sheet steel samples would promote its recovery and recrystallization during annealing process.
2) Precipitation and/or solute drag could retard both recovery and recrystallization dramatically. The key microalloying additions were different and also at different amounts. The amount of key microalloying additions to the steel determined the total

amount of precipitates which could be formed. Based on the calculation, much more TiC precipitates could be formed in the Ti-bearing steel than NbC precipitates could be formed in the Nb-bearing steel. Based on the SEM, EDS, TEM and HRTEM experiments, little of any kinds of precipitates were formed in the Nb-bearing steel during annealing process, except several cementite segregation bands parallel to the rolling direction, which were believed causing by the higher Manganese concentration in Nb-bearing steel. On the other hand, TiC precipitates were easily observed in recrystallized Ti-bearing steel because relatively high volume fraction. Lines of TiC precipitates were found along the unrecrystallized deformed grain boundaries and also in the center of the recrystallized grains along with some random dispersion TiC precipitates on both sides. These lines of TiC precipitates in the center of recrystallized grains were believed to initially precipitate along the deformed grain boundaries because of the higher energy there, and they inhibited the moving of the boundaries during recrystallization, but finally left in the center of recrystallized grain. The sizes of these TiC precipitates observed were from 2nm to 50nm and the average size of them was about 15nm. Most of them had a shape like platelet or disk, the thicknesses and diameter were different at different forming stages and locations. They kept growing with the annealing temperature and time. The ratio of nucleation rate over growth rate of these TiC precipitates seems high when the annealing temperature increased from 640°C to 660°C, because the volume fraction increased much faster than the size of them. The smaller size of these precipitates, the higher pinning force they would apply to the grain boundaries. So they kept applying dragging force during the annealing process, which make a much steadier and slower recrystallization speed of Ti-bearing steel. Nb-bearing steel had a much higher recrystallization speed because of higher stored energy and no dragging effects from precipitates. The recrystallization was nearly done when the annealing temperature reached 660°C and grain growth started from that temperature. That's why the hardness of Nb-bearing steel dropped much steeper from 600°C to 660°C and slowed down after that, while the hardness dropping of Ti-bearing steel kept a steady speed until soaking 6 hours at 670°C. If the concentration of Nb in Nb-bearing steel was higher and similar volume fraction of NbC precipitates were formed as TiC precipitates in Ti-bearing steel, the dragging effect of Nb based precipitates might have been more effective, and that would be a totally different situation.

3) Precipitates could form at different stages: before annealing versus during annealing. No precipitates were found in the Ti-bearing hot band steel, so the TiC precipitates must be formed during the annealing process. The retarding effects became more significant because the formation of these precipitates would definitely consume part of the stored energy which supplied the initial driving force for recovery and recrystallization. And it would take more stored energy to overcome the pinning force.
4) Certain special grain boundaries such as Coincidence Site Lattice (CSL) boundaries have very low boundary energy and their mobility is therefore very low. More CSL boundaries were found in the Ti-bearing steel at lower temperature close to the recrystallization start temperature. Although at a relatively low fraction, it could also be a reason to slow down the recrystallization speed of Ti-bearing steel.
5) It's well known that the stored energy is strongly orientation dependent and γ-fiber area normally contains more stored energy and recrystallizes easier and faster than α-fiber area. This was confirmed to be true for both steels by comparing the EBSD crystal

direction maps with the stored energy distribution maps. If more γ-fiber area might were developed in Nb-bearing steel during cold rolling, it could be another reason to explain its faster recrystallization. But after analyzing and comparing the fraction of γ-fiber and α-fiber, they were at about same level. So texture could not be a critical factor causing the different annealing behavior in this study.

6) It could be a combination effect of two or more factors mentioned above. Some factors could be more efficient than others at certain stage or stages. For example, the stored energy played a more important role in controlling the recovery and recrystallization speed at earlier stages, but after precipitates were formed and part of the stored energy had been consumed, the dragging force and the boundary energy would direct the recrystallization and grain growth speed at later stages.

7.0 CONCLUSIONS

In order to solve practical industrial problems during batch annealing process of HSLA steels, this study has been conducted to fully understand the influence of multi factors on the annealing behavior of these steels. Based on the results analysis, the following conclusions could be made.

1) Higher cold rolling reduction rate would cause higher dislocation density, i.e. stored energy. The stored energy distribution through the thickness of the steel sample is not uniform. The surface of the sample exhibited higher deformation and stored energy than the center of the sample. This lack of uniformity is independent of steel composition and seems to be related to the inhomogeneous nature of the cold deformation.
2) The stored energy was continuously consumed to supply the initial driving force for recovery and recrystallization during batch annealing. The hardness of annealed sample dropped with stored energy because the decrease on the dislocation density. The surface of the sample recrystallized faster than the center of the sample because of higher stored energy caused by higher deformation and more shear strain.
3) The stored energy was consumed faster in the Nb-bearing steel than in the Ti-bearing steel, leading to faster recrystallization kinetics in the Nb-bearing steel. This difference could be caused by the higher stored energy in the cold rolled Nb-bearing steel, which may be inherited by the nature of the type of ferrite which could have a higher dislocation density (stored energy) in the hot band condition.

4) TiC precipitates were formed during the recrystallization process of Ti-bearing steel. The formation of precipitates consumed part of the stored energy which decreased some driving force. The new formed fine TiC precipitates would also apply certain pinning force on the grain boundaries which dragged the moving of those boundaries, i.e., lowered the recrystallization speed further. No carbide or other kinds of precipitates were found in Nb-bearing steel after annealing.

5) In Ti-bearing steel, the stored energy and precipitates apply balanced forces on the grain boundaries, stored energy played a more important role at earlier recovery and recrystallization stages of annealing, and precipitates dragged the annealing process more at the later recrystallization and grain growth stages. If the stored energy was very high, it could surpass the influence of precipitates. For example, the recrystallization speed of the surface layer of the Ti-bearing steel sample is comparable to that of the center layer of Nb-bearing steel sample.

6) Certain special grain boundaries like twin boundaries (Sigma 3) have a very low boundary energy and mobility. Ti-bearing steel contained higher fraction of CSL boundaries before recrystallization started. Although at a relatively small amount, but could also drag the recrystallization speed.

7) Stored energy is strongly texture dependent. It’s confirmed that γ-fiber area contained more stored energy than α-fiber area by comparing the EBSD crystal direction maps with the stored energy distribution maps. But after analyzing and comparing the fraction of γ-fiber and α-fiber, they were at about same level in both steels. So texture could not be a critical factor causing the different annealing behavior in this study

8) When 670°C was used as the highest heating temperature and soaking temperature for both steel samples, recrystallization started around 600°C for Ti-bearing steel and was nearly done after soaking 6 hours at 670°C. But for Nb-bearing steel, recrystallization starts around 580°C and was nearly done when the annealing temperature reached to 660°C

9) Lower heating rate will make recrystallization more difficult because more stored energy is consumed during recovery stage. But recrystallization seems more sensitive to temperature other than heating rate. Higher soaking temperature (always lower than Tac1) will cause a faster recrystallization.

10) The HSLA steel hot band samples with higher Nb & Mn concentration (Nb-bearing) have smaller grain size and smaller ferrite volume fraction. These characteristics determined that higher stored energy in Nb-bearing hot band steel, which could come from both the alloy composition and the process procedures. The second microconstituent in the HSLA steel hot band samples is pearlite, its volume fraction increases with Nb & Mn concentration.

8.0 SUGGESTIONS

Based on the conclusions drawn from this study, the following suggestions were made to the industrial production of HSLA steel during the batch annealing process:

To make the Ti-bearing steel acting more similar to the Nb-bearing steel, the stored energy in Ti-bearing steel will need to be increased. This can be done either by increasing the cold rolling reduction rate or by reducing the hot band coiling temperature.

To reduce the difference of annealing results between the cool spot and hot spot of the coil, higher cold rolling reduction rate would be needed to make the steel at the cool spot of the coil recrystallizing much faster. A higher heating rate and soaking temperature could also be tried to get a better uniformity.

BIBLIOGRAPHY

1. Titchener, A.L.a.B., M. B., Progr. Met. Phys., 1958(7): p. 247-338.

2. Cottrell, A.H., *Theory of dislocations.* Progress in Metal Physics, 1953. **4**(Copyright 2004, IEE): p. 205-264.

3. Gordon, P., Trans. AIME, 1955. **203**: p. 1043.

4. Bohnenkamp, K., Luecke, K., Masing, G., *Messung der latenten Vorformungsenergie an gezogenen Kupferdraehten.* Zeitschrift fuer Metallkunde, 1955. **46**(10): p. 765-770.

5. Clarebrough, L.M., Hargreaves, M. E., West, G. W., Proc. Roy. Soc. London, 1955. **A232**: p. 252.

6. Conrad, H. and B. Christ, Recovery and Recrystallization of Metals, 1963: p. 124.

7. Oyarzabal, M., A. Martinez-de-Gerenu, and I. Guti, *Effect of stored energy and recovery on the overall recrystallization kinetics of a cold rolled low carbon steel.* Materials Science & Engineering: A (Structural Materials: Properties, Microstructure and Processing), 2008. **485**(Copyright 2008, The Institution of Engineering and Technology): p. 200-9.

8. Vanderschueren, D., N. Yoshinaga, and K. Koyama, *Recrystallisation of Ti IF steel investigated with electron back-scattering pattern (EBSP).* ISIJ International, 1996. **36**(8): p. 1046-1054.

9. Cao, S., et al., *EBSD investigation on oriented nucleation in IF steels.* Journal of Materials Science and Technology, 2007. **23**(2): p. 262-266.

10. Etter, A.L., et al., *Stored energy evolution in both phases of a duplex steel as a function of cold rolling reduction.* Scripta Materialia, 2006. **54**(4 SPEC. ISS.): p. 683-688.

11. Avraamov, Y.S., A.G. Gvozdev, and V.M. Kutsak, *Orientation dependence of grain-boundary energy of silicon iron.* Fizika Metallov i Metallovedenie, 1973. **36**(Copyright 1974, IEE): p. 1108-11.

12. Dillamore, I.L., C.J.E. Smith, and T.W. Watson, *Oriented nucleation in formation of annealing textures in iron.* Metal Science Journal, 1967. **1**: p. 49-54.

13. Every, R.L. and M. Hatherly, *ORIENTED NUCLEATION IN LOW-CARBON STEELS.* Texture, 1974. **1**(3): p. 183-194.

14. Rajmohan, N., et al., *Neutron diffraction method for stored energy measurement in interstitial free steel.* Acta Materialia, 1997. **45**(Copyright 1997, IEE): p. 2485-94.

15. Choi, S.-H. and Y.-S. Jin, *Evaluation of stored energy in cold-rolled steels from EBSD data.* Materials Science & Engineering A (Structural Materials: Properties, Microstructure and Processing), 2004. **A371**(Copyright 2004, IEE): p. 149-59.

16. Read, W.T. and W. Shockley, *Dislocation Models of Crystal Grain Boundaries.* Physical Review, 1950. **78**(Copyright (C) 2009 The American Physical Society): p. 275.

17. Choi, S.-H., *Monte Carlo technique for simulation of recrystallization texture in interstitial free steels.* Materials Science Forum, 2002. **408-412**(Copyright 2003, IEE): p. 469-74.

18. Wu, J., *DEVELOPMENT OF A NEW TECHNIQUE TO IDENTIFY AND QUANTIFY COMPLEX AUSTENITE DECOMPOSITION PRODUCTS.* PhD thesis, University of Pittsburgh, 2005.

19. Choi, S.H., F. Barlat, and J.H. Chung, *Modeling of textures and yield surfaces during recrystallization in IF steel sheets.* Scripta Materialia, 2001. **45**(Copyright 2002, IEE): p. 1155-62.

20. Bacroix, B., A. Miroux, and O. Castelnau. *Simulation of the orientation dependence of stored energy during rolling deformation of low carbon steels*. in *Gilles Canova Memorial Symposium. Multi-scale Modelling of Mechanical Properties of Materials, 12-15 June 1998*. 1999. UK: IOP Publishing.

21. Diligent, S., et al., *Lattice orientation dependence of the stored energy during cold-rolling of polycrystalline steels.* Acta Materialia, 2001. **49**(19): p. 4079-4088.

22. Radhakrishnan, B., G. Sarma, and T. Zacharia, *Monte Carlo simulation of deformation substructure evolution during recrystallization.* Scripta Materialia, 1998. **39**(12): p. 1639-1645.

23. Sarma, G.B., B. Radhakrishnan, and T. Zacharia, *Finite element simulations of cold deformation at the mesoscale.* Computational Materials Science, 1998. **12**(2): p. 105-123.

24. Raabe, D., F. Roters, and Z. Zhao, *A texture component crystal plasticity finite element method for physically-based metal forming simulations including texture update.* Materials Science Forum, 2002. **396-402**(Copyright 2003, IEE): p. 31-6.

25. Raabe, D., et al. *A texture component crystal plasticity finite element method for scalable large strain anisotropy simulations*. in *Texture of Materials. ICOTOM 13. 13th*

International Conference on Textures of Materials, 26-30 Aug. 2002. 2002. Switzerland: Trans Tech Publications.

26. Raabe, D. and F. Roters, *Using texture components in crystal plasticity finite element simulations.* International Journal of Plasticity, 2004. **20**(Copyright 2004, IEE): p. 339-61.

27. Choi, S.H., *Simulation of stored energy and orientation gradients in cold-rolled interstitial free steels.* Acta Materialia, 2003. **51**(6): p. 1775-1788.

28. Becker, R. and S. Panchanadeeswaran, *Effects of grain interactions on deformation and local texture in polycrystals.* Acta metallurgica et materialia, 1995. **43**(7): p. 2701-2719.

29. Becker, R., *Analysis of texture evolution in channel die compression - I. Effects of grain interaction.* Acta metallurgica et materialia, 1991. **39**(6): p. 1211-1230.

30. Cuddy, L.J., *Recovery of point defects in iron after low-temperature deformation.* Acta Metallurgica, 1968. **16**(1): p. 23-28.

31. Schmidt, J. and F. Haessner, *Stage III-recovery of cold worked high-purity aluminium determined with a low-temperature calorimeter.* Zeitschrift fur Physik B (Condensed Matter), 1990. **81**(Copyright 1991, IEE): p. 215-22.

32. Clarebrough, L.M., Hargreaves, M.E., Loretto, M.H., L. Himmel, Editor, Recovery and Recrystallization of Metals, Interscience Publishers, New York, 1963: p. 63.

33. Balluffi, R.W., Koehler, J. S., Simmons, R. O., Recovery and Recrystallization, 1963(Interscience Publishers, Inc., New York): p. 1.

34. Cahn, R.W., *Recrystallization of single crystals after plastic bending.* Institute of Metals -- Journal, 1949. **76**(Part 2): p. 121-143.

35. Dunn, C.G., Walter, J.L, *Recrystallization, Grain Growth and Textures.* ASM, Ohio, 1966: p. 461.

36. Burke, J.E. and D. Turnbull, *Recrystallization and grain growth.* Progress in Metal Physics, 1952. **3**(Copyright 2004, IEE): p. 220-292.

37. Cahn, R.W., *A new theory of recrystallization nuclei.* Proceedings of the Physical Society. Section A, 1950. **63**(Copyright 2004, IEE): p. 323-336.

38. Beck, P.A., *The formation of recrystallization nuclei.* Journal of Applied Physics, 1949. **20**(Copyright 2004, IEE): p. 633-634.

39. Hu, H., *Direct observations on annealing of Si-Fe crystal in electron microscope.* Metallurgical Society of American Institute of Mining, Metallurgical and Petroleum Engineers -- Transactions, 1962. **224**(1): p. 75-84.

40. Li, J.C.M., *Possibility of subgrain rotation during recrystallization.* Journal of Applied Physics, 1962. **33**(Copyright 2004, IEE): p. 2958-2965.

41. Beck, P.A. and P.R. Sperry, *Strain induced grain boundary migration in high purity aluminum.* Journal of Applied Physics, 1950. **21**(Copyright 2004, IEE): p. 150-152.

42. Bailey, J.E. and P.B. Hirsch, *The recrystallization process in some polycrystalline metals.* Proceedings of the Royal Society of London, Series A (Mathematical and Physical Sciences), 1962. **267**(Copyright 2004, IEE): p. 11-30.

43. Verbraak, C.A., *Martensitic nucleation of recrystallization textures Martensitische Keimbildung.* Zeitschrift fuer Metallkunde, 1960. **51**(11): p. 646-649.

44. Verbraak, C.A., *Formation of cube recrystallization textures by (112) slip.* Acta Metallurgica, 1958. **6**(9): p. 580-597.

45. Verbraak, C.A., *Application of Rowland mechanism to problem of nucleation of secondary crystals in cube-texture copper.* Acta Metallurgica, 1960. **8**(2): p. 65-70.

46. Chen, S.P., et al., *Quantification of the recrystallization behaviour in Al-alloy AA1050.* Journal of Materials Science, 2002. **37**(Copyright 2002, IEE): p. 989-95.

47. Liu, W.C., et al., *Quantifying the recrystallization of cold rolled AA 3015 aluminum alloy by X-ray diffraction.* Materials Science and Engineering A, 2009. **524**(1-2): p. 168-175.

48. MITSCHE, S., P. POELT, and C. SOMMITSCH, *Recrystallization behaviour of the nickel-based alloy 80 A during hot forming.* Journal of Microscopy, 2007. **227**(3): p. 267-274.

49. Wright, S.I., *Quantification of recrystallized fraction from orientation imaging scans.* Proceedings of the Twelfth International Conference on T extures, 1999. **Volume 1**: p. 104-107.

50. Tarasiuk, J., Gerber, Ph. Bacroix, B., *Estimation of recrystallized volume fraction from EBSD data.* Acta Materialia, 2002. **Volume 50**: p. 1467-1477.

51. Lu, H., P. Sivaprasad, and C.H.J. Davies, *Treatment of misorientation data to determine the fraction of recrystallized grains in a partially recrystallized metal.* Materials Characterization, 2003. **51**(Copyright 2004, IEE): p. 293-300.

52. Field, D.P., *Quantification of partially recrystallized polycrystals using electron backscatter diffraction.* Materials Science & Engineering A (Structural Materials:

Properties, Microstructure and Processing), 1995. **A190**(Copyright 1995, FIZ Karlsruhe): p. 241-6.

53. Beck, P.A., *Annealing of cold worked metals.* Advances in Physics, 1954. **3**(11): p. 245-324.

54. Kronberg, M.L. and F.H. Wilson, *Secondary recrystallization in copper.* American Institute of Mining and Metallurgical Engineers -- Journal of Metals, 1949. **1**(8, Sec 3): p. 501-514.

55. Bowles, J.S.a.B., W., J. Inst. Met., 1948. **74**: p. 501.

56. Sachs, G., *Stresses causing flow Zur Ableitung einer Fliessbedingung.* V.D.I. Zeitschrift, 1928. **72**(22): p. 734-736.

57. Taylor, G.I., *Plastic strain in metals.* Institute of Metals -- Journal, 1938. **62**(1): p. 307-324.

58. Chin, G.Y., W.L. Mammel, and M.T. Dolan, *Taylor's theory of texture for axisymmetric flow in body-centered cubic metals.* Metallurgical Society of American Institute of Mining, Metallurgical and Petroleum Engineers -- Transactions, 1967. **239**(11): p. 1854-1855.

59. English, A.T. and G.Y. Chin, *On variation of wire texture with stacking fault energy in f.C.C. Metals and alloys.* Acta Metallurgica, 1965. **13**(9): p. 1013-1016.

60. Chin, G.Y., W.L. Mammel, and M.T. Dolan, *Computerized plastic deformation by slip.* Transactions of the Metallurgical Society of AIME, 1967. **239**(Copyright 2004, IEE): p. 1111-1112.

61. Ahlborn, H. and G. Wassermann, *Effects of degree and temperature of deformation on texture of silver wire Einfluss von Verformungsgrad und -temperatur auf die Textur von Silberdraehten.* Zeitschrift fuer Metallkunde, 1963. **54**(1): p. 1-6.

62. Hirsch, J. and K. Lücke, *Overview no. 76: Mechanism of deformation and development of rolling textures in polycrystalline f.c.c. metals--II. Simulation and interpretation of experiments on the basis of Taylor-type theories.* Acta Metallurgica, 1988. **36**(11): p. 2883-2904.

63. Honeff, H., Mecking, H., Proceedings ICOTOM 5 Aachen, 1978. **Vol 1**(Berlin: Springer-Verlag): p. 265-275.

64. Molinari, A., G.R. Canova, and S. Ahzi, *A self consistent approach of the large deformation polycrystal viscoplasticity.* Acta Metallurgica, 1987. **35**(Copyright 1988, IEE): p. 2983-94.

65. Kalidindi, S.R. and L. Anand, *An approximate procedure for predicting the evolution of crystallographic texture in bulk deformation processing of FCC metals.* International Journal of Mechanical Sciences, 1992. **34**(Copyright 1992, IEE): p. 309-29.

66. Belyakov, A., et al., *Incomplete recrystallization in cold worked steel containing TiC.* Materials Science & Engineering A, 2007. **471**(Copyright 2007, The Institution of Engineering and Technology): p. 50-6.

67. Ahlborn, H., E. Hornbogen, and U. Koster, *Recrystallisation mechanism and annealing texture in aluminium-copper alloys.* Journal of Materials Science, 1969. **4**(Copyright 1970, IEE): p. 944-9.

68. Hornbogen E. and K. U., Recrystallization of Metallic Materials, F. Haessner, Ed., Dr. Riederer Verlag GmbH, Stuttgart, 1978. **Chapter 8**.

69. Simoneau, R., G. Begin, and A.H. Marquis, *PROGRESS OF NbCN PRECIPITATION IN HSLA STEELS AS DETERMINED BY ELECTRICAL RESISTIVITY MEASUREMENTS.* 1978. **12**(8): p. 381-386.

70. Gladman, T., D. Dulieu, and I.D. Mcivor, *Microalloying' 75.* Proc. Conf. New York, Union Carbide, 1977(ed. J. Crane): p. 35-58.

71. Listhuber, E., *Symposium on low alloy high strength steels.* Proc. Dusseldorf, Metallurg Companies, 1970: p. 29-34.

72. Wadsworth, J., S.R. Keown, and J.H. Woodhead, *EFFECT OF NIOBIUM CARBIDE PRECIPITATION ON THE DENSITY CHANGES AND CREEP PROPERTIES OF TYPE 347 AUSTENITIC STAINLESS STEELS.* Metal Science, 1976. **10**(3): p. 105-112.

73. Palmiere, E.J., C.I. Garcia, and A.J. DeArdo, *Compositional and microstructural changes which attend reheating and grain coarsening in steels containing niobium.* Metallurgical and Materials Transactions A (Physical Metallurgy and Materials Science), 1994. **25A**(Copyright 1994, IEE): p. 277-86.

74. Koyama, S., T. Ishii, and K. Narita, J. Jpn Inst. Mater., 1979. **35**(11): p. 1089-1094.

75. Baker, R.G. and N. J., *Precipitation processes in steels.* The Iron and Steel Institute Journal Special Report, 1959. **No. 64**: p. Page 1.

76. Kurdjumov, G. and S. G., Z. Phyzik, 1930. **64**: p. 325.

77. Humphreys, F.J. and J.W. Martin, *The effect of dispersed phases upon the annealing behaviour of plastically deformed copper crystals.* Philosophical Magazine, 1968. **17**(Copyright 2004, IEE): p. 365-380.

78. Jones, A.R. and N. Hansen, *The interaction between particles and low angle boundaries during recovery of aluminium-alumina alloys.* Acta Metallurgica, 1981. **29**(Copyright 1981, IEE): p. 589-99.

79. Kwon, O. and A.J. DeArdo, *Interactions between recrystallization and precipitation in hot-deformed microalloyed steels.* Acta metallurgica et materialia, 1991. **39**(Copyright 1991, IEE): p. 529-38.

80. Smith, C.S., TMS-AIMF, 1948. **15**: p. 175.

81. Hutchinson, W.B. and B.J. Duggan, *INFLUENCE OF PRECIPITATION ON RECRYSTALLIZATION AND TEXTURE DEVELOPMENT IN AN IRON-1. 2% COPPER ALLOY.* 1978. **12**(8): p. 372-380.

82. Hellman, P. and M. Hillert, Scand. J. Metall., 1975. **4**: p. 211-219.

83. Hillert, M., *Physical metallurgy of thermomechanical processing of steels and other metals.* Proc. Int. Conf. Tokyo, Japan, The Iron and Steel Institute of Japan, 1988: p. 30-38.

84. Hu, H., ASM metals handbook, 1985. **9**: p. 696.

85. Wei, F.-G., T. Hara, and K. Tsuzaki, *High-resolution transmission electron microscopy study of crystallography and morphology of TiC precipitates in tempered steel.* Philosophical Magazine, 2004. **84**(17): p. 1735-1751.

86. Zhou, J., Y. Kang, and X. Mao, *Precipitation characteristic of high strength steels microalloyed with titanium produced by compact strip production.* Journal of University of Science and Technology Beijing: Mineral Metallurgy Materials (Eng Ed), 2008. **15**(4): p. 389-395.

87. Jouet, A., Rev. Metall./Cah. Inf. Tech., 1997. **11**: p. 1425–1434.

88. Kneissl, A.C., C.I. Garcia, and A.J. DeArdo, *HSLA Steels: Processing, Properties and Applications.* The Minerals, Metals and Materials Society, 1992.

89. Charleux, M., Poole, W., Militzer, M., et al., Metall. Mater. Trans., 2001. **A 32**: p. 1635.

90. Fujita, N., et al., *Effect of Nb on high-temperature properties for ferritic stainless steel.* Scripta Materialia, 1996. **35**(6): p. 705-710.

91. Le Bon, A., J. Rofes-Vernis, and C. Rossard, *Recrystallization and precipitation during hot working of a nb-bearing hsla steel.* Metal Science, 1975. **9**(Copyright 1975, IEE): p. 36-40.

92. Webster, D. and J.H. Woodhead, *Effect of 0.03% niobium on ferrite grain size of mild steel.* Iron and Steel Institute -- Journal, 1964. **202**(Part 12): p. 987-994.

93. Ruiz-Aparicio, L.J., Garcia, C.I., and DeArdo, A.J., *Development of {111} Texture in Intersticial Free Steels.* Metall. Trans. A, 2001. **32A (2)**: p. 417-423.

94. Dillon, C.P., Corrosion Resistance of Stainless Steels, 1995: p. Marcel Dekker, Inc., New York.

95. Xu, Y., et al. *Annealing behavior and formability*. in *Proceedings of the International Symposium on Low-Carbon Steels for the 90's, October 18, 1993 - October 21, 1993.* 1993. Pittsburg, PA, USA: Publ by Minerals, Metals & Materials Soc (TMS).

96. Palmiere, E.J., *Suppresion of Recrystallization during the Hot Deformation of Microalloyed Austenite.* PhD thesis, University of Pittsburgh, 1991.

97. Deardo, A.J., *Niobium in modern steels.* International Materials Reviews, 2003. **Volume 48**(Number 6): p. 371-402.

98. Hutchinson, C.R., et al., *The comparative effectiveness of Nb solute and NbC precipitates at impeding grain-boundary motion in Nb steels.* Scripta Materialia, 2008. **59**(Copyright 2008, The Institution of Engineering and Technology): p. 635-7.